Long noncoding RNA *H19* protects from dietary obesity by promoting brown adipose tissue commitment and function

I N A U G U R A L – D I S S E R T A T I O N

zur

Erlangung des Doktorgrades

der Mathematisch-Naturwissenschaftlichen Fakultät

der Universität zu Köln

vorgelegt von

ELENA SCHMIDT

aus Ludwigsburg

KÖLN

2018

Berichterstatter:	Prof. Dr. Jan-Wilhelm Kornfeld
	Prof. Dr. Thorsten Hoppe
Tag der mündlichen Prüfung:	29.10.2018

Table of Contents

Figure Index

Table Index

Abbreviations

1°	Primary
AC	Adenylyl cyclase
AMP	Adenosine-mono-phosphate
ANOVA	Analysis of variance
ASO	Antisense oligonucleotide
AT	Adipose Tissue
Atf2	Activating transcription factor 2
ATP	Adenosine-tri-phosphate
BAT	Brown adipose tissue
BMI	Body mass index
brite	Brown-in-white
BtnTg	Biotin-TEG
BW	Body weight
BWS	Beckwith-Wiedemann Syndrome
cAMP	Cyclic AMP
CD	Control diet
cDNA	Complementary DNA
C/EBPβ	CCAAT/enhancer-binding protein-β
cGMP	Cyclic GMP
ChART	Capture hybridization analysis of RNA targets
Cidea	Cell death-inducing DFFA-like effector A
CNS	Central nervous system
CPAT	Coding Potential Assessment Tool
CPC	Coding Potential Calculator
Cre	Cyclation recombination
Creb	CAMP response element-binding protein
CT	Threshold cycle
CTCF	CCCTC-binding factor
DEPC	Diethyl pyrocarbonate
DIO	Diet-induced obesity
Dio3	Deiodinase, iodothyronine type III
Dlk1	Delta-like non-canonical notch ligand 1
DM	Diabetes mellitus
DMD	Differentially-methylated domain
DNA	Deoxyribonucleic acid
dNTP	Deoxynucleotide triphosphate
E	Embryonic day
EBF2	Early B-cell factor 2
ECAR	Extracellular acidification rate
EE	Energy expenditure
EHMT1	Euchromatic histone-lysine N-methyltransferase 1

EM	Electron microscopy
eWAT	Epididymal white adipose tissue
EZH2	Enhancer of zeste homolog 2
FCCP	Carbonyl cyanide-4-(trifluoromethoxy)phenylhydrazone
FFA	Free fatty acids
Firre	Functional intergenic repeating RNA element
Fl	Floxed
FPKM	Fragments per kilobase of transcript per million mapped reads
GC	Guanylyl cyclase
GO	Gene ontology
GTT	Glucose tolerance test
H19	H19, imprinted maternally expressed transcript
H&E	Hematoxylin and eosin
HDAC	Histone deacetylase
HFD	High-fat diet
HNF4a	Hepatocyte nuclear factor 4a
hnRNP	Heterogeneous nuclear ribonucleoprotein
HOTS	H19 opposite tumor suppressor
Hprt1	Hypoxanthine phosphoribosyltransferase 1
ICR	Imprinting control region
ID	Imprinting disorder
Igf	Insulin-like growth factor
Igf2	Insulin-like growth factor 2
Igf1r	Insulin-like growth factor 1 receptor
IGN	Imprinted gene network
IPA	Ingenuity pathway analysis
ITT	Insulin tolerance test
JARID2	Jumonji, AT rich interactive domain 2
LNA	Locked nucleic acids
lncRNA	Long noncoding RNA
lincRNA	Long intergenic noncoding RNA
Mapk	Mitogen-activated protein kinase
MBD1	Methyl-CpG-binding domain protein 1
MeCP2	Methyl-CpG binding protein 2
MEG	Maternally expressed gene
Meg3	Maternally-expressed 3
miRNA	MicroRNA
MPW	Millipore H_20
mRNA	Messenger RNA
Myf5	Myogenic factor 5
NCD	Normal chow diet
Ndn	Necdin

Ndufaf7	NADH:Ubiquinone Oxidoreductase Complex Assembly Factor 7
NE	Norepinephrine
NEFA	Non-esterified fatty acids
NP	Natriuretic peptide
Npra	Natriuretic peptide receptor A
NST	Non-shivering thermogenesis
nt	Nucleotide
OCR	Oxygen consumption rate
O/N	Over night
Opa1	Optic Atrophy 1
ORF	Open reading frame
PBS	Phosphate buffered saline
PCAF	P300/CBD-associated factor
PCR	Polymerase chain reaction
Pdgfra	Platelet Derived Growth Factor Receptor Alpha
PEG	Paternally expressed gene
Peg1	Paternally-expressed gene 1
Peg3	Paternally-expressed gene 3
PET	Positron-emission tomography
Pgc1α	Peroxisome proliferator-activated receptor gamma coactivator 1α
PI3K	Phosphatidyl inositol 3-kinase pathway
PIBA	Primary immortalized brown adipocytes
piRNA	Piwi-interacting RNA
Pla2	Phospholipase A2
Pparα	Peroxisome proliferator-activated receptor α
Pparγ	Proliferator-activated receptor γ
PRC2	Polycomb Repressive Complex 2
PRDM16	PR domain zinc finger protein 16
PREF1	Preadipocyte factor-1
P/S	Penicillin/streptomycin
qRT-PCR	Real-time quantitative RT-PCR
RNP	Ribonucleoprotein
RNA	Ribonucleic acid
RNAi	RNA interference
RNA-Seq	RNA-Sequencing
rRNA	Ribosomal RNA
RT	Reverse transcription
RTemp	Room temperature
Runx2	Runt-related transcription factor 2
RXRs	Retinoid X receptors
SAH	S-adenosylhomocysteine
SAHH	S-adenosylhomocysteine hydrolase
SCAT or scWAT	Subcutaneous adipose tissue
scr	Scramble (control)
SEM	Standard error of the mean

siRNA	Small interfering RNA
SM	Skeletal muscle
SNS	Sympathetic nervous system
snoRNA	small nucleolar RNA
SRS	Silver Russel Syndrome
SUZ12	Suppressor of zeste 12 homolog
SVF	Stromal vascular fraction
T1DM	Type 1 diabetes mellitus
T2DM	Type 2 diabetes mellitus
TG	Transgene
TGs	Triglycerides
TRx	Thyroid receptors
Ucp1	Uncoupling protein 1
VAT or vWAT	Visceral adipose tissue
WAT	White adipose tissue
WB	Western blot
WHO	World Health Organization
w/o	Without
WT or wt	Wild-type
ZFP516	Zinc finger protein 516

Abbreviations of units

bp	Basepair
µm	Micrometre
g	Gram
mg	Milligram
µg	Microgram
kDa	Kilodalton
l	Liter
ml	Millilitre
µl	Microlitre
M	Molar
mM	Millimole
µM	Micromole
nM	Nanomole
mol	Mole
rpm	Revolutions per minute
TG	Transgene
V	Volts
W	Watt
°C	Degree Celsius
%	Percentage
h, min, s	hours, minutes, seconds
x g	G-force

1 Introduction

1.1 The obesity pandemic

Over the last decades, obesity has become a major public health concern with 1.9 billion adults classified as overweight and 650 million as obese in 2016[1]. The World Health Organisation (WHO) defines overweight and obesity as abnormal or excessive fat accumulation that may impair an individual´s health[1].

Although now recommended only as an approximate measure, the body mass index (BMI) is utilised to classify overweight and obesity. BMI is a simple index of weight-for-height defined as a person´s weight in kilograms divided by the square of his or her height in meters (kg/m^2)[1]. A BMI greater or equal to 25 is referred to as overweight, whereas a BMI greater or equal to 30 is defined as obesity. The number of obesity incidences are steadily increasing with studies showing that, if trends continue as expected, 2.16 billion of the world´s adult population will be classified as overweight and 1.12 billion as obese by 2030[2]. This prognosis is supported by an alarming number of children and adolescents that are strongly affected by obesity and overweight with an estimated 41 million under the age of 5 years and 340 million aged 5-19 years in 2016[1].

Obesity results from a steady and complex synergism between predisposing genes and environmental stimuli[3]. Interestingly, the predisposition to obesity might already develop in offspring in early stages of life as rodent studies indicate that offspring had a higher risk for the development of obesity and impaired glucose homeostasis when the mother consumed a high-fat diet (HFD) during lactation[4]. This result demonstrates the severe impact nutrition might have on an individual´s physiology and draws attention to the alarming reach of the metabolic syndrome. If untreated, obesity can result in severe diseases such as type 2 diabetes mellitus (T2DM)[5], artherosclerosis[6], cardiovascular disease[5], different types of cancer[7], liver manifestations of metabolic disease[8], or even mortality[9].

The obesity pandemic has reached such a severe impact worldwide that we have transitioned to a world in which suffering due to over-nutrition outpaces that due to under-nutrition[10,11] leading to a massive burden on health systems around the globe. Attempts to manage and prevent obesity have had limited success so far. Thus, a better

understanding of the adipocyte itself and the etiology of obesity is necessary to develop more successful and personalized prevention and treatment possibilities.

1.1.1 Obesity, type 2 diabetes mellitus, and other obesity-associated diseases

Diabetes mellitus (DM) is characterized by high blood sugar levels over a prolonged period and, therefore, is classified as metabolic disorder. In 2016, DM was listed as number 7 of the top 10 causes of deaths worldwide[12]. One year later, the International Diabetes Federation (IDF) estimated the total number of adults (20-79 years of age) with DM to be 425 million worldwide[13]. DM is classified into two different forms: Type 1 diabetes mellitus (T1DM) and type 2 diabetes mellitus (T2DM).

T1DM is defined as an autoimmune disease in which insulin-producing β-cells of the pancreas are defective, resulting in a complete loss or highly impaired insulin production[14]. Symptoms include chronic hyperglycemia, polyuria, polydipsia, weight loss, constant hunger, and fatigue[14].

Patients diagnosed with T2DM use the insulin their (initially functional) pancreatic β-cells secrete ineffectively. The disorder is characterized by chronic hyperglycemia caused by the development of insulin resistance in peripheral organs, such as the white adipose tissue (WAT), the liver or the skeletal muscle[15]. Insulin resistance develops due to a progressive loss of the insulin-induced inhibitory effect on glycogenolysis and gluconeogenesis. Furthermore, under these conditions, insulin fails to efficiently stimulate glucose and triglyceride uptake into fat and muscle as well as to suppress hepatic glucose production resulting in increased blood glucose levels.

In a healthy state, insulin binds to the insulin receptor and induces a signalling pathway including the phosphatidyl inositol 3-kinase (PI3K) pathway[16]. Subsequently, AKT is phosphorylated and activated leading to the expression of many targets involved in metabo-regulatory pathways[16]. In the beginning, the hyperactivation of pancreatic β-cells is able to compensate for the insulin resistance. However, chronic hyperglycemia eventually leads to progressive deterioration of pancreatic β-cell function culminating first in exhaustion and loss of these cells ultimately resulting in relative insulin deficiency in T2DM patients[17].

The symptoms of T2DM are similar to that of T1DM but are less distinct. Misinterpretation of symptoms can result in a delayed diagnosis, sometimes even years after onset, a situation where complications are inevitable. Hyperglycemia resulting

from uncompensated T2DM increases the risk for microvascular damage and can result in complications like retinopathy, nephropathy and neuropathy[18]. As such, T2DM can have massive effects on the function of several organs[18]. Moreover, T2DM can result in macrovascular complications which, if left untreated, can result in strokes, heart attacks, and insufficiency in blood flow to legs, potentially leading to amputation[18].

Despite the growing knowledge about molecular and cellular alterations associated with the disease, the steadily increase of T2DM diagnoses strengthen the need to understand the underlying aspects contributing to the development and progression of T2DM and other obesity-associated diseases.

1.2 Regulation of energy metabolism by adipose tissue thermogenesis in mice

Prior research has thoroughly investigated how the central nervous system (CNS), in particular the hypothalamic area of the brain, regulates body weight[19]. Different nuclei of the hypothalamus have been identified and characterized regarding their function in the regulation of energy homeostasis[19]. Moreover, previous studies have shown that a fine-tuned system involving hormonal and neuronal mechanisms is in place to respond to feeding behaviour with neuropeptides produced by the brain[20]. Nevertheless, to ensure proper energy homeostasis in the body the bidirectional communication between peripheral tissues and the brain is important[20].

One peripheral organ that is strongly involved in the regulation of energy and glucose homeostasis in the body is the adipose tissue (AT). Next to its more mechanistic function of cushioning and insulating the body, the AT stores energy in the form of lipids (lipogenesis) after feeding and ensures lipid mobilisation and distribution (lipolysis) within the body after fasting. During lipogenesis excess carbohydrates are converted to fatty acids, which are subsequently esterified and stored as triglycerides (TGs)[21]. Lipolysis, on the other hand, involves the release of fatty acids into the circulation to provide fuel for β-oxidation. Moreover, the AT functions as a paracrine and an endocrine organ. As an endocrine organ, it is responsible for the release of different hormones, in particular adipokines[22] that affect various conditions such as appetite, energy balance, insulin sensitivity, lipid metabolism and lipid homeostasis by interacting with other tissues, the sympathetic nervous system and the brain[23].

In mammals, three different classes of adipocytes have been identified: WAT, mainly located in the intra-abdominal and subcutaneous regions, brown adipose tissue (BAT), primarily found in the interscapular region in rodents, and beige/'brite' (brown in white) AT, an adrenergically inducible form of fat that is dispersed throughout the AT[24]. All three ATs stem from a mesodermal origin and pre-adipocytes express the *preadipocyte factor-1* (*Pref1*), which represses the differentiation of adipocytes[25]. However, as soon as cells undergo growth arrest, *Pref1* expression is down-regulated, activating a signalling cascade that results in adipogenic differentiation. Factors which contribute to this process are the transcription factors proliferator-activated receptor γ (PPARγ) and CCAAT/enhancer-binding proteins (C/EBP α, β and γ)[26].

While white adipocytes are involved in the storage and release of energy in form of fatty acids in response to systemic demands, brown and beige adipocytes convert dietary and stored nutrients such as fatty acids and glucose directly for the generation of heat in a process called non-shivering thermogenesis (NST). With this, euthermia is maintained by uncoupling electrochemical energy stored within proton gradients in mitochondria[24]. These processes propelled brown and beige ATs into the focus of attention as a potential new way to counteract obesity and obesity-associated diseases by increasing whole-body energy expenditure (EE) and, therefore, positively influencing adiposity.

In 1983 it was calculated by Rothwell and Stock that 40-50g of additional maximally stimulated BAT would be sufficient to combust 20% of calories more ingested per day in humans[28]. Critically to this project, dysfunction in the regulation and thermogenic activation of AT results in the development of obesity and its associated disorders such as insulin resistance, diabetes, depression, cardiovascular disease and cancer[29]. Thus, there is an urgent need to better understand the molecular mechanisms in brown and beige adipocytes as the manipulation of adipocyte biology represents an attractive therapeutic strategy to combat metabolic disease.

1.2.1 White adipose tissue

Adipose tissue is a loose connective tissue which is composed of mature adipocytes as well as the stromal vascular fraction (SVF) composed of a heterogeneous cellular ensemble, consisting of preadipocytes, fibroblasts, vascular endothelial cells, various inflammatory cells (macrophages), and immune cells. It develops in distinct locations

throughout the body and larger accumulations are defined as adipose depots. WAT can be divided into several depots of which the most common depots represent visceral fat (located around internal organs) and subcutaneous fat (located beneath the skin). Additionally, WAT can be found in other parts of the body such as bone marrow, intermuscular or in breast tissue.

Visceral white adipose tissue (vWAT), also called abdominal fat, is composed of several adipose depots, including mesenteric, epididymal white adipose tissue (eWAT) and perirenal depots. It is mainly located inside the abdominal cavity surrounding organs such as the stomach, liver, intestines, or kidneys and drains directly through the portal circulation to the liver[23]. Here vWAT provides direct hepatic access to free fatty acids (FFAs) and adipokines which are secreted by visceral adipocytes[23]. vWAT is mostly composed of large adipocytes due to its reduced capacity for preadipocytes to differentiate[23]. Women and men possess different amounts of vWAT. Whereas in females vWAT accounts for 5-8% of body mass, for males its 10-20%[30]. However, in both genders, the amount of visceral fat increases with age[30]. One study showed that patients with a higher amount of visceral abdominal obesity had difficulties in disposing and oxidizing glucose and, therefore, greater lipid oxidation compared to people with peripheral obesity[23].

In humans scWAT is mainly located in the femerogluteal regions, the back, and anterior abdominal wall and accounts for 80% of all body fat[30,31]. Normally, lipid release and uptake in white adipocytes are well balanced. However, due to the constant change in food availability, white adipocytes are more dynamic and possess the possibility to change in size[32]. Typically, white adipocytes contain a unilocular lipid droplet which requires 90% of the adipocyte mass and give the cells their spherical shape[24]. In case of excess energy intake and limited EE cells either increase in number (hyperplasia) or in size (hypertrophy) to provide a storage side for fatty acids[32]. The deposition of lipids within these adipose depots happens in a hierarchical manner. First, fat accumulation in subcutaneous depots represents the normal physiological buffer as it can store FFAs and glycerol as TGs[33]. Second, as soon as lipid storage capacity is saturated, excess energy will be stored in vWAT[32]. When the capacity to store excess TGs in WAT is exceeded or the possibility to generate new adipocytes is impaired, due to genetic predisposition or stress, fat starts to accumulate in areas outside the adipose tissues[23].

Comparing both types of ATs with each other in terms of their role during adiposity, scWAT has been shown to inversely correlate with disease risk whereas

vWAT is often associated with metabolic disease[34]. In a study by Tran and Kahn (2010), transplantation experiments showed that placing vWAT into a subcutaneous position had only little positive effect whereas the transplantation of scWAT into visceral compartments resulted in reduced adiposity and improvements in glucose homeostasis[35]. One contributing factor to the beneficial effects on metabolism is the property of scWAT cells to undergo browning, a process that is activated in response to different stimuli that lead to the expression of the thermogenic gene program, normally associated with BAT (see **1.2.2**). As a consequence, the arising beige cells contribute to EE by reducing the amount of lipids stored within the WAT[36].

As described in this section, WAT depots are distinct from each other as they possess specific differences that comprise among others cellular, molecular, and physiological characteristics[23].

1.2.2 Brown and beige adipose tissue

1.2.2.1 Development of brown and beige adipocytes

The first adipose depot that forms in mice during embryogenesis is BAT[37]. BAT provides newborns with the crucial capacity for NST, thereby enabling them to acclimatize to cold temperatures. Clusters of brown adipocytes can be located in the interscapular region of developing mice as early as embryonic day 14.5 (E14.5)[38]. By executing fate-mapping studies in mice, it has been demonstrated that most brown adipocytes in dorsal BAT depots emanate from a mesodermal progenitor population in the somites[38–40]. In humans, BAT is primarily localized in the neck, the supraclavicular, and mediastinal regions[41].

Brown fat has a different developmental pattern and transcriptional program compared to white fat. Brown adipocytes are marked by *myogenic factor 5* (*Myf5*)[39] which encodes a transcription factor that marks myogenic precursor cells and is involved in important processes in skeletal myogenesis. The close relation of BAT and skeletal muscle is confirmed by other shared characteristics. For example, as shown by various gene expression studies, brown adipocyte precursor cells express several skeletal-muscle-specific genes[42]. Moreover, it has been demonstrated that the mitochondrial proteome of brown adipocytes is more akin to that of muscle cells than to white adipocytes[43]. A cell-fate decision between muscle cells and brown fat cells is

regulated by factors such as PR domain zinc finger protein 16 (PRDM16), euchromatic histone-lysine N-methyltransferase 1 (EHMT1), and *miR-133*[39,44–46].

As soon as precursor cells are committed to developing into BAT cells, adipogenic-specific transcription factors and signaling pathways are necessary for the cells´ development into mature brown adipocytes. Early B-cell factor 2 (EBF2) is a marker for committed brown preadipocytes[38]. EBF2 potentially regulates the lineage specification and is involved in the development of BAT. A different factor that assists in the differentiation of brown adipocytes is PR domain zinc finger protein 16 (PRDM16) which interacts with the adipogenic transcription factors CCAAT/enhancer-binding protein-β (C/EBPβ), peroxisome proliferator activated receptor-γ (PPARγ), zinc finger protein 516 (ZFP516), and euchromatic histone-lysine N-methyltransferase 1 (EHMT1)[24].

The recently identified beige fat[47,48] is defined as clusters of *uncoupling protein 1* (*Ucp1)*-expressing adipocytes that are located outside of common brown fat depots. These beige adipocytes have an abundance of mitochondria and develop in depots of WAT upon cold exposure or when exposed to other particular stimuli. Just like brown adipocytes, beige adipocytes are able to convert energy into heat[49]. The embryonic origin of beige adipocytes is less clear. It has been demonstrated that beige cells in the subcutaneous depot do not stem from Myf5 positive cells[39,50]. Therefore, it can be concluded that beige and brown adipocytes stem from different cell lineages. The question emerged whether beige adipocytes originate from white adipocytes through trans-differentiation or through *de novo* differentiation and maturation of precursors. Some publications report indications that large unilocular white adipocytes transform into beige adipocytes upon stimulation[51]. Conversely, a study by Wang et al. (2013), in which authors pulse labeled mature adipocytes in WAT using LacZ, showed convincingly that most beige adipocytes derive from a precursor population rather than from pre-existing adipocytes[52].

1.2.2.2 Characteristics of brown and beige adipocytes

In terms of morphological and biochemical characteristics, brown and beige adipocytes show compelling similarities[53]. As both contain many small lipid droplets, they are termed multilocular in contrast to unilocular white adipocytes. Moreover, both adipocytes are densely packed with mitochondria and express marker thermogenic

genes such as *Ucp1*, *cell death-inducing DFFA-like effector A* (*Cidea*), *peroxisome proliferator-activated receptor gamma coactivator 1α* (*Pgc1α*), and *peroxisome proliferator-activated receptor α* (*Pparα*). Furthermore, in response to specific stimuli, both adipocytes display thermogenesis[49].

Despite these striking similarities, brown and beige adipocytes also exhibit unique phenotypic and functional features: Whereas brown adipocytes contain an abundance of mitochondria and express high levels of *Ucp1* and other thermogenic components under basal conditions, beige adipocytes express those only upon β-adrenergic stimulation[48]. This difference between brown and beige fat cells can be observed *in vivo* and *ex vivo*[48,54]. More specifically, the stable thermogenic character of brown fat cells is at least partly cell autonomous as adipogenic precursors, isolated from BAT, induce the expression of *Ucp1* during the process of differentiation in cell culture[54]. In contrast, specific beige precursors or adipogenic precursors from WAT lack the capacity to activate the thermogenic program in culture unless they are stimulated with inducers like thiazolidinediones[47,55] or β-adrenergic agonists[48]. Beige adipocytes are, therefore, more flexible and can both function as either energy storing or energy dissipating cell types depending on environmental or physiological circumstances.

Moreover, mouse and human beige adipocytes have the capacity to activate the thermogenic mechanism which, consequently, affects systemic energy homeostasis independently of UCP1 function, by running a futile creatine cycle that produces heat as a reaction to stimuli such as cold or β-adrenergic activation. By blocking this cycle, a reduction of the thermogenic capacity of inguinal WAT (and other WAT depots) can be observed which leads to a decline in the animal´s oxygen consumption[56]. The phenomenon of this UCP1-independent pathway for thermogenesis in beige adipocytes may be utilized to explain, at least partially, why UCP1-deficient animals are able to survive in the cold through gradual acclimatization[24].

1.2.2.3 Induction of thermogenesis in brown and beige fat

Upon cold exposure, NST in mammal BAT is activated aimed at maintaining constant body temperatures through the production of heat independently from shivering[57]. In order to fuel NST heat production, BAT combusts nutrients and oxygen delivered through blood circulation. UCP1, and its activity in the mitochondrial membrane of BAT cells, plays and important role in this process. As an electron transporter, UCP1

uncouples the electron transport from ATP synthesis thereby inducing heat production and subsequently EE[22].

Cold, as an important regulator of different aspects of BAT, is sensed by diverse mechanisms such as thermoreceptors in the skin. These thermoreceptors elicit sympathetic outflow to BAT through a complex neural circuitry (Figure 1)[49]. In detail, the cascade is activated by sympathetic neurons releasing catecholamines such as norepinephrine (NE) that bind to β-adrenoreceptors which are located on the surface of brown adipocytes and activating adenylyl cyclase (AC), consequently increasing cyclic AMP (cAMP; light green circles) concentrations and PKA activity. Among different β-adrenoreceptors, the β3-adrenoreceptors can be identified as the most efficient subtype of BAT thermogenesis[22]. Next to catecholamines, natriuretic peptides (NPs) bind to natriuretic peptide receptor A (Npra) and activate guanylyl cyclase (GC) to increase the concentrations of cyclic GMP (cGMP) and activate PKG. Upon activation of PKA and PKG, similar mechanisms lead to transcriptional responses in brown adipocytes through the activity of phosphorylated cAMP response element-binding protein (Creb) and p38 mitogen-activated protein kinases (Mapk). The transcription of downstream thermogenic genes such as *Ucp1* results from phosphorylated Mapk causing the phosphorylation and activation of activating transcription factor 2 (ATF2) and PGC1α.

As a transcriptional cofactor, PGC1α regulates specialized functions of brown adipocytes and is considered as a dominant regulator of mitochondrial biogenesis, oxidative metabolism, and thermogenesis in brown fat[58]. It also interacts with PPARγ, PPARα, retinoid X receptors (RXRs), and thyroid receptors (TRx) and has been shown to be crucial for thermogenesis rather than adipogenesis[59]. It has as well been shown that catecholamines lead to an increase of *miR-196a* causing an increase in *C/ebpβ* expression[49]. This process supports the drive of the thermogenic gene program.

The activation of PKA and PKG not only triggers the thermogenic gene program, it induces lipolysis as well. Upon lipolysis induction, lipid droplets release FFAs that are subsequently oxidized for heat production by the mitochondria. The release of long-chain fatty acids from the mitochondrial membrane by phospholipase A2 (PLA2) results in the proton leak through UCP1. Other stimuli that are able to induce thermogenesis in BAT comprise β-adrenergic pharmaceuticals such as isoproterenol, hormones, as well as calorie consumption[60].

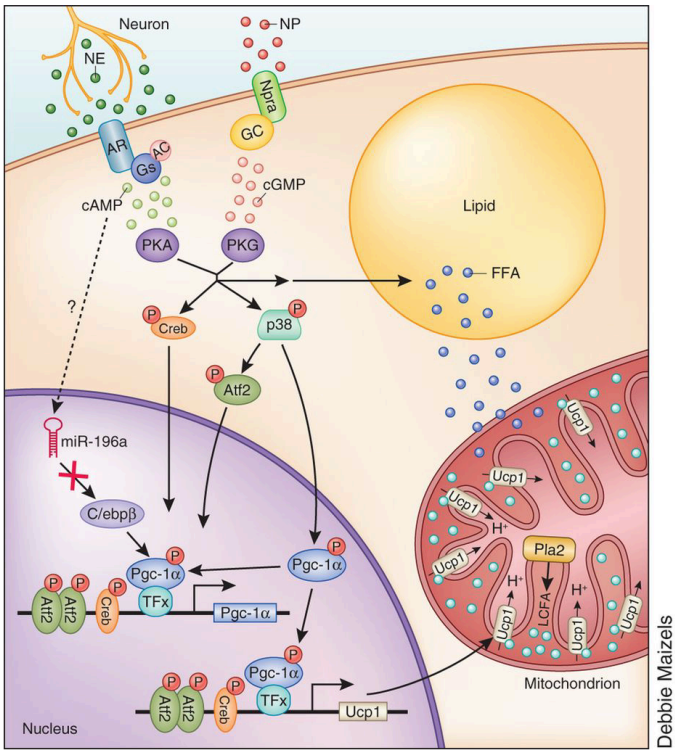

Figure 1: Activation of the adipocyte thermogenic program by the β-adrenergic receptor and natriuretic signalling pathway
Upon cold exposure, sensory nerves of peripheral tissues signal to the hypothalamus, which is responsible for the control of the sympathetic nervous system (SNS). This signalling process triggers the release of the catecholamine norepinephrine (NE) from nerve terminals in the adipose tissue that binds to β-adrenergic receptors (ARs). Natriuretic peptides (NPs) are produced in the heart and increase with cardiac wall stress, cold exposure, and exercise[61]. The binding of NE to ARs and NPs to the natriuretic peptide receptor A (Npra), both located on adipocytes, leads to the activation of signalling transduction cascades that result in the expression of thermogenic genes such as *uncoupling protein 1* (*Ucp1*). AC, adenyl cyclase; cAMP, cyclic adenosine monophosphate; cGMP, cyclic guanosine monophosphate; FFA, free fatty acids; GC, guanylyl cyclase; Gs, a G protein subunit; LCFA, long-chain fatty acids; P, phosphate; Gs, a G protein subunit; PKA, protein kinase A; PKG, protein kinase G. From Harms et al. (2013)[49]. Artwork by D. Maizels.

As the cell´s need for energy supply increases, the respiratory activity, often accompanied by an increase in mitochondrial mass, is enhanced to meet this demand[62]. During the process of adaptive thermogenesis, mitochondrial respiration increases, among other things, due to a partial uncoupling of the electron transport from ATP synthesis. In this way, energy is dissipated in the form of heat, consequently making it possible for the animal to adapt to the cold. In addition, this process can counteract obesity by decreasing the possibility of fat storage.

An increase in mitochondrial proliferation presents a challenge to the cells as mitochondrial biogenesis depends on the generation of products that are encoded by both the nuclear and mitochondrial genome[62]. These products are assembled into the complexes of the electron transport chain, the ATP synthase machine, and the

mitochondrial protein synthesis apparatus[62]. The coordinated expression of a diverse set of genes controls the challenge of orderly assembly of these mitochondrial complexes and the maintenance of mitochondrial DNA copy number[62].

An important factor in the assembly process is PGC1α. PGC1α leads to the expression of molecules responsible for the synthesis of components of the oxidative phosphorylation apparatus such as mtTFA — a mitochondrial transcription factor controlling the replication and transcription of the mitochondrial genome[63] — as well as UCP1-UCP3. UCP1-UCP3 regulate the uncoupling from the mitochondrial electron transport from ATP synthesis[64]. Moreover, PGC1α also activates the expression of nuclear respiratory factors, NRF-1 and NRF-2. Various genes are targeted by these two transcription factors many of which encode subunits of cytochrome oxidase, the ATP synthase complex, and enzymes of heme biosynthesis[65].

1.2.2.4 Brown adipose tissue as therapeutic target for human obesity

In adult mice, major BAT depots can be identified in the dorsal anterior region comprising the interscapular, cervical, and axillary BAT[66]. Interscapular BAT depots, with a molecular profile comparable to that of classical rodent BAT, can be found in infant humans as well[67]. For a long time, it was assumed that BAT would only exist in meaningful amounts in infants and regress and become metabolically negligible in adults. However, lately, positron-emission tomography (PET) imaging studies of glucose uptake have shown that substantial deposits of thermogenic fat reside in adult humans (in addition to interscapular BAT, also perirenal BAT and an adipose depot in the deep neck region can be detected)[41,68–71]. Therefore, estimations have been made that 50% of the population possibly possesses BAT in a thermogenically active form although it declines both with age and obesity[27,72].

Just like WAT, BAT as an endocrine organ produces different hormones such as batokines and lipokines. These hormones are involved in the regulation of the cross-talk existing between the brain and peripheral organs[73]. The analysis of marker gene expression in thermogenic tissues confirmed the expression of *UCP1*. However, several studies have suggested that some human depots have a molecular profile which is comparable to rodent BAT whereas other depots display a profile of adipocytes which are more similar to beige fat[41,48,74]. Enerback et al. (1997) demonstrated that the condition of certain strains of mice lacking UCP1 deteriorate under cold conditions[75]. In

contrast, another study has demonstrated that long-term adaptation to cold does not require UCP1[76].

Another trigger for BAT thermogenesis is high-calorie or high-fat diets[77] which depends on UCP1 function and can obstruct obesity[78]. Mice without BAT are highly susceptible to the development of obesity[79] while those with elevated brown and/or beige fat function are protected against several damaging metabolic effects of a high-fat diet, such as obesity and insulin resistance[80,81]. This beneficial effect was also observed in humans, in which increased levels of brown and beige fat activity correlated with a lean body type. These observations suggest that brown and beige fat could have an important protective role in the metabolism of humans[68–70,82]. Another factor that correlated with an improved metabolism in lean[83] and diabetic[84] subjects was reduction in ambient temperature. Moreover, treatment with β3-adrenergic agonists resulted in enhanced human BAT and beige fat activity and EE[83,85]. These studies have spurred enthusiasm for understanding how the catabolic properties of BAT can be harnessed for therapeutic purposes.

1.3 The non-coding genome

The term noncoding RNA (ncRNA) refers to RNA that does not code for protein. This does not mean, however, that these ncRNAs do not contain information or have a specific function. For a long time, it was assumed that the part of the genome, not translated in protein, was 'junk'. Only recently, with the help of transcriptome sequencing, it was discovered that only 1-2% of the mammalian genome codes for protein. More than 80% of the genome is transcribed into RNA, which results in the production of many ncRNAs[86,87]. These ncRNAs include microRNAs (miRNAs; small ncRNA molecules that are involved in silencing and post-transcriptional gene regulation processes[88]), piwi-interacting RNAs (piRNAs; small ncRNAs which are part of silencing processes in the germline or of the RNA-induced silencing complex (RISC)[89]), small nucleolar RNAs (snoRNAs; small RNA molecules that are known to regulate the modification and processing of other RNAs[90]) and other classes of yet-to-be discovered small regulatory RNAs as well as longer transcripts. Although the function of many of those ncRNAs is not yet discovered, they seem to act as a layer of internal signals that regulate different levels of gene expression in physiology and during development[91].

1.3.1 Long noncoding RNAs and genomic localization

Long noncoding RNAs (lncRNAs) are categorized as RNA transcripts that lack open reading frames and protein-coding potential[92,93]. In former days, lncRNAs were arbitrarily defined as transcripts longer than 200 nucleotides compared to other ncRNA species such as miRNA, piRNA, and small interfering RNA (siRNA). Similar to mRNA transcripts, most lncRNAs are transcribed by RNA polymerase II and undergo further steps of processing like splicing and polyadenylation. Initially, large-scale discovery of lncRNAs was performed with tiling microarray[94,95] and full-length RNA-sequencing[96]. Nowadays, epigenome analysis[97] and techniques like whole transcriptome RNA-sequencing (RNA-Seq) have led to the identification of even greater numbers of lncRNAs[98,99]. Although lncRNA numbers remain debated, RNA-Seq meta-analyses in human tissues identified >60,000 lncRNAs which surpassed the approximately 22,000 coding genes found in the same study[100].

Despite this progress, challenges still remain to accurately annotate and characterize lncRNA transcripts. In a recent study it has been shown, for example, that a transcript originally defined as a muscle lncRNA encodes a small protein in the cell[101]. With bioinformatics tools such as PhyloCSF, the coding potential of RNA transcripts can be predicted, which uses comparative genomic analysis of the coding probability of nucleotides across multiple species[102]. Next to PhyloCSF, other tools to assess coding potential can be applied such as Coding Potential Calculator (CPC)[103], PORTRAIT[104] and Coding Potential Assessment Tool (CPAT) which is advertised as being faster and more accurate than the aforementioned techniques[105].

In the genome lncRNAs can be categorized into sense, antisense, intronic, divergent, and intergenic groups based on their location relative to nearby protein-coding genes. The expression of lncRNAs is tissue-specific and strongly regulated during tissue development and in response to physiological signals[106–109].

1.3.2 Multifaceted control of gene expression by lncRNAs

In recent years, gain-and-loss-of function research has discovered several lncRNAs that are involved in diverse biological processes in almost all eukaryotes including animals, plants, and yeast[110–114]. LncRNAs can be localized in different areas of the cells such as the nucleus, the cytosol, or both[86] depending on their function in the regulation of

various biological processes such as transcription[115,116], cell differentiation[117,118], tissue development[119,120], and tumorigenesis/metastasis[106,121,122].

Furthermore, studies have shown different mechanisms through which lncRNAs are able to regulate gene expression (Figure 2). In the nucleus, lncRNAs can either function as transcriptional coactivators by direct interaction with transcription factors[123,124] or prevent the assembly of transcriptional complexes and thereby lead to the inhibition of gene expression[125,126]. Moreover, lncRNAs can exert their posttranscriptional effects on gene expression by assisting as molecular sponges for microRNAs as it has been shown for the lncRNAs *H19* as well as lincRNA-RoR[127,128].

One mechanism by which lncRNAs exert silencing of other genes is the recruitment of repressive chromatin-remodeling complexes, such as the Polycomb Repressive Complex 2 (PRC2) and the SWItch/Sucrose Non-Fermentable (SWI/SNF) complexes[115,129]. In this way, lncRNAs facilitate the recruitment of PRC2 to chromatin, possibly by building complexes with several components of the PRC2 complex such as Enhancer of zeste homolog 2 (EZH2), Jumonji, AT rich interactive domain 2 (JARID2), and Suppressor of zeste 12 homolog (SUZ12)[130,131]. Additionally, lncRNAs can also regulate post-transcriptional events during gene expression such as mRNA translation[132], splicing[133], and mRNA degradation[134].

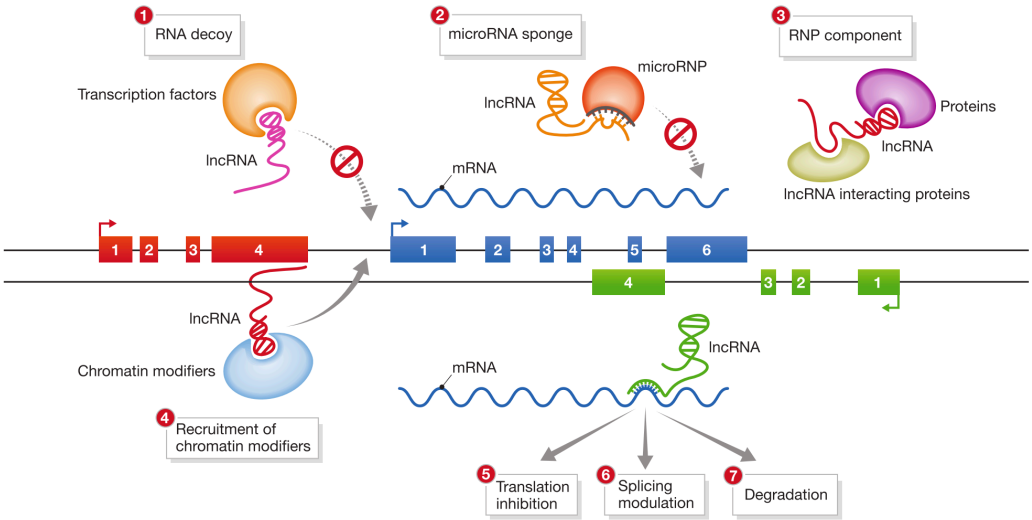

Figure 2: Multifaceted control of gene expression by lncRNAs
LncRNAs, a subclass of ncRNAs, stand out at being tissue- and species-specific and at exhibiting unique conservation patterns. They have been found to interact with DNA, other RNA molecules, and proteins to fulfil regulatory functions. These interactions can result in transcriptional regulation in which lncRNAs function as decoys for transcription factors (1) or miRNA sponges (2) and with that preventing them to bind to their mRNA target or by lncRNAs building ribonucleoprotein complexes (3). Moreover, lncRNAs can be involved in chromatin remodelling by recruiting chromatin modifiers (4) or by regulating post-transcriptional events (5), (6), and (7). From Hu et al. (2012)[135].

1.3.3 Metabolic regulation by lncRNAs

The regulation of nutrient and energy metabolism in mammals is controlled by reciprocal signaling between different tissues that primarily serve regulatory functions such as the CNS, the pancreatic islets, and metabolic tissues like adipose tissues, liver, and skeletal muscle[136]. Currently, we are faced with an increased rise of obesity in the world which is accompanied by a rise in obesity-associated diseases such as insulin resistance and T2DM[5]. A better understanding of the master regulator insulin which controls peripheral as well as central-nervous system-related aspects of metabolism is inevitable to understand whole-body metabolism[137].

A key step in the development of metabolic disease is resistance toward the metabolic effects of insulin. Interestingly, it has been shown that insulin and insulin-like growth factor 1 (IGF1) signaling also lead to changes in lncRNA expression[138]. This finding supports the hypothesis that lncRNAs may be involved in metabolic effects of insulin and progression of insulin resistance. Thus, a strong interest lies within the identification and understanding of new lncRNAs governing mechanisms in energy and glucose homeostasis at cell-intrinsic, organ, and whole-body levels.

1.3.4 Regulation of brown and beige adipocyte differentiation by lncRNAs

In the last years studies have focused on understanding and functionally dissecting the transcriptional and epigenetic regulation of BAT by protein-coding genes[139]. However, sequencing initiatives like ENCODE[140] project have recently demonstrated that RNA transcription is a phenomenon observed throughout the majority of genomes in higher organisms and that small noncoding RNAs (sncRNAs) such as microRNAs but also lncRNAs have important functions. The extent to which lncRNAs are involved in the regulation of brown/beige fat development, homeostasis and function is, however, still poorly understood. Yet, recent work on lncRNAs has led to the discovery of several candidates that may be involved in adipocyte biology.

Using whole transcriptome RNA-Seq, Sun et al. (2013) discovered a cluster of lncRNAs that exhibited differential expression during adipogenesis. This cluster contained several lncRNAs that appeared to be required for adipocyte differentiation[108]. One candidate, linc-RAP-1 (Firre), has been shown to interact with heterogeneous nuclear ribonucleoprotein (hnRNP) U[141]. Another brown fat lncRNA, Blnc1, identified by Zhao et al. (2014), has been shown to promote brown and beige adipocyte

differentiation and function[124]. Blnc1 is mainly localized in the nuclear compartment suggesting a role in transcriptional regulation. Mechanistically, *Blnc1* interacts with EBF2. EBF2 is a transcription factor that regulates adipocyte differentiation and brown fat development[142,143] and it forms a ribonucleoprotein transcriptional complex to induce the expression of genes involved in fuel oxidation and uncoupled respiration. The expression of Blnc1 itself is regulated by EBF2 by forming a feedforward regulatory loop that probably serves as a regulator for the thermogenic differentiation of adipocytes[142].

In a paper by Alvarez-Dominguez et al. (2015), a cluster of brown fat-enriched lncRNAs was identified by RNA-Seq analysis of transcriptomes from various adipose tissues[120]. One candidate, Lnc-BATE1, has been shown to be induced during brown adipocyte differentiation and more highly expressed in BAT as compared to WAT. Lnc-BATE1 appeared to be equally distributed between the cytosol and nucleus and physically interacts with the nuclear matrix factor hnRNP U; a factor required for brown adipocyte differentiation, as already shown for Firre.

Although several profiling studies have been performed to explore the regulation of lncRNA expression during thermogenic adipocyte development, the involvement of lncRNAs in adipocyte biology remains poorly understood. Therefore, future work is needed for understanding the role of these lncRNAs in adipocyte metabolism.

1.4 Genomic imprinting

Genomic imprinting is an epigenetic mechanism resulting in parent-of-origin specific monoallelic expression which affects less than 1% of all genes in eutherians[144]. It was first discovered in mammals in 1984 when pronuclear transplantation experiments revealed that both the maternal and paternal genomes are needed for the proper development of mouse embryos[145,146]. In addition, mouse genetic experiments showed that in specific regions of the genome, genes fulfil different functions when inherited maternally than when inherited paternally[147]. The phenomenon of genomic imprinting must have arisen with the development of the placenta around 125 million years ago[148]. However, a plausible explanation of this epigenetic process has not yet been brought forward. Because imprinted genes are monoallelically expressed, one might hypothesize that there are selective advantages for the evolution and maintenance of the organism. Two widely cited theories exist that give reason for the existence of the phenomenon of

genomic imprinting: the 'kinship theory' and the 'coadaptation theory' (for review, see Peters et al. (2014)[148]).

The kinship theory, also called the parental conflict hypothesis, states that there is a conflict of 'interest' between maternal and paternal genes in a fetus or infant at those developmental stages where it is reliant on the nutritional resources of the mother[148,149]. The idea of the kinship theory can be explained through the fact that mothers are able to bear and nurture progeny from several fathers. The consequence is that offspring from one female are equally related to their mother whereas the father is only related to a subgroup of the offspring. Due to the difference in relatedness, different interests of maternal and paternal genomes in the offspring emerge. To provide ideal fitness for the father it is beneficial for paternal genes in the fetus or infant to make maximal use of maternal resources without regard to the detrimental effects to other siblings or the mother. With this, siblings larger in size will be raised that have a better chance of survival and thereby secure the reproduction of the father´s genes. On the other hand, to provide optimal fitness for the mother, maternal genes in the fetus or infant should be reduced in demands for maternal resources, and thus provide the mother with better chances to raise more progeny. This hypothesis is in accordance with the observation that numerous paternally expressed genes (PEGs) enhance growth, whereas maternally expressed genes (MEGs) supress growth, which might also give a reason for adult phenotypes such as maternal care and social behaviour[148,150].

The coadaptation theory, in contrast, proposes that for optimization of fetal development and maternal provisioning and nurturing imprinted genes act co-adaptively[151]. The theory only refers to a subset of predominantely PEGs that are expressed in the placenta and the hypothalamus. During development of mammalian species, complex interactions happen between the fetus, the placenta, and the mother´s hypothalamus[148]. These interactions not only influence fetal growth and brain development but also the provision of maternal resources at prenatal and postnatal stages of development and postnatal maternal care. This is likely regulated by the parent-infant coadaptation through a selection of co-expression of genes both in the placenta and the hypothalamus of the mother[148]. One example for which this theory applies is the gene, *paternally expressed 3* (*Peg3*)[151].

Deregulation of imprinting, via (epi)mutations in individual imprinting genes or imprinted gene clusters, results in diverse imprinting disorders (IDs). IDs can affect growth, development and metabolism of an individual and often have a severe lifelong

impact on the person´s quality of life. Some examples of IDs are Prader-Willi´s, Beckwith-Wiedemann´s (BWS) and Angelman´s syndromes[152,153]. Interestingly, in Silver-Russell´s syndrome (SRS) it has been shown that the ID is due to defects in the *H19-Igf2* locus[154], a locus which is of great relevance to this thesis.

In spite of progress in understanding the molecular basis of imprinting, the etiology of IDs[155–157] and approaches to cure IDs[158], the question remains as to why some genes but not others are monoallelically expressed[149,159]. To date, it is not clear whether specific similarities between PEGs or MEGs as two differing gene sets exist at all, mainly because PEGs/MEGs represent a collection of genes with heterogeneous functions.

Interestingly, one consequence of ID in patients and also mouse models are metabolic sequelae, for instance altered adiposity, lipodystrophy and alterations in insulin sensitivity and EE[148]. All these processes are closely linked to BAT and WAT (dys)function.

1.4.1 Genomic imprinting and thermogenesis

To assure survival of newborn mammals, especially those progeny that are born nude, the maintenance of body temperature in the cold is vital. Newborn mice cannot regulate their own body temperature until one week after birth[160]. This makes them dependent not only on the mother to provide body heat but also on the litter staying together in the nest to conserve heat. In neonates the regulation of temperature is provided through the process of NST in BAT, which has evolved in mammals to overcome hypothermia[22]. During this process chemical energy is dissipated in the form of heat through mitochondrial brown fat UCP1[22]. Several genes have already been identified that affect BAT and possibly NST.

The *Gnas* cluster harbours two genes – *Gnas* (encodes the G protein α-subunit $G_s\alpha$) and *Gnasxl* (gives rise to a variant $G_s\alpha$ subunit known as XLαs). Normally, *Gnas* is known to be a biallelically expressed gene. However, it shows maternal expression in a few tissues[148]. *Gnasxl* on the other hand is a PEG depending on the tissue in which it is expressed[161,162]. Thus, both genes act antagonistically and have opposite effects on BAT metabolism with $G_s\alpha$ promoting and XLαs repressing the production of heat[161,163,164].

Two other PEGs have been shown to inhibit the differentiation of brown adipocytes: *Necdin* (*Ndn*) and *delta-like 1 homologue* (*Dlk1*)[165], although the role of *Dlk1*

in BAT differentiation before weaning is not clear[166]. However, Charalambous et al. (2012) could show that *Dlk1* as well as the PEG *Dio3* (encodes *deiodinase, iodothyronine type III*) are important for a second phase of BAT recruitment two weeks after birth. This stage was not recognized until recently and is necessary for thermoregulation when mice start to become independent of the mother by leaving the nest[166]. When *Dlk1* was overexpressed, BAT differentiation and β-adrenergic signalling was impaired, and overexpression of both *Dlk1* and *Dio3* even resulted in reduced *Ucp1* expression. Thus, through impaired thermogenesis and instable body temperature, BAT is defective in its response to cold. These data support the prediction of the kinship theory of imprinting that PEGs act to reduce thermogenic output and that MEGs on the other hand invest in increasing thermogenic output[148,167].

1.4.2 The lncRNA H19

In 1984, the imprinted RNA transcript *H19* was identified in a murine fetal liver cDNA library for clones containing mRNA sequences that decrease in expression after birth[168]. The clone which hybridized only to a fetal but not to an adult liver cDNA probe was designated *H19* based on its position as the 19th clone in row H. *H19* is expressed from the maternal allele in mouse and human[169,170] and transcribed by RNA polymerase II, capped, polyadenylated and spliced. However, it lacks conserved open reading frames (ORFs) between human and mouse[171] and is noncoding. The *H19* gene encodes a 2.3 kb noncoding mRNA which is strongly expressed during embryogenesis and consists of five exons and four introns which are shorter than most lncRNA genes, each less than 100 bp[172]. The *H19* locus harbours several transcripts, among them H19 which functions as a full lncRNA. Moreover, *H19* encodes two variants of microRNAs, *miR-675*[173] within its first exon, but also two antisense transcripts, 91H and HOTS[174].

H19 is part of an imprinted gene cluster, which is conserved on mouse chromosome 7 and human chromosome 11p15 (Figure 3). *H19* is located adjacent to the protein-coding gene, *insulin-like growth factor 2* (*IGF2*) which is an important fetal growth factor. *H19* and *Igf2* are oppositely imprinted and co-expressed in endoderm- and mesoderm-derived tissues during embryonic development, which suggests that they are regulated by a common mechanism. Both genes share regulatory sequences which control their expression, including two enhancers which are located 3' downstream of *H19*[175]. Furthermore, an imprinting control region (ICR) is located

between the two gene loci which exhibits differential methylation and controls the expression[176].

Although *H19* is noncoding, it is abundantly expressed during mammalian development in both embryonic and extraembryonic tissues. *H19* is expressed in the embryo and downregulated shortly after birth in all tissues except from skeletal muscle[177]. *H19* has various biological functions and a vast amount of reviews have been published which discuss research on *H19*. Prior reviews focus on topics such as *H19´*s regulation[178,179] or its broad role in cancer[180] specifically the role of *H19* to act either as an oncogene[181] or tumour suppressor[182–184]. In addition, its participation in the regulation of cell proliferation[185] and differentiation[173] has been investigated.

In the developing fetus, *H19* regulates several important genes that are part of the imprinting gene network (IGN). One of these genes is *Igf2* which is responsible for proper embryonic development[186]. Moreover, it has been shown to influence mouse growth independently of the mechanism co-regulating imprinted expression of *Igf2* and *H19*[187]. *H19* may influence the regulation of growth through at least two distinct mechanisms involving miRNAs. Sequences within exon 1 of *H19* are the source of microRNA *miR-675*, which is solely expressed in placenta and serves to suppress genes that promote placental growth, including *Igf type-1 receptor* gene (*Igf1r*)[188].

In addition, *H19* RNA acts as a sponge for *let-7* family microRNAs[188]. By binding to *let-7* microRNAs, *H19* has been shown to influence the expression of *let-7* target genes which end up promoting the differentiation of myoblasts[127]. Although *H19* is one of the most-well studied lncRNAs, based on its status as being the first lncRNA discovered and characterized and its participation in many known biological functions, to date, nothing is known about its involvement in BAT homeostasis.

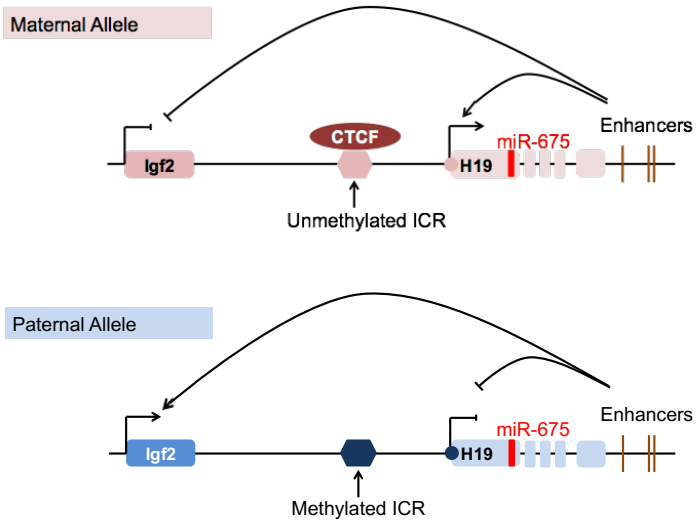

Figure 3: *H19-Igf2* imprinting gene cluster
The ICR of the paternal allele is DNA methylated. The ICR on the maternal allele is unmethylated and the insulator protein CTCF can bind and prevent enhancers from interacting with the *Igf2* promoter. Instead, the enhancers activate the expression of *H19*. On the paternal allele, DNA methylation prevents CTCF from binding to the ICR, and the enhancers activate *Igf2* expression.

1.4.2.1 Regulation of H19 expression

The expression of *H19* is regulated via genomic imprinting, an epigenetic phenomenon. *H19* is only expressed on the maternal allele and silenced on the reciprocal chromosome. The paternal allele is imprinted which means that the ICR region, which is located between *H19* and *Igf2*, is highly methylated, and thus silenced. The ICR, also called differentially methylated region (DMR), exhibits different methylation statuses depending on the origin of the parental chromosome. On the maternal allele, the ICR is hypomethylated and *H19* is expressed. *Igf2*, which is adjacent to *H19*, is imprinted and regulated in opposite direction: its expression is driven from the paternal allele and it is silenced on the maternal allele[189]. In normal circumstances, the ICR is hypermethylated at the paternal allele and hypomethylated on the maternal allele.

The mechanism that controls imprinting at this locus involves the binding of either Methyl-CpG-binding protein 2 (MeCP2) or CTCF depending on the methylation status of the *ICR*. The expression of *H19* is silenced through histone deacetylation by MeCP2 binding to methylated CpG dinucleotides. Afterwards, histone deacetylases (HDACs) interact with MeCP2 to silence *H19*[176]. On the maternal chromosome *H19* expression is not repressed by MeCP2 binding and can interact with its enhancer region. CTCF can bind to the ICR thereby preventing the expression of *Igf2*. The ICR and its methylation status are important for normal expression of *H19* and *Igf2*. Dysregulation

of this ICR, and thus abnormal expression of either *H19* or *IGF2* can have tremendous negative effects and result in various diseases as mentioned in **1.4**.

1.4.2.2 Regulation of gene expression by H19

To treat epigenetic abnormalities in different diseases, the activation or repression of *H19* could be an important epigenetic therapy[174]. One way in which *H19* acts as a guide to repress gene expression is through the interaction with epigenetic modifiers[174]. In a publication by Monnier et al. (2013) it has been shown that *H19* controls gene expression of maternal expressed genes (*Cdkn1c, Dcn, Meg3*) and paternal expressed genes (*Igf2, Dlk1, Slc38a4, Peg1*) or biallelically (*Gnas*) expressed genes of the IGN[190]. To control these genes *H19* interacts with methyl-CpG-binding domain protein 1 (MBD1), which is similar to MeCP2, a repressor of *H19*. MBD1 binds to methylated DNA and recruits HDACs and histone lysine methyltransferase (KMT)-containing complexes. These two complexes silence genes via H3K9 methylation resulting in chromatin compaction[190].

Despite its repressing function, *H19* can promote gene expression by interacting with epigenetic modifying enzymes. *H19* has been shown to bind hnRNP U, which is part of a complex with RNA polymerase II and a histone acetyltransferase P300/CBD-associated factor (PCAF). Histone acetylation resulted in an upregulation of genes within the *miR-200* family[191]. These studies show that *H19* can act either as repressor or activator of gene expression by being part of different epigenetic mechanisms. This underlines the multifaceted role of *H19* as a lncRNA on gene expression.

1.4.2.3 H19 in the regulation of diabetes

Blood sugar levels in the body need to be maintained at precise levels and the liver constitutes the major site of glucose regulation. If blood glucose is too low the alpha cells of the pancreas secrete glucagon. Glucagon stimulates the liver to release glucose and stimulates the production of more glucose through glycogenolysis. Elevated blood glucose levels stimulate glycogenesis by, increasing insulin release and causing glycogen to be produced from glucose. Insulin, generated in the β-cells of the pancreas, stimulates the liver and muscle to take up blood glucose resulting in a decrease of blood glucose levels. If these processes are dysregulated this can result in T1DM and T2DM[192].

Research shows evidence for *H19´*s involvement in T2DM. When cultured in the presence of insulin, smooth muscle cells have been shown to express a five-fold increase in *H19* than when cultured in media without insulin. This points to a response of *H19* to changes in insulin[193]. Moreover, it has been shown that mice with a whole-body knockout of *H19,* and thus biallelic expression of *Igf2*[194], are heavier compared to control animals[195] which results in improper growth after birth and a predisposition to T2DM[196].

Although the liver is a major site of insulin resistance in T2DM, some studies have also focused on the involvement of muscle and the pancreas. It has been shown that *H19* plays a role in both mice and humans suffering from T2DM in the muscle. *H19* was significantly decreased and shown to act as a decoy for the microRNA *let-7*[197]. Gao et al. (2014) showed that *H19* acts as a sponge that binds *let-7*, which interacts normally with *Insr* and *Lpl*, to inhibit the insulin-PI3K-mTOR pathway. *H19* downregulation in diabetic muscle resulted in limited binding of *let-7* and in increased inhibition of the pathway, consequently, promoting insulin resistance. Chronic downregulation of *H19* resulted in a dysregulation of glucose metabolism[197].

When researchers induced diabetes in pregnant females, pups received a high intrauterine exposure to glucose[198]. This resulted in a hypermethylation of the ICR in the pancreatic islets of the pups and consequently in the low expression of *H19* and *Igf2*. The low expression of *H19* and *Igf2* was even detectable in the sperm of these mice revealing a mechanism for the inheritance of childhood diabetes with *H19* as an important factor[198].

The studies discussed in this section show that *H19*, due to its diverse action in different tissues, impacts diabetes in a multifaceted fashion. However, more mechanistic studies examining the epigenetic profiles and changes of *H19* and *IGF2*—also in other tissues which have beneficial effects on whole body metabolism such as the BAT—are needed to fully reveal *H19´*s role.

1.5 Objectives

The aim of this study is to identify and characterise novel lncRNAs that favor energy dissipation by enhancing BAT metabolism. Obesity and T2DM represent two of the major health concerns of our society. The activation of BAT has been proposed as therapeutic target due to its unique property to convert dietary and stored nutrients like lipids and glucose directly into heat. LncRNAs have moved into the focus of attention as a novel class of noncoding RNAs due to their multifaceted control of gene expression. However, our knowledge of how lncRNAs control BAT differentiation and function in particular remains limited despite the progress in identifying and functionally characterizing lncRNAs involved in processes such as ageing[199], metabolic homeostasis[136,200], and AT biology[120,124,201,202].

Thus, this study aims to reveal candidate lncRNAs that can be used in the long-term as link for therapeutic options. In order to achieve this aim, we performed RNA-Seq to identify lncRNAs correlating with BAT function. Candidate lncRNAs were tested for *in vitro* functionality and gain-and-loss of function analysis of lncRNA *H19* was performed to unravel its effect on BAT biology *in vitro* and *in vivo*. To elucidate possible molecular effector circuits ChART-MS was applied to find *H19* associated proteins.

2 Materials and Methods

2.1 Materials

2.1.1 Technical Equipment

Machine	Manufacturer
Analytical balances, Quintix® 124-1S & Quintix® 612-1S	Sartorius AG, Göttingen, DE
Blood glucose monitoring system + sensors, Contour® XT	Bayer Healthcare, Leverkusen, DE
Cell culture cabinet, Scanlaf Mars, safety class II	LaboGene ApS, Allorød, DK
Centrifuge, 5810 R	Eppendorf AG, Hamburg, DE
CO_2-Incubator, C 170	BINDER GmbH, Tuttlingen, DE
CO_2-Incubator, Heracell™ 150i	Thermo Fisher Scientific, Waltham, US
Digital printer, P95DE	Mitsubishi Electric Corporation., Chiyoda, JP
Electrophoresis and blotting system, Mini-PROTEAN Tetra Cell	Bio-Rad Laboratories, Inc., Hercules, US
Electrophoretic transfer module, Mini Trans-Blot Cell	Bio-Rad Laboratories, Inc., Hercules, US
Fume cupboard, CC-30	Caspar & Co. Labora GmbH, Aachen, DE
Gel documentation system, FastGene® FAS V	Nippon Genetics Europe GmbH, Düren, DE
Gel electrophoresis chamber, PerfectBlue™ Mini	VWR International GmbH, Radnor, US
Homogenizer, FastPrep-24™ 5G	MP Biomedicals Germany GmbH, Eschwege, DE
Inverted microscope, DM IL LED	Leica Microsystems CMS GmbH, Wetzlar, DE
Laboratory freezer, Forma™ 88000	Thermo Fisher Scientific, Waltham, US
Laboratory freezer, LGex 3410 Mediline	Liebherr-International AG, Bulle, CH
Microcentrifuge, refrigerated, Micro Star 17R	VWR International GmbH, Radnor, US
Microplate reader, FilterMax™ F5	Molecular Devices, LLC, San José, US
PCR-Thermocycler, FlexCycler^2	Analytik Jena AG, Jena, DE
PhenoMaster, Automated Home Cage Phenotyping	TSE Systems GmbH, Bad Homburg vor der Höhe, DE
Platform shaker, Polymax 1040	Heidolph Instruments GmbH & Co. KG, Schwabach, DE
Power Supply, PowerPac™ HC	Bio-Rad Laboratories, Inc.,

	Hercules, US
Real-Time PCR System, QuantStudio™ 7 Flex	Applied Biosystems, Foster City, US
Refrigerator, KT 1730-26	Liebherr-International AG, Bulle, CH
Shaker, IKA® MS 3	IKA Werke GmbH & Co. KG, Staufen im Breisgau, DE
Spectrophotometer, NanoDrop™ ND-1000	NanoDrop Technologies, LLC, Wilmington, US
Thermoshaker, MKR 23	Hettich Benelux B.V., Geldermalsen, NL
Ultracentrifuge, Heraeus™ Megafuge™ 16R	Thermo Fisher Scientific, Waltham, US
Vortex mixer, Vortey-Genie 2	Scientific Industries, Inc., Bohemia, US
Water bath, model 1003	GFL Gesellschaft für Labortechnik mbH, Burgwedel, DE
Water purification system, Milli-Q® Advantage A10	Merck Millipore, Darmstadt, DE

2.1.2 General Materials

Material	**Manufacturer**	**Reference**
Cell Scraper [25 cm, 39 cm]	Sarstedt AG & Co., Nümbrecht, DE	83.1830, 83.1831
Cell strainer EASYstrainer™, 40 µm	Greiner Bio-One GmbH, Kremsmünster, AT	542000
Centrifugation tubes, Falcon®, polypropylene [15 ml, 50 ml]	Corning Corp., Corning, US	352096, 352070
Ceramic beads, Precellys® zirconium oxide beads, 1.4 mm	Cayman Chemical, Ann Arbor, US	03961-1-103
Chromatography paper, Whatman™	GE Healthcare, Chicago, US	3030-861
Cryo tubes, CryoPure®, 1.8 ml	Sarstedt AG & Co., Nümbrecht, DE	72.379.005
Disinfectant, Bacillol® AF	BODE Chemie GmbH, Hamburg, DE	9733803
Dispenser, Multipette® E3	Eppendorf AG, Hamburg, DE	4987000010
Dispenser-tips, Combitips advanced® [0.2 ml, 2.5 ml]	Eppendorf AG, Hamburg, DE	613-2059, 613-2062
Improved Neubauer hemacytometer chamber, 0.01 mm	W. Schreck, Hofheim am Taunus, DE	N/A
Multichannel pipette, Transferpette® S-8	Brand GmbH + CO KG, Wertheim, DE	703708
Needles, Sterican®, 0.45 x 12mm	B. Braun Melsungen AG, Melsungen, DE	4665457

Nitrocellulose western blotting membrane, Amersham™ Protran® Premium, 0,45 µm	GE Healthcare, Chicago, US	10600047
Optical 384-well reaction plate with barcode, MicroAmp™	Thermo Fisher Scientific, Waltham, US	4309849
Optical adhesive film, MicroAmp™	Thermo Fisher Scientific, Waltham, US	4311971
PCR lid strips, Multiply® 8-lid chain, flat	Sarstedt AG & Co., Nümbrecht, DE	65.989.002
PCR tubes, Multiply®-µStrip, 0.2 ml	Sarstedt AG & Co., Nümbrecht, DE	72.985.002
Petri dishes, 94 x 16 mm	A. Hartenstein GmbH, Würzburg, DE	PP90
Pipetboy, accu-jet® pro	Brand GmbH + CO KG, Wertheim, DE	26300
Pipettes, Transferpette® S Starter Kit	Brand GmbH + CO KG, Wertheim, DE	613-3478
Pipette-tips [10 µl, 200 µl, 1000 µl]	Greiner Bio-One GmbH, Kremsmünster, AT	771255, 739265, 686271
Pipette-tips, filtered [0.5-10 µl, 5-100 µl, 50-1000 µl]	Brand GmbH + CO KG, Wertheim, DE	732724, 732730, 732734
Pipette with tip, sterile [5 ml, 10 ml, 25 ml, 50 ml]	Greiner Bio-One GmbH, Kremsmünster, AT	606180, 607180, 760180, 768180
Precast gels, Mini-PROTEAN® TGX™,, 10-well [4-15 %, 7.5 %]	Bio-Rad Laboratories, Inc., Hercules, US	4561084, 4561023
Reaction tubes, SafeSeal® [0.5 ml, 1.5 ml, 2.0 ml]	Sarstedt AG & Co., Nümbrecht, DE	72.704, 72.706, 72.695.600
Syringes, Injekt®-F, 1 ml	B. Braun Melsungen AG, Melsungen, DE	9166017V
Tissue culture dish, TPP®, 15 cm	Sigma-Aldrich Chemie GmbH, Schnelldorf, DE	Z707694
Tissue culture plate, Falcon®, polystyrene [6-well, 24-well	Corning Corp., Corning, US	353046, 353047
Amicon Ultra-0,5 Centrifugal Filter Unit	Merck Millipore, Darmstadt, DE	UFC500324

2.1.3 Chemicals and Reagents

Chemical	Manufacturer	Reference
2-Propanol (isopropanol), for molecular biology, min. 99.5%	Sigma-Aldrich Chemie GmbH, Schnelldorf, DE	I9516
ß-Glycerophosphate disodium salt hydrate, min. 99%	Sigma-Aldrich Chemie GmbH, Schnelldorf, DE	G9422

ß-Mercaptoethanol, min. 99%	AppliChem GmbH, Darmstadt, DE	A1108
Acetic acid, glacial, min. 90%	VWR International GmbH, Radnor, US	BAKR9522
Agarose, for molecular biology	Sigma-Aldrich Chemie GmbH, Schnelldorf, DE	A9539
D-(+)-Glucose, min. 99.5%	Sigma-Aldrich Chemie GmbH, Schnelldorf, DE	G7021
Dynabeads® MyOne™ Streptavidin C1	Thermo Fisher Scientific, Waltham, US	65001
Ethanol absolut, AnalaR NORMAPUR®, min. 99.8%	VWR International GmbH, Radnor, US	20821.296
Ethylene glycol-bis(2-aminoethylether)-tetraacetic acid (EGTA), min. 99%	AppliChem GmbH, Darmstadt, DE	A0878
Ethylenediaminetetraacetic acid (EDTA), min. 98%	Sigma-Aldrich Chemie GmbH, Schnelldorf, DE	E6758
Formaldehyde solution 37%	AppliChem GmbH, Darmstadt, DE	A0823,0500
Glucose-solution 20 %, ad us. vet.	bela-pharm GmbH & Co. KG, Vechta, DE	2069.97.99
GlycoBlue™ Coprecipitant	Thermo Fisher Scientific, Waltham, US	AM9515
Hydrochloric acid (HCl), 37%	AppliChem GmbH, Darmstadt, DE	211020
Insulin solution, human recombinant, 9.5 - 10.5 mg/ml	Sigma-Aldrich Chemie GmbH, Schnelldorf, DE	I9278
Methanol, ROTIPURAN®, min. 99.9%	Carl Roth GmbH + Co. KG	4627.1
N-2-hydroxyethylpiperazine-N-2-ethane sulfuric acid (HEPES) buffer solution, 1M	Thermo Fisher Scientific, Waltham, US	15630049
Protease inhibitor tablets, Complete™ Mini	Roche Diagnostics, Rotkreuz, CH	4693159001
RNase inhibitor, RNasin® Plus	Promega GmbH, Mannheim, DE	N2511
Sodium acetate (NaAc), min. 99%	Sigma-Aldrich Chemie GmbH, Schnelldorf, DE	S5636
Sodium chloride (NaCl), pure	VWR International GmbH, Radnor, US	443827W
Sodium dodecyl sulfate (SDS), min. 99%	AppliChem GmbH, Darmstadt, DE	A1112
Sodium hydroxide (NaOH), AnalaR NORMAPUR®, solid	VWR International GmbH, Radnor, US	28244.295
Transfection reagent, Lipofectamine™ 2000	Thermo Fisher Scientific, Waltham, US	11668019

Trichlormethane (chloroform), min. 99.8 %	Carl Roth GmbH + Co. KG	4432.1
Tween® 20 (polysorbate), for molecular biology	VWR International GmbH, Radnor, US	437082Q

2.1.4 Commercialized test systems (Kits)

Kits	Manufacturer	Reference
DreamTaq Green DNA Polymerase (5 U/µl)	Thermo Fisher Scientific, Waltham, US	EP0714
High-Capacity cDNA Reverse Transcription Kit	Thermo Fisher Scientific, Waltham, US	4368814
MinElute PCR Purification Kit	QIAGEN N.V., Venlo, NL	28006
mirVana™ miRNA Isolation Kit	Fisher Scientific, Hampton, US	AM1560, AM1561
PCR Mycoplasma Test Kit	AppliChem GmbH, Darmstadt, DE	A3744
Pierce BCA Protein Assay Kit	Thermo Fisher Scientific, Waltham, US	23225
Seahorse XF Cell Mito Stress Test Kit	Agilent, Santa Clara, US	103015-100
SYBR™ Select Master Mix	Thermo Fisher Scientific, Waltham, US	4472903
TaqMan Gene Expression Master Mix	Thermo Fisher Scientific, Waltham, US	4369016
TURBO DNA-*free*™ Kit	Thermo Fisher Scientific, Waltham, US	AM1907

2.1.5 Buffer and Solutions

Buffer/Solution	Composition/Manufacturer	Reference
Bacillol	BODE (Hamburg, DE)	973380
Diethylpyrocarbonate (DEPC) H2O	0,1% (v/v) DEPC in H2O	
DNA gel loading dye, 6X	Thermo Fisher Scientific, Waltham, US)	R0611
DNA ladder mix, GeneRuler™	Thermo Fisher Scientific, Waltham, US	SM0331
dNTP Set, 100 mM Solutions	Thermo Fisher Scientific (Waltham, MA, USA)	R0182
Dream Taq Green Buffer (10x)	Thermo Fisher Scientific (Waltham, MA, USA)	B71
Erythrocyte lysis buffer	Qiagen (Hilden, DE)	79217
GeneRuler DNA Ladder Mix	Thermo Fisher Scientific (Waltham, MA, USA)	SM0332
GeneRuler DNA Ladder Mix	Thermo Fisher Scientific (Waltham, MA, USA)	SM0331
Laemmli sample buffer, 4X	Bio-Rad Laboratories, Inc., Hercules, US	1610747

Midori Green Advance DNA stain	Biozym Scientific GmbH, Hessisch Oldendorf, DE	617004
Ni-NTA Agarose	Thermo Fisher Scientific (Waltham, MA, USA)	R90115
Oil Red O Staining Solution	Sigma-Aldrich (St. Louis, MO, USA)	O1391-9
PageRuler™ Prestained Protein Ladder	Thermo Fisher Scientific (Waltham, MA, USA)	26616
Membrane staining solution, Ponceau S, 0.1 %	Sigma-Aldrich Chemie GmbH, Schnelldorf, DE	P7170
peqGOLD TriFast™	VWR (Darmstadt, DE)	30-2010
RNase Zap	Sigma-Aldrich (St. Louis, MO, USA)	R2020
TAE buffer (Tris-Acetate-EDTA buffer)	0.04 M Tris-Acetate, 0.001 M EDTA in H_2O	
Tail Lysis Buffer		
TaqMan Gene Expression Master Mix	Thermo Fisher Scientific (Waltham, MA, USA)	4369016
Tissue freezing medium	Leica Biosystems Nussloch GmbH, Nussloch, DE	14020108926
Trypan blue solution, 0.4%	Sigma-Aldrich Chemie GmbH, Schnelldorf, DE	T8154
Western blocking reagent, solution	Roche Diagnostics GmbH, Mannheim, DE	11921673001

2.1.6 Reagents for cell culture experiments

Reagent	**Manufacturer**	**Reference**
3-Isobutyl-1-methylxanthin (IBMX)	Sigma-Aldrich (St. Louis, MO, USA)	I5879-5G
3,3',5-Triiodo-L-thyronine (T3)	Sigma-Aldrich (St. Louis, MO, USA)	T2877
Biotin	Sigma-Aldrich (St. Louis, MO, USA)	B4639
Bovine Serum Albumine (BSA)	Sigma-Aldrich (St. Louis, MO, USA)	A8806-5G
CL-316,243	Sigma-Aldrich (St. Louis, MO, USA)	C5976
D(+)-Glucose-Monohydrat	AppliChem (Darmstadt, DE)	A3730
D-Pantothenic acid hemicalcium salt	Sigma-Aldrich (St. Louis, MO, USA)	P5155
Dexamethasone	Sigma-Aldrich (St. Louis, MO, USA)	D1756
DMEM/Ham's F-12 (1:1)	Merck (Darmstadt, DE)	FG4815
Dulbecco's Modified Eagle Medium (DMEM) (1x)	Thermo Fisher Scientific (Waltham, MA, USA)	11960-044
Dulbecco's Phosphate Buffered Saline (DPBS)	Thermo Fisher Scientific (Waltham, MA, USA)	14190-094

Fetal Bovine Serum (FCS)	Biochrom AG (Berlin, DE)	S0115
Indomethacin	Sigma-Aldrich (St. Louis, MO, USA)	I7378
Insulin solution human	Sigma-Aldrich (St. Louis, MO, USA)	I9278-5ML
L-Ascorbic acid	Sigma-Aldrich (St. Louis, MO, USA)	A4544-25G
L-Glutamine 200 mM (100x)	Thermo Fisher Scientific (Waltham, MA, USA)	25030-024
Lipofectamine® 2000 Reagent (1 mg/mL)	Thermo Fisher Scientific (Waltham, MA, USA)	52758
Minimum Essential Medium Non-Essential Amino Acids (MEM NEAA) (100x)	Thermo Fisher Scientific (Waltham, MA, USA)	11140-035
OPTI-MEM™ (1x)	Thermo Fisher Scientific (Waltham, MA, USA)	31985-062
Penicillin/Streptomycin	Thermo Fisher Scientific (Waltham, MA, USA)	15140-122
Rosiglitazone	Sigma-Aldrich (St. Louis, MO, USA)	R2408-10MG
Sodium Pyruvate 100 mM (100x)	Thermo Fisher Scientific (Waltham, MA, USA)	11360-039
Trypsin-EDTA (10x)	Thermo Fisher Scientific (Waltham, MA, USA)	15400-054

2.1.7 Antibodies

Protein target	Product no.	Company	Dilution
Calnexin	208-880	Calbiochem	1:5000
PGC1α	sc-13067	Santa Cruz	1:500
UCP1	sc-6528	Santa Cruz	1:500

2.1.8 List of utilized TaqMan assays

TaqMan	Full Gene Name	TaqMan ID
AdipoQ	adiponectin, C1Q and collagen domain containing	Mm00456425_m1
CD34	Cluster of Differentiation 34	Mm00519283_m1
Cebpα	CCAAT/enhancer binding protein (C/EBP), alpha	Mm00514283_s1
Cebpβ	CCAAT/enhancer binding protein (C/EBP), beta	Mm00843434_s1
Cidea	cell death-inducing DNA fragmentation factor, alpha	Mm00432554_m1
Ctcf	CCCTC-binding factor	Mm00484027_m1
Dcn	Decorin	Mm00514535_m1
Dio2	deiodinase, iodothyronine, type II	Mm00515664_m1
Dlk-1/Pref-1	Delta Like Non-Canonical Notch Ligand 1	Mm00494477_m1

Elovl3	elovl family member 3	Mm01194164_m1
Fabp4	fatty acid binding protein 4, adipocyte (AP2)	Mm00445878_m1
Gapdh	glyceraldehyde-3-phosphate dehydrogenase	Mm99999915_g1
Hprt	hypoxanthine guanine phosphoribosyl transferase 1	Mm00446968_m1
H19	H19, imprinted maternally expressed transcript	Mm01156721_g1
Igf2	Insulin-like growth factor 2	Mm00439564_m1
Lep	leptin	Mm00434759_m1
Mest	Mesoderm specific transcript	Mm00485003_m1
Nnat	Neuronatin	Mm00731416_s1
Pdgfra	Platelet Derived Growth Factor Receptor Alpha	Mm01211685_m1
Pdgfrb	Platelet Derived Growth Factor Receptor Beta	Mm01262489_m1
Peg3	Paternally expressed 3	Mm01337379_m1
Peg 10	Paternally expressed 10	Mm01167724_m1
Plagl1	Pleiomorphic adenoma gene-like 1	Mm00494251_m1
Pparγ	peroxisome proliferator activated receptor gamma	Mm01184322_m1
Pparg	Peroxisome proliferator activated receptor gamma	Mm01184322_m1
Ppargc1α	peroxisome proliferative activated receptor, gamma, coactivator 1 alpha	Mm01208835_m1
Runx2	Runt Related Transcription Factor 2	Mm00501580_m1
Ucp1	uncoupling protein 1	Mm01244861_m1

All TaqMan assays have been purchased from ThermoFisher Scientific, Waltham, US.

2.1.9 Indication of utilized miRNA TaqMan assays

miRNA TaqMan Assay	**TaqMan ID**	**Mature miRNA Sequence/Control Sequence (5' → 3')**
snoRNA429	001240	AAACAGTCTCCCTCTTCTGAATCTCGCT GAGGAAACTGCACGTCACCCTCCTGAAA
mmu-miR-675-5p	mmu482834_mir	UGGUGCGGAAAGGGCCCACAGU
mmu-miR-675-3p	mmu-miR-675-3p	CUGUAUGCCCUAACCGCUCAGU

2.1.10 Sequences of oligonucleotides used for qRT-PCR quantification of gene expression using SYBR method

Nucleotide oligo	Sequence (5´-> 3´)	Type
Adipoq_F	CGTGATGGCAGAGATGGCACTC	Adipogenesis (Late marker)
Adipoq_R	CCTTAGGACCAAGAAGACCTGCATC	
Afg3l2_F	GTTGATGGGCAATACGTCTGG	Mitochondrial Biogenesis
Afg3l2_R	GACCCGGTTCTCCCCTTCT	
CD24_F	TGCTCCTACCCACGCAGATT	Adipocyte Progenitor Marker
CD24_R	GCGTTACTTGGATTTGGGGAAGCA	
CD29_F	GGACCTTTTGGGTTGAGCTTATT	Adipocyte Progenitor Marker
CD29_R	AAAAAGTCTAACCCCCATATTGGA	
Cdkn1c_F	CCGGTCGAGGAGCAGAAT	Imprinted Gene (MEG)
Cdkn1c_R	TTCGACGCCTTGTTCTCCT	
Cox4i1_F	ACCAAGCGAATGCTGGACAT	Mitochondrial Biogenesis
Cox4i1_R	GGCGGAGAAGCCCTGAA	
Cox7a1_F	CAGCGTCATGGTCAGTCTGT	Mitochondrial Biogenesis
Cox7a1_R	AGAAAACCGTGTGGCAGAGA	
Cox8b_F	GAACCATGAAGCCAACGACT	Mitochondrial Biogenesis
Cox8b_R	GCGAAGTTCACAGTGGTTCC	
Cebpa_F	GAACAGCTGAGCCGTGAACT	Adipogenesis (Transcription Factor)
Cebpa_R	AAACCATCCTCTGGGTCTCC	
Drp1_F	CAGGAATTGTTACGGTTCCCTAA	Mitochondrial Fission / Fusion
Drp1_R	CCTGAATTAACTTGTCCCGTGA	
Fabp4_F	TTCGATGAAATCACCGCAGA	Adipogenesis (Late marker)
Fabp4_R	AGGGCCCCGCCATCT	
Fis1_F	AGAGCACGCAATTTGAATATGCC	Mitochondrial Fission / Fusion
Fis1_R	ATAGTCCCGCTGTTCCTCTTT	
Gata2_F	AACGCCTGTGGCCTCTACTA	Adipocyte Progenitor Marker
Gata2_R	TGCTGGACATCTTCCGATTC	
H19_F	AGTGATCGGTGTCTCGAAGAG	Imprinted Gene (MEG)
H19_R	CCTTCTGTCCTCTCCATCAC	
hnNctc1_F	CCCTATCTGCAATGTTTTCCT	Nuclear localisation marker
hnNctc1_R	GATGGTGCGTATTGTTGCTA	
Igf2r_F	ACACCTACTACTTGCGGGTC	Imprinted Gene (MEG)
Igf2r_R	ATAGATGGTTGTGGAGCGCT	
Ly6a_F	GTTTGCTGATTCTTCTTGTGGCCC	Adipocyte Progenitor Marker
Ly6a_r	ACTGCTGCCTCCTGAGTAACAC	
Mff_F	ATGCCAGTGTGATAATGCAAGT	Mitochondrial Fission / Fusion
Mff_R	CTCGGCTCTCTTCGCTTTG	
Mfn1_F	ATGGCAGAAACGGTATCTCCA	Mitochondrial Fission / Fusion
Mfn1_R	GCCCTCAGTAACAAACTCCAGT	
Mfn2_F	AGAACTGGACCCGGTTACCA	Mitochondrial Fission / Fusion
Mfn2_R	CACTTCGCTGATACCCCTGA	
Mrpl12_F	GCCACCGAAGGAGTGAAGC	Mitochondrial Biogenesis
Mrpl12_R	GGAGCGTAAGGCTGGCAAT	
Nctc1_F	CCACCAAAGCAGAAGACCAC	Imprinted Gene (PEG)

Nctc1_R	TGATAGTCCTGGTGTGGTGG	
Ndufaf2_F	CACGGACCATCTGGGGAAC	Mitochondrial Biogenesis
Ndufaf2_R	CTTTTCTCTCGAATAGTCTGCCC	
Ndufaf7_F	ATCTTCGGGGAGCTACTAGGG	Mitochondrial Biogenesis
Ndufaf7_R	ATGGCACAGGTCTTTAGCACA	
Ndufs2_F	TCGTGCTGGAACTGAGTGGA	Mitochondrial Biogenesis
NdufS2_R	GGCCTGTTCATTACACATCATGG	
Ndufv2_F	GGCTACCTATCTCCGCTATGA	Mitochondrial Biogenesis
Ndufv2_R	TCCCAACTGGCTTTCGATTATAC	
Nrf1_F	TATGGCGGAAGTAATGAAAGACG	Mitochondrial Biogenesis
Nrf1_R	CAACGTAAGCTCTGCCTTGTT	
Nrf2_F	CTTTAGTCAGCGACAGAAGGAC	Mitochondrial Biogenesis
Nrf2_R	AGGCATCTTGTTTGGGAATGTG	
Opa1_F	TGGAAAATGGTTCGAGAGTCAG	Mitochondrial Fission / Fusion
Opa1_R	CATTCCGTCTCTAGGTTAAAGCG	
Peg10_F	AGAGCAGCCAACCGAGAAG	Imprinted Gene (PEG)
Peg10_R	TCGTGGTTGGCGTCTTTTG	
Plagl1_F	TCGTCACCCTGGAGAAGTTC	Imprinted Gene (PEG)
Plagl1_R	ATCTTGTTGGGATCGTGGGT	
Polg_F	ATCTTGTTGGGATCGTGGGT	Mitochondrial Biogenesis
Polg_R	CAG GTA GGA CAC ACC CAT CT	
Ppara_F	AGAGCCCCATCTGTCCTCTC	Adipogenesis (Transcription
Ppara_R	ACTGGTAGTCTGCAAAACCAAA	Factor)
Pparg_F	GCATGGTGCCTTCGCTGA	Adipogenesis (Transcription
Pparg_R	TGGCATCTCTGTGTCAACCATG	Factor)
Ppargc1a_F	CCGATCACCATATTCCAGGT	Adipogenesis (Cofactor)
Ppargc1a_R	GTGTGCGGTGTCTGTAGTGG	
Ppargc1a_F	TATGGAGTGACATAGAGTGTGCT	Mitochondrial Biogenesis
Ppargc1a_R	CCACTTCAATCCACCCAGAAAG	
Prdm16_F	CACAGCACGGTGAAGCCATTC	Adipogenesis (Cofactor)
Prdm16_R	GGCGTGCATCCGCTTGTG	
Rnu6b_F	GCTCGCTTCGGCAGCACA	Nuclear localisation marker
Rnu6b_R	AACGCTTCACGAATTTGCGTG	
Sdha_F	GAACACTCCAAAAACAGACCTGC	Mitochondrial Biogenesis
Sdha_R	TCCACCACTGGGTATTGAGTAG	
Slc22a3_F	CCTGGATGACTTGCTTCGTG	Imprinted Gene (MEG)
Slc22a3_R	AGAGAAAGCTGGGCAGAGAG	
Ucp1_F	AGCTGTGCGATGTCCATGTAC	Uncoupling Protein
Ucp1_R	TGATGACGTTCCAGGACC	
Tgfb2_F	TGGAGTTCAGACACTCAACACA	Adipocyte Progenitor Marker
Tgfb2_R	GTTCCAGATCCTGGGACACA	
Uqcr10_F	CGAGCGAGCCTTCGATCAG	Mitochondrial Biogenesis
Uqcr10_R	ACAGTTTCCCCTCGTTGATGT	

If not stated otherwise all primers were designed using the Primer3web online tool. All primer oligonucleotides were purchased in 100 pmole stocks from Sigma-Aldrich Chemie GmbH, Schnelldorf, DE.

2.1.11 List of utilized Locked Nucleic Acid (LNA) GapmeR inhibitors

LNA Power Inhibitor	Sequence (5' → 3')	Manufacturer
Negative Control A, scr LNA	AACACGTCTATACGC	Exiqon (Vedbaek, DK)
H19_3 LNA, Imprinted Maternally Expressed Transcript (Non-Protein Coding)	GGCAAAGGATGAAGTA	Exiqon (Vedbaek, DK)
H19_2 LNA, Imprinted Maternally Expressed Transcript (Non-Protein Coding)	CCTTGCTGTAAAATC	Exiqon (Vedbaek, DK)

All LNA GapmeRs have been purchased from Exiqon A/S, Vedbaek, DK.

2.1.12 List of utilized small interfering RNAs (siRNAs)

LNA Power Inhibitor	Sequence (5' → 3')	Manufacturer
Negative Control A, scr LNA	GUCUCGUUCUGAAUCAAGAtt, UCUUGAUUCAGAACGAGACgg	Invitrogen

2.1.13 Enzymes

Enzymes	Manufacturer	Reference
Dispase II	Roche Diagnostics GmbH, Mannheim, DE	4942078001
DNAse I	Roche Diagnostics GmbH, Mannheim, DE	10104159001
Dream Taq DNA Polymerase	Thermo Fisher Scientific (Waltham, MA, USA)	EP0705
Proteinase K, recombinant, PCR grade	Roche Diagnostics GmbH, Mannheim, DE	3115844001
RNase A, DNase and protease-free (10 mg/ml)	Thermo Fisher Scientific, Waltham, US	EN0531

2.1.14 Software

Software	Manufacturer	Version
ImageJ	Wayne Rasband/NIH	version 1.48v
Keynote	Apple Inc.	version 8.0.1
Mendeley	Elsevier	Version 1.18
NanoDrop™ 1000 software	Thermo Fisher Scientific Inc.	version 3.8.1
Primer3web	web-based application, http://primer3.ut.ee/ [March, 2018]	version 4.1.0

Prism	GraphPad Software Inc.	version 7.0c
PyRAT	Scionics Computer Innovation GmbH	version 3.6-365
QuantStudio™ 6	Applied Biosystems	version 1.3

2.2 Cell biology methods

All methods described in this section were performed under a Mars Safety Class 2 Laminar Airflow Cabinet (LaboGene). Incubation steps were performed in a CO_2 Incubator CB 160 (Binder) at 37 °C and 5 % CO_2.

2.2.1 Mycoplasma test

Prior to usage, cells were tested for mycoplasma contamination using the PCR Mycoplasma Test Kit according to the manufacturer´s protocol. PCRs products of mycoplasma-positive samples are 270 bp in size. Cells were discarded if the test outcome was positive.

2.2.2 Cryoconservation

For cryoconservation, cells were expanded prior to freezing. Freezing medium (DMSO in growth medium 1:10) was prepared and stored on ice. The medium was aspirated and followed by a wash with 1x PBS. Subsequently, PBS was removed and 5 ml 1x Trypsin was added to each 15 cm plate. After a 10 min incubation at 37°C, 5 ml of growth medium was added and the cell suspension was transferred to a 15 ml tube and centrifuged at 1200 rpm for 5 min. The cell pellet was resuspended in freezing medium after aspiration of the medium. 1 ml of cell suspension was added to 1 cryotube (1x 15 cm plate was used for 3x cryotubes). The tubes were stored in a freezing container at –80 °C and transferred to liquid nitrogen after two weeks.

2.2.3 Reconstitution of cryopreserved stocks

For the reconstitution of cells from the cryopreserved stocks, growth medium was pre-warmed to 37 °C. 9 ml of growth medium was transferred to a 15 ml falcon tube and stored at 37 °C. The sample was kept on dry ice and 500 µl of pre-warmed growth medium was used for resuspension in warm growth medium. After thawing, cells were transferred to a 15 ml falcon tube and centrifuged at 1200 rpm for 5 min at room temperature (RTemp). The supernatant with DMSO was aspirated and discarded into DMSO-waste. After resuspension in 10 ml medium, the cells were plated in two different

concentrations (1:10 and 1:1,11). Afterwards, the cells were incubated at 37 °C with 5% CO_2. Cells were passaged every 2-3 days and split in a ratio of 1:10 or 1:20.

2.2.4 Primary immortalized brown pre-adipocyte (PIBA) cell line

2.2.4.1 Cultivation and passage of the PIBA cell line

Primary immortalized brown pre-adipocyte (PIBA) cells were generated in-house using standard protocols[203] and maintained in Dulbecco´s modified Eagle´s medium (DMEM) growth medium containing 4.5 g l^{-1} glucose supplemented with 10% fetal bovine serum (FCS), 1% L-glutamine, 1% penicillin/streptomycin (P/S), 1% minimum essential medium non-essential amino acids (MEM NEAA), and 1% sodium pyruvate. For passaging, cells were grown in growth medium until states of 80-90% confluency. At this stage, the medium was aspirated and cells cultured in 15 cm dishes were washed with 10 ml of 1x PBS. Next, cells were detached using 5 ml of 1x Trypsin, for which the plate was stored at 37 °C for 10 min. 5 ml of growth medium was added to stop the Trypsin activity, followed by transfer to a 15 ml falcon tube. The tube was centrifuged at 1200 rpm for 5 min and the supernatant was aspirated. 10 ml growth medium was used for pellet resuspension and cells were seeded in a ratio of 1:10 or 1:20. Cells were incubated at 37 °C and 5% CO_2 and passaged every 2-3 days at approximately 80% confluency. Modified after Schmidt et al. (2018)[204].

2.2.4.2 Induction of adipogenesis

Prior to the induction of adipogenesis, cells were grown until confluent in differentiation medium (DMEM, 20 nM insulin, 1 nM T3). The differentiation process to brown adipocytes was induced via one-day incubation in differentiation medium supplemented with 0.125 mM indomethacin, 2 mg/1 dexamethasone and 0.5 mM isobutylmethylxanthine and subsequent incubation in differentiation medium for 5 days. Modified after Schmidt et al. (2018)[204].

2.2.4.3 LNA mediated gene knockdown of PIBA cells

For transfection with LNA GapmeRs, cells were cultivated until confluent in differentiation medium (growth medium, 20 nM insulin, 1 nM T3). To carry out lncRNA-mediated inhibition, custom-made LNA GapmeRs (sequences are provided in **2.1.11**) were transfected once the cells reached confluency. Lipofectamine 2000 was diluted 1:62,5 in Opti-MEM. To achieve a final concentration of 25 nM, the appropriate LNAs (stock concentration 10 µM) were diluted 1:50 in Opti-MEM. After incubation of both solutions at RTemp for 5 min, LNA and Lipofectamine solutions were mixed at equal volumes and incubated for 20 min at RTemp. Pre-warmed PBS was used to wash the cells and 750 µl of growth medium without P/S was added to each well. 250 µl of the LNA/Lipofectamine mix was added and the cells were incubated for 24 h at 37 °C and 5% CO_2, before exchanging the medium to induction medium. Differentiation of brown adipocytes was induced using differentiation medium supplemented with 0.125 mM indomethacin, 2 mg/l dexamethasone and 0.5 mM isobutylmethylxanthine for 1 day, followed by incubation in differentiation medium for 5 more days. Modified after Schmidt et al. (2018)[204].

2.2.5 Primary cell culture

2.2.5.1 Isolation of adipose-depots specific stromal vascular fraction (SVF) cells

In order to isolate depot-specific SVF cells, the mice were sacrificed by cervical dislocation. Next, the interscapular BAT, posterior inguinal subcutaneous (scWAT), and perigonadal visceral (vWAT) tissue of 5-6 weeks old male C57BL/6 N or H19 TG mice was isolated and transferred into pre-warmed DMEM/Ham's F-12 medium without supplements. Tissue samples were pooled according to genotype and AT depot to obtain sufficient cell numbers for cultivation. In a sterile environment, the medium was aspirated before cutting the AT into 1 mm x 1 mm pieces to reach homogenized consistency. Homogenized tissue was collected in a 50 ml tube filled with 10 ml DMEM/Ham's F-12 medium without supplements. For debris removal, 5 ml of the lower aqueous phase was aspirated, 5 ml serum-free DMEM/Ham's F-12 medium was added, and in a final wash 5 ml of the infranatant was removed. 1 mg/ml Collagenase II, 1.5% BSA, 6.6 ml serum-free medium, and 100 µl DNase (15kU/ml) was prepared for each scWAT and vWAT sample. Each BAT sample received the aforementioned reagents as in

addition to 240 µl Dispase I (50 U/ml). To each AT preparation, 10 ml of the mixed enzyme solution was added. Next, the tubes were placed in a 37°C water bath and shaken at 120 rpm for 15 min. After vigorous inversion of the samples by hand, they were placed on a shaking incubator at 37°C for another 15 min at 120 rpm. For purification, the cell suspension was filtered through 100 µm EASYstrainer™ Cell Strainer into a 50 ml tube filled with 20 ml DMEM/Ham's F-12 growth medium (DMEM/Ham´s F12 medium plus 10% Fetal Calf Serum, 1% P/S, 0.1% Biotin, and 0.1% pantothenic acid). The suspension was centrifuged at 200 g at 21°C for 5 min. The supernatant was discarded and the pellets were resuspended in 1 ml growth medium and filled up to 10 ml. The cells were then centrifuged at 200 g for 5 min at 21°C and the medium was aspirated down to 1 ml, the pellet was resuspended and transferred into a 15 ml tube. Growth medium was added to reach 13 ml and centrifuged for 5 min on 21°C and with 200 g. Next, supernatants were aspirated and pellets were resuspended in 1 ml Erythrocyte Lysis Buffer for 5 min. Once again the tubes were filled up to 13 ml and centrifuged for 5 min at 21°C and with 200 g. The supernatant was aspirated down to 1 ml, which was used for resuspension of the pellet containing the SVF. The cell suspension was filtered through a 30 µm Partec CellTrics® filters (Sysmex Partec, Görlitz, Germany) dampened with 500 µl growth medium. After filtration, the filter was rinsed with 500 µl growth medium and isolated cells quantified using a Neubauer Counting Chamber to seed 50,000 cells/well in a flat bottom 24-well Falcon™ tissue culture plate. The cells were incubated at 37 °C with 5% CO_2 until confluenct and the medium was changed daily. Modified after Schmidt et al. (2018)[204].

2.2.5.2 Induction of SVF adipogenesis

To induce the SVFs isolated from scWAT and vWAT into mature adipocytes, a cocktail of freshly prepared 0.05% Insulin, 0.005% Dexamethasone, 0.001% Rosiglitazone, and 0.05% 3-Isobutyl-1-methylxanthin (IBMX) in growth medium (induction medium) was added to fully confluent cells. In order to induce BAT-isolated SVFs into mature adipocytes, a mix of freshly prepared 0.05% Insulin, 0.005% Dexamethasone, 0.001% Rosiglitazone, 0.05% 3-Isobutyl-1-methylxanthin (IBMX), 0.1% Indomethazine, and 0.001% Triiodothyronine in growth medium (induction medium) was added to fully confluent cells. After 48h of induction, cell differentiation was initiated using freshly prepared 0.0015% Rosiglitazone (scWAT and vWAT) or 0.001% Triiodothyronine

(BAT) in growth medium (differentiation medium) which was exchanged every 24h. After 48 -72h incubation with primary adipogenic differentiation medium, the vWAT and BAT were considered fully differentiated whereas scWAT usually differentiated after a 72-96 h incubation period. Modified after Schmidt et al. (2018)[204]. Details of the media composition are shown in **Table 1**.

Table 1: Composition of media used for primary cell culture

Media	Supplementation
Primary growth medium	10 % (v/v) FCS 1 % (v/v) Penicillin/Streptomycin 0.1 % (v/v) Biotin (stock 33 mM in 0.1 M NaOH) 0.1 % (v/v) D-Pantothenic acid (stock 17 mM in H2O) in DMEM/Ham's F-12 (1:1) (1x)
Primary brown adipogenic induction	1 µM Rosiglitazone 850 nM Insulin 1 µM Dexamethasone 250 µM IBMX 125 nM Indomethacin 1 nM T_3 in primary growth medium
Primary white adipogenic induction	1 µM Rosiglitazone 850 nM Insulin 1 µM Dexamethasone 250 µM IBMX in primary growth medium
Primary brown adipogenic differentiation	1 µM Rosiglitazone 1 nM T_3 in primary growth medium
Primary white adipogenic differentiation	1 µM Rosiglitazone in primary growth medium

2.2.5.3 LNA mediated gene knockdown of primary adipocytes

Primary brown adipocytes were isolated from depots-specific SVFs as described above. For lncRNA inhibiton, confluent cells were transfected with custom-made LNA GapmeRs (sequences are provided in **2.1.11**). Lipofectamine 2000 was diluted 1:62,5 in Opti-MEM. For a final concentration of 25 nM, the respective LNAs (stock concentration 10 µM) were diluted 1:50 in Opti-MEM. Both solutions were incubated for 5 min at room

temperature. LNA and Lipofectamine solutions were mixed at equal volumes and incubated for 20 min at RTemp. Cells were washed with pre-warmed PBS and 750 µl of growth medium without P/S was added to each well. 250 µl of LNA/Lipofectamine mix was added and cells incubated for 24 h at 37 °C and 5% CO_2 before exchanging for the induction medium. Modified after Schmidt et al. (2018)[204].

2.2.5.4 siRNA mediated gene knockdown of primary adipocytes

SiRNAs targeting *H19* (siH19, oligo n253571) or non-targeting Control (siCtrl, Cat. No. 4390843; both 100nmol/l, Invitrogen) were delivered into 1° BAT adipocytes by Amaxa nucleofection (Lonza Bioscience) according to the manufacturer´s protocol. Cells were utilized 48-72 h after transfection. SiRNA sequences are provided in **2.1.12**. Modified after Schmidt et al. (2018)[204].

2.2.5.5 Subcellular fractionation protocol

For subcellular localization analyses, RNAs were purified from nuclear and cytoplasmic fractions obtained using the PARIS kit (Ambion) according to the manufacturer´s protocol. Modified after Schmidt et al. (2018)[204].

2.2.6 Determination of oxygen consumption rates (OCR)

SVF from indicated AT depots were isolated and cells were seeded into Agilent Seahorse XFe96 Bioanalyzer microplates. 50,000 cells were seeded per well and incubated in DMEM/Ham´s F12 medium plus 10% Fetal Calf Serum, 1% P/S, 0.1% Biotin, and 0.1% Pantothenic acid (Growth medium) at 37 °C and 5% CO_2 in a standard incubator until confluent. For lncRNA inhibition cells were transfected as described in **2.2.5.3** in the Seahorse setup. For this, cells were washed with pre-warmed PBS and 75 µl of growth medium w/o P/S added to each well. 25 µl of LNA/Lipofectamine mix was added and cells were incubated for 24 h at 37°C and 5% CO_2 before changing the medium to induction medium. A cocktail of freshly prepared 0.05% insulin, 0.005% Dexamethasone, 0.001% Rosiglitazone, and 0.05% IBMX (scWAT and vWAT) or 0.1% Indomethazine, 0.001% Triiodothyronine (BAT) in growth medium (induction medium) was used to induce commitment of SVFs into mature adipocytes directly in the Seahorse microplates. After 48 h of induction, differentiation was initiated using freshly prepared 0.001% Rosiglitazone (scWAT and vWAT) and 0.001% Triiodothyronine (BAT) in

growth medium (differentiation medium). 3-4 days of incubation in differentiation medium was sufficient for cell differentiation. For each Seahorse plate the corresponding calibration plate was prepared 24 h prior to experiments, which contained 200 µl XF Seahorse Calibrant Agilent per well. The plate was incubated for 24 h in a non-CO_2 incubator at 37 °C and the instrument was set to 37 °C, 24 h before the start of the experiment. The cells were washed with PBS and the medium was exchanged an hour before the experiment, according to the corresponding experiment analysis kit (MitoStressKit, provided by the manufacturer). The calibration was carried out using calibration plates, measuring O_2, and pH LED Value/emission/Initial reference Delta for each well, before sample measurement. After calibration, cartridges were kept within the machine and the measurement of adipocyte-containing microplates commenced. The measurement parameters wereas follows: Mix: 3 min, wait 0 min, measure 3 min with each reagent´s effect assessed within 3 min (MitoStressKit) with a total duration of 18 min or 24 min per reagent injection. All measurements started with measuring basal values, followed by the injection of Oligomycin, FCCP, and Rotenone + Antimycin A (MitoStressKit).

For MitoStress Kits, corresponding media were freshly prepared before the experiment and consisted of Basal Seahorse Medium supplemented with 25 mM Glucose, 1 mM Glutamine, 2 mM Sodium Pyruvate, (pH = 7,4) that were filtered sterile. Subsequently, medium of the Seahorse cell plates was aspirated and 180 µl MitoStress medium was added 1 h prior to calibration. The plate was stored in a non-CO_2 incubator at 37 °C for 1 h. Part of the calibration plate was a cartridge with 4 pockets per well. Prior to measurement, pocket A was filled with 20 µl 10 µM Oligomycin, pocket B with 22 µl 10 µM FCCP, and pocket C with 25 µl 5 µM Antimycin A and Rotenone. Modified after Schmidt et al. (2018)[204].

2.3 Total RNA isolation

2.3.1 Trizol based method

Total RNA was isolated from primary adipocytes and tissues using peqGOLD TriFast™ (PEQLAB Biotechnologies). 500µl of peqGOLD TriFast™ was used for cells whereas 1 ml was used for isolated tissue sections. The samples were stored for 10 min at room temperature. Afterwards, the RNA was isolated according to the manufacturer´s

protocol. RNA was finally resuspended in 50 µl of DEPC-H_20 (0,1% DEPC). Subsequently, the concentration of RNA was quantified using a Nanodrop Spectrophotometer ND-1000 (Thermo Fisher Scientific).

2.3.2 miRVana kit

For RNA sequencing, RNA of tissues was isolated using the manufacturer´s instructions of the total RNA isolation procedure of the mirVana miRNA isolation kit.

2.4 Real-time quantitative RT-PCR (qRT-PCR)

2.4.1 Reverse Transcription from total RNA to cDNA

In order to convert single-stranded RNA molecules into double-stranded complimentary DNA (cDNA) molecules, total RNA solutions were subjected to reverse transcription using the High-Capacity cDNA Reverse Transcription Kit according to the manufacturer´s protocol. The synthesis of cDNA molecules in this protocol is based on random hexamer primers, which allow conversion of all possible RNA sequences. For the preparation of the reaction, 1 µg of total RNA in 10 µl was added to the master mix indicated in the table below.

Table 2: Composition of RT master mix for total cDNA.

Reagent	Volume[µl]
10x RT buffer	2,0
dNTPs	0,8
Random hexamer primers	2,0
H_20	4,2
Reverse Transcriptase	1,0

Reverse transcription of total RNA was performed in FlexCycler^2 PCR cycler using the following program:

Primer annealing	25°C	10´
Reverse transcription	37°C	120´
Enzyme inactivation	85°C	5´
Final hold	4°C	∞

After the RT-PCR reaction, 180µl MPW was added to the cDNA and stored at -20°C or directly used for RNA expression analysis in quantitative PCR (qRT-PCR) experiments.

2.4.2 Quantitative RT-PCR (qRT-PCR) analysis

For quantification of the expression of specific RNA molecules, cDNA was subjected to quantitative PCR (qRT-PCR) analysis using a QuantStudio™ 7 Flex Real-Time PCR System. For RNA molecules with commercially available gene expression assays, the TaqMan Gene Expression Master Mix was used in combination with the respective transcript-specific TaqMan Gene Expression Assays. For other genes, the SYBR™ Select Master Mix was used in combination with self-designed and DNA primers tested for good quality.

TaqMan- based qRT-PCRs

6 µl	TaqMan Master Mix
0,3 µl	TaqMan probes
4 µl	cDNA solution

SYBR Green-based qRT-PCRs

5 µl	SYBR Select Master Mix (10x)
4 µl	cDNA solution
1 µl	SYBR primer mix (5 µM)

qRT-PCR program

Initial Denaturation	95°C	2 min	
Denaturation	95°C	30 sec	
Annealing	60°C	30 sec	40x
Elongation	72°C	1 min	
Final Elongation	72°C	5 min	
Hold	4°C		

The relative abundance of mRNAs was calculated using comparative methods ($2^{-\delta\delta CT}$) according to ABI Relative Quantification Methods. Transcript levels of mRNAs were normalized to hypoxanthine phosphoribosyltransferase 1 (*Hprt1*) expression. *Hprt* abundances were unaffected across all experimental conditions. SYBR primer sequences are provided in **2.1.10** and utilized TaqMan assays in **2.1.8**.

2.4.3 Reverse Transcription of microRNAs and qRT-PCR

For reverse transcription of particular miRNAs, the samples were diluted 1:50 to have a concentration of 4 ng/µl and added to the master mix, shown in the table below.

Reagents of the High Capacity cDNA Reverse Transcription Kit were used. The list of miRNA RT primers can be seen in the Materials section.

Reagents	
0,15 µl	100mM dNTPs
1 µl	MultiScribe RT
1,5 µl	10x RT buffer
1 µl	of each TaqMan MicroRNA RT primer
5 µl	total RNA sample
up to 15 µl	DEPC-H_20

Reverse transcription of total RNA was performed in FlexCycler^2 PCR cycler using the following program:

Primer annealing	16°C	30´
Reverse transcription	42°C	30´
Enzyme inactivation	85°C	5´
Final hold	4°C	∞

After the RT-PCR reaction, 75 µl MPW was added to 15 µl of the RT product and stored at -20°C or directly used for RNA expression analysis in quantitative PCR (qRT-PCR) experiments. For quantification of the expression of specific RNA molecules, cDNA was subjected to quantitative PCR (qRT-PCR) analysis using a QuantStudio™ 7 Flex Real-Time PCR System. 9,5 µl of the RT product was transferred to the 384-well plate and 10,5 µl of the Master mix was added.

TaqMan MircoRNA assay- based qRT-PCRs	
10 µl	TaqMan Master Mix
0,5 µl	TaqMan probes
9,5 µl	cDNA solution

qRT-PCR program

Initial Denaturation	95°C	2 min	
Denaturation	95°C	30 sec	
Annealing	60°C	30 sec	40x
Elongation	72°C	1 min	
Final Elongation	72°C	5 min	
Hold	4°C		

2.5 RNA sequencing

2.5.1 Mouse RNA isolation

RNA of tissue samples for RNA sequencing was isolated using the miRVana Isolation Kit following the protocol for total RNA isolation. RNA concentration and integrity was assessed using the Experion Bioanalyzer system (Bio-Rad) according to the manufacturer´s instructions. Furthermore, contaminating DNA was removed using the TURBO DNA-free™ kit following the manufacturer´s protocol.

2.5.2 Deep RNA-Sequencing procedure

Library preparation and sequencing was performed at the Max Planck-Genome-Centre Cologne, Germany. Quality checks were carried out for 4°C-exposed versus 22°C-exposed samples as well as the CD versus HFD BAT samples. To do so, 1 µg of total RNA of each sample was depleted for rRNA using the NEBNext® rRNA depletion Kit (human/mouse/rat). For library preparation NEBNext Ultra™ Directional RNA Library Prep Kit for Illumina (New England Biolabs) was used. All libraries were sequenced in parallel on a HiSeq2500 instrument (Illumina) in 2 x 100bp sequencing mode. Modified after Schmidt et al. (2018)[204].

RNA sequencing experiments were performed at the Cologne Center for Genomics, Cologne, DE with the following conditions:

Sample input	2 µg of total RNA
rRNA depletion	Ribo-Zero rRNA Removal Kit (Illumina)
cDNA library preparation	TruSeq RNA Library Prep Kit v2 (Illumina)
Normalization	ERCC RNA Spike-In (ThermoFisher)
Sequencing Platform	HiSeq2500, paired-end flow cells
Sequencing condition	2 x 100bp read length, strand specific
Sequencing depth	50-100 million reads per sample

2.5.3 Data processing of deep RNA-Sequencing

RNA-Seq data were processed using the QuickNGS analysis pipeline[205], version 1.2.7, based on Ensembl release 87. Reads were mapped to the GRCh38 assembly of the human genome using Tophat2, version 2.0.10, and reassembled with Cufflinks, version 2.1.1. Differential gene expression was analysed using the DESeq2 package, version

1.10.1. Finally, the results were uploaded to the QuickNGS database and combined with multiple annotations using the biomaRt package. Modified after Schmidt et al. (2018)[204].

2.6 Protein biochemistry

2.6.1 Protein isolation

For protein isolation, the medium of cells was aspirated and the plates were stored on ice. The cell monolayer was washed gently 1x with ice-cold 1xPBS and the excess was aspirated. 50 µl of RIPA lysis buffer with inhibitors was added to each well of the 24-well plate. RIPA buffer was composed of 50 mM Tris-HCl pH 8,0, 150 mM NaCl, 1% NP-40 (IPEGAL CA-630), 5 mM EDTA, 0,5 % sodium deoxycholate, 0,1 % of 10% SDS, 0,2 M β-glycerol phosphate, and 1 protease inhibitor tablet (cOmplete, Roche Diagnostics) for 10 ml of buffer. An ice-cold cell scraper was used to scrape the cells. The lysate was transferred to 1,5 ml Eppendorf tubes. The samples were snap-frozen in liquid nitrogen and thawed on ice for three repeated cycles. After 10 min of centrifugation at 12,000 g and 4°C the supernatant was transferred to fresh tubes and stored at -80 °C.

2.6.2 Protein concentration measurements

Protein concentration was determined following the manufacturer´s instructions of the Pierce BCA Protein Assay Kit.

2.6.3 Sodium dodecyl sulfate polyacrylamide gel electrophoresis (SDS-PAGE)

Samples were separated by SDS-PAGE after being mixed 1:4 with 4x Laemmli Sample Buffer (Bio-Rad) containing 10% β-mercaptoethanol and heated to 95 °C for 5 min. 20-40µl of protein was loaded in 4-15% gradient gels depending on the concentration of the protein. PageRuler™ Prestained Protein Ladder (ThermoScientific) was used as ladder. The SDS-gel was run for about 1h in 1x SDS running buffer at 100V. Afterwards, proteins were transferred to a nitrocellulose membrane for incubation with primary antibodies. For the transfer, 1x transfer buffer + 20% methanol was prepared. The membrane, gel, whatman papers, and sponges were pre-wet in transfer buffer. The cassette was set up in the following order: black part of the cassette, sponge, 3 wet whatman papers, gel, membrane, 3 whatman papers, sponge, and finally the holder, which was closed. After every step, bubbles were removed. Blotting was performed in cold conditions for 2-3h at

0,2 Am/gel. After protein transfer, the membrane was incubated with Ponceau S for approximately 2 min to check for protein abundance. Ponceau S was discarded and the membrane was rinsed with MPW. A picture was taken. Afterwards, the membrane was incubated with 20 ml of blocking solution for one hour under permanent shaking. Following overnight incubation with 10 ml of the respective primary antibody solution (9,5 ml TBST, 500µl of Blocking reagent, and appropriate amount of primary antibody) at 4°C and permanent shaking, the membrane was washed with 1x TBS-T for 3x 10 min at RTemp and shaking. Afterwards, the membrane was incubated in solution containing secondary antibody (19 ml TBST, 1ml Blocking reagent and appropriate amount of secondary antibody) for 1h at RTemp and shaking. Another washing step followed as before and 1 ml of ECL Western Blotting Substrate (ThermoFisher) (mix 1:1) was applied on the membrane. The cheminoluminescence was detected using the Agfa Curix 60 x-ray developing machine.

10x SDS-Running Buffer (1L)

144,2 g	Glycine [1,92 M]
30,3 g	Tris base [250mM]
50 ml	20% SDS [1%]
up to 1L	Millipore H_20

10x Wet transfer buffer (1L) for 1x+20%MeOH

29,15 g	Glycine [390mM]
58,1 g	Tris base [480mM]
18,5 ml	20% SDS [0,37%]
up to 1L	Millipore H_20

10x TBST (1L) pH=8,00

60,5 g	Tris base [500mM]
87 g	1,5M NaCl
5ml	0,5% Tween
up to 1L	Millipore H_20

Blocking solution

18 ml	1x TBST
2 ml	Blocking Reagent

2.6.4 Stripping and reprobing western blot membranes

Stripping buffer (see below) was pre-warmed to 50°C and transferred to a small plastic box with a lid. The membrane was added and incubated at 50°C for up to 45 min with

some agitation. The solution was disposed of as required for β-mercaptoethanol based buffers and the membrane rinsed under running water tap. The membrane was washed extensively for 5 min in TBST and therewith it was ready for blocking stage.

Harsh stripping buffer (0,1L)

20 ml	SDS 10%
12,5 ml	0,5 M Tris HCl pH 6,8
67,5 ml	MPW
add 0,8 ml	β-mercaptoethanol under the fumehood

2.7 Immunohistochemistry

2.7.1 Oil Red O staining

The Oil Red O (ORO) solution was prepared by dissolving 0.3 g ORO dye was dissolved in 60 ml isopropanol in the dark at RTemp overnight. Afterwards, 40 ml dH_20 was added and the solution was filtered. Cell media was aspirated under a fume hood and the cells were rinsed with 2 ml of sterile PBS per well. Subsequently, PBS was aspirated and the cells were incubated for 1.5 h at RTemp in 1 ml 10% formalin. Next the excess formalin was removed; wells washed with 2 ml PBS and stained with 1 ml ORO staining solution for 2 h. The stained cells were washed twice with dH_20 for 5 min before acquiring images. Modified after Schmidt et al. (2018)[204].

2.7.2 Hematoxylin and eosin staining

Haematoxylin and eosin (H&E) stainings were performed by the histology facility of the Max-Planck Institute for Metabolism Research. BAT, scWAT, vWAT and liver specimens were incubated at 4°C in 4% paraformaldehyde overnight, embedded in paraffin (FFPE), and sliced according to standard protocols. H&E staining and insulin immunohistochemistry were performed after de-paraffination as previously described[206]. A Zeiss Axioskop 40microscope (Carl Zeiss MicroImaging) and Zeiss AxioVision 4.2 software (Carl Zeiss MicroImaging) were used for the imaging. Modified after Schmidt et al. (2018)[204].

2.7.3 Automated adipocyte quantification

H&E stainings were carried out as described above. The adipocyte quantification was performed by the CECAD Imaging facility. An automated workflow was utilized to

segment and measure adipocytes from the images. First, the interactive learning and segmentation toolkit ilastik[207] (www.ilastik.com) was used to train tissue specific pixel-level classifiers on the RGB photomicrographs. For classification of BAT, three classes were defined (membrane, vacuole, nucleus) and a classifier using a set of eleven optimized features selected by the filter method was trained based on a manually labelled training dataset. For images from scWAT and vWAT a unified classifier was trained with just two classes (membrane and vacuole) and using all available features. Application of the classifiers to the respective image sets resulted in two or three class probability maps which were fed in Cellprofiler[208] to segment and individually measure single adipocytes. The vacuole probability map was smoothed and automatically thresholded. The obtained binary vacuole mask was subjected to morphological closing to fill small holes. The result was used to mask the original vacuole probability image which then was used to perform intensity/probability based cell segmentation by means of the Cellprofiler Identify Primary Objects module. The cell masks were expanded until touching their neighbouring cells and cells intersecting with the image border before expansion were excluded. Size and shape parameters of the remaining cells were measured. Modified after Schmidt et al. (2018)[204].

2.7.4 Electron microscopy and mitochondrial morphometry

To fix tissues, the specimens were cut into small (~1 mm^3) pieces and stored in fresh fixative (10 ml Caco-buffer, 1.6 ml of 25 % Glutardialdehyde, 5 ml of 8 % PFA in H2O, filled up to 20 ml with DEPC-treated H2O with pH-value adjusted to 7.3) for 16-24 h at 4° C. Electron microscopy (EM) and mitochondrial morphometry was performed by the CECAD imaging facility. In order to embed the fat tissue, samples were washed 4x for 20 min in 0.1 M Caco-buffer (pH=7.2-7.3) at 4° C and incubated in 2 % OsO_4 in 0.1 M Caco-buffer (pH=7.2-7.3) at 4° C in the dark for 2h. Afterwards, samples were washed in 0.1 M Caco-buffer (pH=7.2-7.3) 4x for 20 min at 4°C. They were then incubated in ice-cold 50% EtOH for 20 min at 4° C to dehydrate them. Subsequently, samples were stored in ice-cold 70% EtOH at 4°C overnight which was followed by a 20 min incubation in ice-cold 90% EtOH at 4°C the next day. After that, samples were stored 3x for 20 min in ice-cold 100% EtOH at 4°C, 20 min in equal volumes of Propylenoxide:EtOH at 4°C, and 2x 20min in pure Propylenoxide at 4°C. For sample transfer to epon (20 g Epoxy, 11 g DDSA, 9 g NMA, 0.8 g DMP30, freshly prepared) samples were stored for 5 h in equal volumes of Epon:Propylenoxide at 4°C. Afterwards, samples were incubated in 3:1

volumes of Epon:Propylenoxide overnight at 4°C. On the next day, samples were immersed in fresh epon for 2 h with an open lid. The final embedding was performed in flat form in fresh epon for 72 h at 62 °C, subsequent too which, semi-thin sections (500 nm) were cut using a Leica UC6 ultramicrotome as a quality control check for for the samples. If the sections were of good quality, ultrathin sections were produced. The sections were fit to the grid and contrasted. The grid was incubated for 15 min in 1.5% aqueous Uranylacetate, washed 5x in distilled H_2O, incubated again for 4 min in lead citrate, and washed 5x in distilled H2O. Finally, samples were checked with electron microscope Jeol 2100 Plus equipped with a Gatan camera. Modified after Schmidt et al. (2018)[204].

2.8 Capture hybridization analysis of RNA targets (ChART) – Mass spectrometry (MS)

2.8.1 ChART

PIBA cells were seeded and either grown to confluency or induced to differentiate. The cells were fixed with 1% Formaldehyde for 10 min after a wash with 1x PBS. The fixation was quenched with 0.125 M Glycine, followed by another wash with ice-cold 1x PBS, scraped off, and centrifuged for 5 min at 100 g. The supernatant was aspirated and cells stored at -80 °C. The cells were lysed in 400 µl lysis buffer, resuspended, and stored on ice for 5 min. This step was repeated with an addition of 0.1% of NP-40 to the lysis buffer. 1ml of sucrose buffer was pipetted into a new tube and the lysed cells (max. 400 µl) were carefully pipetted into the center of the buffer which were centrifuged for 10 min at 7,000g at 4°C. The lysis step was repeated with only 400 µl of lysis buffer and afterwards the sucrose step was repeated. After centrifugation, the supernatants were discarded and the nuclei were washed with 1ml PBS. The tube was centrifuged for 1 min at 7,000 g, the supernatants were discarded, and 1ml of PBS was added. The suspensions were resuspended and vortexed to achieve a single nucleus suspension. 2% formaldehyde was added to crosslink the nuclei for 30 min and the tubes were vortexed and stored for 30 min on a rotating wheel at RTemp. For quenching, 0.125 M Glycine was added and the samples were centrifuged for 1 min at 7,000 g at 4°C. Prior to another centrifugation step at 7,000 g for 1 min, the supernatant was discarded and the nuclei were washed with 1ml PBS. Washing was repeated with 2 min of centrifugation in between. The supernatants were discarded and 300 µl nuclear lysis buffer and RNAse

inhibitor were added. The samples were vortexed and incubated for 5 min on ice. PBS and protease inhibitor were added in equal amounts to the nuclear suspension and vortexed. A tip sonicator was used to lyse the residual nuclei, with the following settings: 3x cycles 10%, 3x 10 sec, POWER 10%. The suspension was transferred into Diagenode TPX microtubes and sonicated with following conditions: Amplitude: 35%, 15 sec ON, 15 sec OFF, 36 cycles, time: 9 min for appropriate shearing of mature brown adipocyte chromatin. This was followed by a centrifugation at 17,000 g for 5 min and the supernatants were transferred to new tubes. Gross nucleic acid abundances were quantified using a Nanodrop instrument and 75 µg chromatin mixed with RNAse inhibitor and 650 pmol of oligonucleotides (OGNs) was conjugated to Biotin-TEG. (Biotin-TEG increases OGN–biotin distances to approximately 15 atoms using a triethyleneglycol (TEG) spacer. Biotin-TEG is used to avoid steric hindrances and improve attachment of OGNs to the beads). The samples were vortexed carefully and spun down, incubated at 55 °C while shaking at 600 rpm for 10 min. The temperature was decreased to RTemp and the samples stored o/n at 55 °C. The beads were mixed with 1 ml of Solution 1 (1 M NaCl and 0.1% Tween), vortexed, centrifuged shortly, and transferred to a magnetic rack. After a three-fold wash with Solution 1, the samples were adjusted to 1 M NaCl, vortexed, and 50 µl of beads and RNase inhibitor was added to the solution. The tubes were stored on a rotator for 30 min at RTemp, centrifuged, incubated on the magnetic rack, and the supernatants were discarded. The next wash step consisted of a 2x wash with 1ml of Solution 1 and 3x with 1ml of Solution 2 (1M NaCl, 0.1% Tween, 0.1% SDS). For this, solutions were added, the tubes were vortexed and stored on a shaker 1050 rpm set to 16 °C for 5 min. After an incubation step on the magnetic rack, the supernatant was discarded. For the final elution, the beads were resuspended in 300µl elution buffer (0.2 M NaCl, 0.1% SDS, 10 mM Tris pH=8.0) and 1x proteinase inhibitor. The samples were incubated on a ThermoShaker for 4-5 h and shaken at 1450 rpm at 65 °C. Finally, the eluate was concentrated with Amicon Ultra-0,5 Centrifugal filter. To degrade RNA contaminations, samples were treated with RNAse A. Modified after Schmidt et al. (2018)[204]. Sequences for *H19* sense and antisense oligonucleotides for RNA-immunoprecipitation are provided in **Table 3**.

Whole Cell Lysis buffer
10 mM Tris pH 7,5
150 mM NaCl
0,15% NP-40

1mM DTT, protease inhibitors and RNAse inhibitor was added freshly.

Sucrose buffer
10 mM Tris pH 7,5
150 mM NaCl
24% sucrose

1mM DTT, protease inhibitors and RNAse inhibitor was added freshly.

Nuclear Lysis Buffer
10 mM Hepes pH 7,6
7,5 mM $MgCl_2$
0,2 mM EDTA
0,3 M NaCl
1 M Urea
1% NP-40

1 mM DTT was added freshly.

Table 3: List of biotinylated-oligonucleotide sequences.

Description	Sequence (5'-3')	Type
#probe 1 sense 90	GAAGCAGTTCCATCATAAAGTG[BtnTg]	Biotinylated H19 sense OGN (sense H19 pulldown Control)
#probe 2 sense 225	CGTATGAATGTATACAGCGAGT[BtnTg]	Biotinylated H19 sense OGN (sense H19 pulldown Control)
#probe 3 sense 551	ACAGATGGTGTCAACATTTTGA[BtnTg]	Biotinylated H19 sense OGN (sense H19 pulldown Control)
#probe 4 sense 714	CTTGAACCCTCAAGATGAAAGA[BtnTg]	Biotinylated H19 sense OGN (sense H19 pulldown Control)
#probe 5 sense 894	GTGTGGTCAATGTGACAGAAAG[BtnTg]	Biotinylated H19 sense OGN (sense H19 pulldown Control)
#probe 6 sense 1186	ATGACAGACAGAACATTTCCAG[BtnTg]	Biotinylated H19 sense OGN (sense H19 pulldown Control)
#probe 4 antisense 1497	AGTGTTAGCTCTTTGGGAAAAG[BtnTg]	Biotinylated H19 antisense OGN (antisense H19 pulldown)
#probe 5 antisense 1623	GATTCAGAACGAGACGGACTTA[BtnTg]	Biotinylated H19 antisense OGN (antisense H19 pulldown)
#probe 6 antisense 1726	AGTCTGCTCTTTCAAAATGTTG[BtnTg]	Biotinylated H19 antisense OGN (antisense H19 pulldown)
#probe 8 antisense 2201	AAAGGATGAAGTAGGGCATGTT[BtnTg]	Biotinylated H19 antisense OGN (antisense H19 pulldown)

#probe 11 antisense 1953	GGTAAATGGGGAAACAGAGTCA[BtnTg]	Biotinylated H19 antisense OGN (antisense H19 pulldown)
#probe 12 antisense 2061	ATTGCCAAAGAGGTTTACACAC[BtnTg]	Biotinylated H19 antisense OGN (antisense H19 pulldown)

2.8.2 Sample preparation for mass spectrometry (MS)

DTT was added to yield a final concentration of 5 mM and the samples were incubated at 55 °C for 30 min. Next, the samples were cooled down to RTemp and Chloroacetamide (CAA) was added at a final concentrations of 40 mM for an incubation period of 30 min in the dark. The CECAD proteomics facility carried out the protein digestion by using the Single-Pot Solid-Phase-enhanced Sample Preparation technology. In brief, 2 µL of a 10 mg/mL mixture of hydrophilic and hydrophobic carboxylate coated paramagnetic beads (SeraMag Speed Beads, Cat No. 44152105050250 and 24152105050250, GE Healthcare) were added to each sample. Acidified acetonitrile was added to achieve a final concentration of 50% organic solvent. Bound proteins were washed with 70% ethanol and 100% acetonitrile. The beads were resuspended in 5 µL 50 mM Triethylammoniumbicarbonate buffer containing 0.1 µg Trypsin (Sigma) and 0.1 µg LysC (Wako). Digestion was carried out for 16 h at 37 °C in a thermocycler to maintain constant temperatures. Recovered peptides were resuspended in 1% formic acid / 5% DMSO and stored at -20° C prior to MS analysis. Modified after Schmidt et al. (2018)[204].

2.8.3 MS

Mass spectrometry was performed at the proteomics facility of the CECAD research center. The samples were analysed on a Q-Exactive Plus (Thermo Scientific) mass spectrometer, coupled to an EASY nLC 1000 UPLC (Thermo Scientific). Peptides were loaded with solvent A (0.1% formic acid in water) onto an analytical column, packed in-house (50 cm × 75 µm I.D., filled with 2.7 µm Poroshell EC120 C18, Agilent). Peptides were chromatographically separated at a constant flow rate of 250 nL/min using the following gradient: 5-30% solvent B (0. 1% formic acid in 80% acetonitrile) within 119 min, 30-50% solvent B within 19 min, followed by washing and column equilibration. The mass spectrometer was operated in data-dependent acquisition mode. The MS1 survey scan was acquired from 300-1750 m/z at a resolution of 70,000. The top ten most abundant peptides were isolated within a 2 Da window and subjected to HCD

fragmentation at a normalized collision energy of 27%. The AGC target was set to $5x10^5$ charges, allowing a maximum injection time of 55 ms. Product ions were detected in the Orbitrap at a resolution of 17,500. Precursors were dynamically excluded for 20 s. Modified after Schmidt et al. (2018)[204].

2.8.4 Bioinformatic analysis of MS data

Bioinformatic analysis of MS data was performed by the proteomics facility at the CECAD research center. The mass spectrometric raw data were processed with Maxquant (version 1.5.3.8) using default parameters. The acquired MS2 spectra were searched against the Uniprot MOUSE.fasta database which included a list of common contaminants. False discovery rates on protein and PSM level were estimated by the target-decoy approach to 0.01% (Protein FDR) and 0.01% (PSM FDR). Minimal peptide length was set to 7 amino acids and carbamidomethyolation at cysteine residues was considered as a fixed modification. Oxidation (M) and Acetyl (Protein N-term) were included as variable modifications. The match-between-runs option was enabled. LFQ quantification was enabled using default settings. The Maxquant output was processed as follows: protein groups flagged as 'reverse', 'potential contaminant', or 'only identified by site' were removed from the proteinGroups.txt. The resulting table was analysed using R through which the protein groups with at least two valid values out of three replicates (or 2 out of 2) in at least one of the bait subgroups were directed to statistical analysis. The R 'STATS' Package was used to perform Student's t-tests to distinguish significantly changed proteins. Those peptides with p-values < 0.05 and log2 fold-changes > 1 were considered as significantly different. Proteins that provide 2 or 3 valid values in one bait group and zero in the other, were also considered as significantly different. Modified after Schmidt et al. (2018)[204].

2.8.5 Ingenuity pathway analysis and AMIGO2 GO Term Analysis

By using ChART-MS, 3,590 proteins were detected in total. All 168 uniquely identified and significantly enriched peptides with fold-changes ≥1.5 between *H19* antisense compared to sense oligonucleotide immunoprecipitation in confluent (n=114) or differentiated (n=102) conditions were analysed using the Ingenuity Pathway Analysis (IPA). To construct a functionally interconnected *H19* protein interactome, all n=168 genes were loaded into IPA and gene nodes with ≥1 edges to other genes retained. For

GO Term classification of the remaining n=61 *H19* interaction partners, corresponding Gene Symbols were loaded into AMIGO2 (http://amigo.geneontology.org) and those proteins counted classified by GO Terms 'RNA binding' or 'Chromatin binding' or 'Chromatin modification'. Modified after Schmidt et al. (2018)[204].

2.9 Mouse procedures

2.9.1 Animal care and research diets

All animals were maintained on a C57BL/6 N background, housed in individually ventilated cages (IVC Type II long) in groups of 3-5 animals per cage on a constant 12 h light/dark cycle at a temperature of 22-24°C with relative air moisture (50-70%) in a SPF controlled facility with regular testing for pathogens. All experimental mice were 17-18 weeks of age at sacrifice. Experimental mice were exposed to HFD feeding for 15 weeks (H19 TG and $H19^{\Delta AT}$ mice versus littermate Controls) and 17-18 weeks of age at sacrifice. The care of animals was within institutional and animal-care committee guidelines approved by local government (Bezirksregierung Köln) and regional authorities (Tierschutzkommission acc. §15 TSchG of the Landesamt for Natur, Umwelt and Verbraucherschutz (LANUV) North-Rhine Westphalia, Germany, internal reference no. 84-02.04.2014.A068). Unless otherwise indicated, animals were allowed *ad libitum* access to food and drinking water.

For maintenance animals received a normal chow diet (NCD) containing 57% carbohydrate, 34% protein and 9% fat. For diet-induced obesity (DIO) experiments, mice were fed a high-fat diet (HFD) containing 54% fat, 24% protein and 22% carbohydrate, starting at 3 weeks of age. Control animals were fed a Control diet (CD) containing 62 % carbohydrate, 20% protein and 13% fat starting at 3 weeks of age. Modified after Schmidt et al. (2018)[204].

NCD:	ssniff® R/M-H Low-Phytoestrogen	(Product-ID: V1554)
HFD:	ssniff® EF acc. D12492 (I) mod.	(Product-ID: E15742)
CD:	ssniff® EF D12450B* mod. LS	(Product-ID: E15748)

All diets were purchased from ssniff Spezialdiäten GmbH, Soest, DE.

2.9.2 Experimental mouse models

Specific AT reduction of *H19* expression was achieved via Cre recombinase-mediated excision of LoxP-flanked ('floxed') gene sequences. Mice harbouring loxP-flanked *H19* differentially methylated regions (DMR; H19-DMR$^{flDMR/flDMR}$) were obtained from the group of Linheng Li (Stowers Institute) and generated as described[209] and. Female H19-DMR$^{flDMR/flDMR}$ mice were bred with male C57BL76 mice expressing adipose-selective Adiponectin (*Adipoq*)-promoter driven Cre (H19-DMR$^{wt/wt}$;Adipoq-Cre$^{tg/wt}$) to obtain H19-DMR$^{flDMR/wt;}$Adipoq-Cre$^{tg/wt}$ (H19$^{\Delta AT}$) and H19-DMR$^{flDMR/wt}$;Adipoq-Cre$^{wt/wt}$ as control littermates (control for H19$^{\Delta AT}$). *Adipoq-Cre* mice were originally purchased from Jackson Laboratory (Bar Harbor, ME, USA; stock number 010803-JAK) and maintained in-house. The Cre recombinase is expressed heterozygously under control of the fat-specific *Adipoq* promotor in these transgenic mice. For *H19* overexpression, a strain harbouring yeast artificial chromosomes (YACs, present in ten genomic copies) was used. Each YAC cassette contained a 130 kb transgene spanning the entire *H19-Igf2* cluster in which the Igf2 coding sequence was inactivated with the lacZ reporter gene (MGI accession number 5648556, Symbol: Tg(Igf2/LacZ,H19)YZ15Aco; H19 TG)[210]. Only male, non-randomized mice were used for the experiments and the non-transgenic littermates were used as experimental controls.

Tissues from C57BL/6 N mice exposed to 4°C either for 1 or 7 days were kindly provided by the laboratory of Prof. Dr. Jörg Heeren, Institute for Biochemistry and Molecular Cell Biology, Medical Center Hamburg-Eppendorf, Hamburg, Germany. All other experiments were performed using C57BL/6 N mice. Modified after Schmidt et al. (2018)[204].

2.9.3 Genotyping

2.9.3.1 Genomic DNA extraction from mouse tails

Mouse tail biopsies were obtained at weaning age and incubated in 500 µL tail lysis buffer by shaking overnight at 56 °C and 400 rpm.

2.9.3.2 Polymerase chain reaction (PCR)

For genotyping genomic DNA was tested for H19lxDMD, LacZ, and *Adipoq-cre* gene presence. In brief, 2 µl of extracted genomic DNA (gDNA) were mixed with 23 µl of corresponding PCR master mix (**Table 4**) and polymerase chain reaction (PCR) was performed using primers listed in **Table 5**. PCR master mix consisted of approximately 25pMol of each primer, 25 µM dNTP mix, 1% Dream Taq Green Buffer, and 1 unit Dream Taq DNA polymerase per 25 µl reaction. PCR cycling parameters have been determined for each individual PCR according to the annealing temperature of the specific primer pair and the length of the DNA product.

Table 4: Composition of PCR master mix.

Reagent	H19lxDMD	LacZ	*AdipoQ-Cre*
Dream Taq Green Buffer (10x)	2.5 µl	2.5 µl	2.5 µl
dNTPs (10mM)	0,4 µl	0,4 µl	0,5 µl
Primer (10 µM)	22745 0,4 µl 22746 0,4 µl	ARTE_βGAL3 0,4 µl ARTE_βGAL4 0,4 µl	mom0137 0,2µl mom0138 0,2µl oIMR6694 0,4µl oIMR6695 0,4µl
Millipore H_20	19,1 µl	19,5 µl	20,4 µl
Dream Taq Green DNA Polymerase	0,2 µl	0,2 µl	0,4 µl

All PCRs were performed using FlexCycler² PCR-Thermocycler using the following programs:

<u>*AdipoQ-cre*</u>

Temperature [°C]	Time [m:s]	
94	3:00	
94	0:30	
60	1:00	33x
72	1:00	
72	2:00	
12	∞	

H19-flox

Temperature [°C]	Time [m:s]	
95	5:00	
95	0:30	
56,3	0:30	34x
72	1:00	
72	10:00	
12	∞	

LacZ

Temperature [°C]	Time [m:s]	
94	5:00	
94	0:30	
60	0:30	26x
72	0:30	
72	5:00	
14	∞	

2.9.3.3 Agarose gel electrophoresis

Amplified DNA fragments were separated by native gel electrophoresis. For the preparation of the gel, 3g of agarose was dissolved in 100ml 1x TAE buffer, boiled and poured, resulting in gels of 3% containing 5% Midori Green Advance DNA stain® (Nippon Genetics Europe) for DNA visualization. DNA fragments were separated at 140V by a Gene power supply GPS 200/400 (Pharmacia, Uppsala, SWE) and visualized under UV light on a FastGene® FAS V gel documentation system.

50x TAE buffer

50 mM	EDTA disodium salt
2 M	Tris
1M	glacial/acetic acid

Expected products sizes are indicated below:

Products for *AdipoQ-cre*:

WT:	542 bp
Tg:	450 bp

Products for YZ15:

Tg:	315 bp

Products for H19-flox:
WT: 300 bp
WT/flox: 300 bp and ~350 bp
Flox/flox: ~350 bp

Table 5: List of primers for genotyping PCR.

PCR	Name	Sequence (5'-3')
AdipoQ-cre	mom0137	CTGCAGTTCGATCACTGGAAC
	mom0138	AAAGGCCTCTACAGTCTATAG
	oIMR6694	TCCAATTTACTGACCGTACA
	oIMR6695	TCCTGGCAGCGATCGCTATT
H19-flox	22745	GGCAACCCTGGTCTTTACAC
	22746	GCCCTATTCTTGGACGTCTG
YZ15	ARTE_βGAL3	ATCCTCTGCATGGTCAGGTC
	ARTE_βGAL3	CGTGGCCTGATTCATTCC

2.9.4 Phenotyping

2.9.4.1 Assessment of body weight

Body weight of HFD- and CD-fed H19 TG and H19$^{\Delta AT}$ and Control mice was assessed weekly for each individual mouse for ages 3-18 weeks.

2.9.4.2 Glucose tolerance test (GTT)

The GTT was performed at 13 weeks of age, prior to which the mice were exposed to CD or HFD feeding for 10 weeks. After a 6 h fasting period, the GTT was carried out at 12 noon. The basal blood glucose levels (0 min) were measured and subsequently, the animals received an intraperitoneal bolus of 2 g glucose per kilogram of body weight (20% glucose, Delta select). An automated glucose monitor was used to record blood glucose values at 15, 30, 60 and 120 min after injection. Modified after Schmidt et al. (2018)[204].

2.9.4.3 Insulin tolerance test (ITT)

The ITT was performed when mice were 12 weeks of age after 9 weeks of exposure to either CD or HFD feeding. The ITT was carried out in random-fed state between 9-10am in fresh cages with bedding, free access to drinking water but no food. After determining basal blood glucose levels (0 min) using a glucometer, each animal received 0,75 U/kg of body weight of insulin (Actrapid; Novo Nordisk) via intraperitoneal administration.

Blood glucose levels were measured 15, 30 and 60 min after injection. Modified after Schmidt et al. (2018)[204].

2.9.4.4 Indirect calorimetry (PhenoMaster)

For indirect calorimetry measurements, mice of all genotypes and diets were 16 weeks of age and had been exposed to either HFD or CD for 13 weeks. To obtain metabolic measurements, the PhenoMaster System (TSE) was used. Five days before the experiment, mice were single-housed in trainings cages, identical to the 7.1-1 chambers of the PhenoMaster open circuit calorimetry system. The mice received their respective diets (HFD, CD) throughout the training and data acquisition periods with *ad libitum* access to food and water. Food intake was measured using the built-in automated system. Initially, parameters of indirect calorimetry were measured for 96h at 22°C (warm measurement). Subsequently, temperatures within the PhenoMaster setup were reduced to 4°C (cold measurement) and data acquired for 96 h. Afterwards, norepinephrine (NE) was administered intraperitoneally at a final concentration of 1 mg/kg and systematic data collection continued for another 24 h (NE measurement) at 4°C to measure maximally activated BAT uncoupling effects. Mean values for every measurement, each time of day, were calculated and plotted for warm, cold and NE measurement. Modified after Schmidt et al. (2018)[204].

2.9.5 Serum analyses

Serum analyses were performed by the Institute for clinical chemistry at the University Clinics in Cologne. Serum was obtained by allowing the blood to clot at 4°C for 4 h, followed by a centrifugation step of 10 min at 6,200 g. The supernatants were transferred to a new tube and centrifuged for another 10 min at 17,000 g. The serum was collected and stored at -80 °C diluted 1:3 with 0.9% NaCl. To analyse serum cholesterol levels, the Cholesterin CHOD-PAP (Roche Diagnostics) was used. Similarly, to determine triglycerides levels, the Triglyceride GPO-PAP of Roche Diagnostics was used. Both analyses ran on the Cobas C 702 (Roche Diagnostics). Modified after Schmidt et al. (2018)[204].

2.10 Graphical representation of data and statistical analysis

All graphs were created using GraphPad Prism 7.0. Floating bars indicate minimum, maximum and mean values. GraphPad Prism 7.0 software was utilized to perform statistical calculations. When two groups were analysed, significance was determined using an unpaired or paired Student´s t-test. When three groups were analysed, a one-way ANOVA followed by Bonferroni correction was used. Two-way ANOVA was applied for repeated measures (2WA-RM) followed by Bonferroni post-hoc test to judge the effect of two independent variables. Statistical details are provided in the figure legends. A p value < 0.05 is considered statistically significant.

Significance was indicated as followed in the figures:

n.s.	$p > 0.05$
*	$p < 0.05$
**	$p < 0.01$
***	$p < 0.001$
****	$p < 0.0001$

3 Results

3.1 Brown adipose tissue (BAT)-regulatory lncRNAs correlate with BAT function

In order to identify mRNAs and lncRNAs correlating with BAT function, lean male C57BL/6 N mice were either exposed to thermal stress (4°C, as model for BAT activation) for 24 h compared to mice housed by ambient temperatures (22°C) or to chronic HFD (as model for BAT dysfunction) compared to CD feeding. Afterwards, RNA-Seq was performed with RNA from BAT samples of these mice. Additionally, RNA-Seq with RNA from BAT, scWAT, and vWAT from C57BL/6 N male mice housed at ambient temperatures and fed a NCD was conducted to analyse the function of candidate genes throughout all ATs. Different filter criteria were applied to identify candidates for further characterization. As criteria we selected adipose enrichment, size of noncoding RNAs (>200nt), and increased expression (FPKM > 1). Across cold/DIO conditions, 1394/433 mRNAs were upregulated and 1147/429 mRNAs were downregulated whereas 71/6 lncRNAs were upregulated and 101/33 lncRNAs were downregulated (fold-change ≥ 2 or ≤-2) (Figure 4). After manual verification of the RNA-Seq data, four candidates were selected for further studies: *170007L15Rik*, *2500002B13Rik*, *Gm12319*, and *H19*. With this screen, we could show that BAT-regulatory lncRNAs correlate with BAT function *in vivo*.

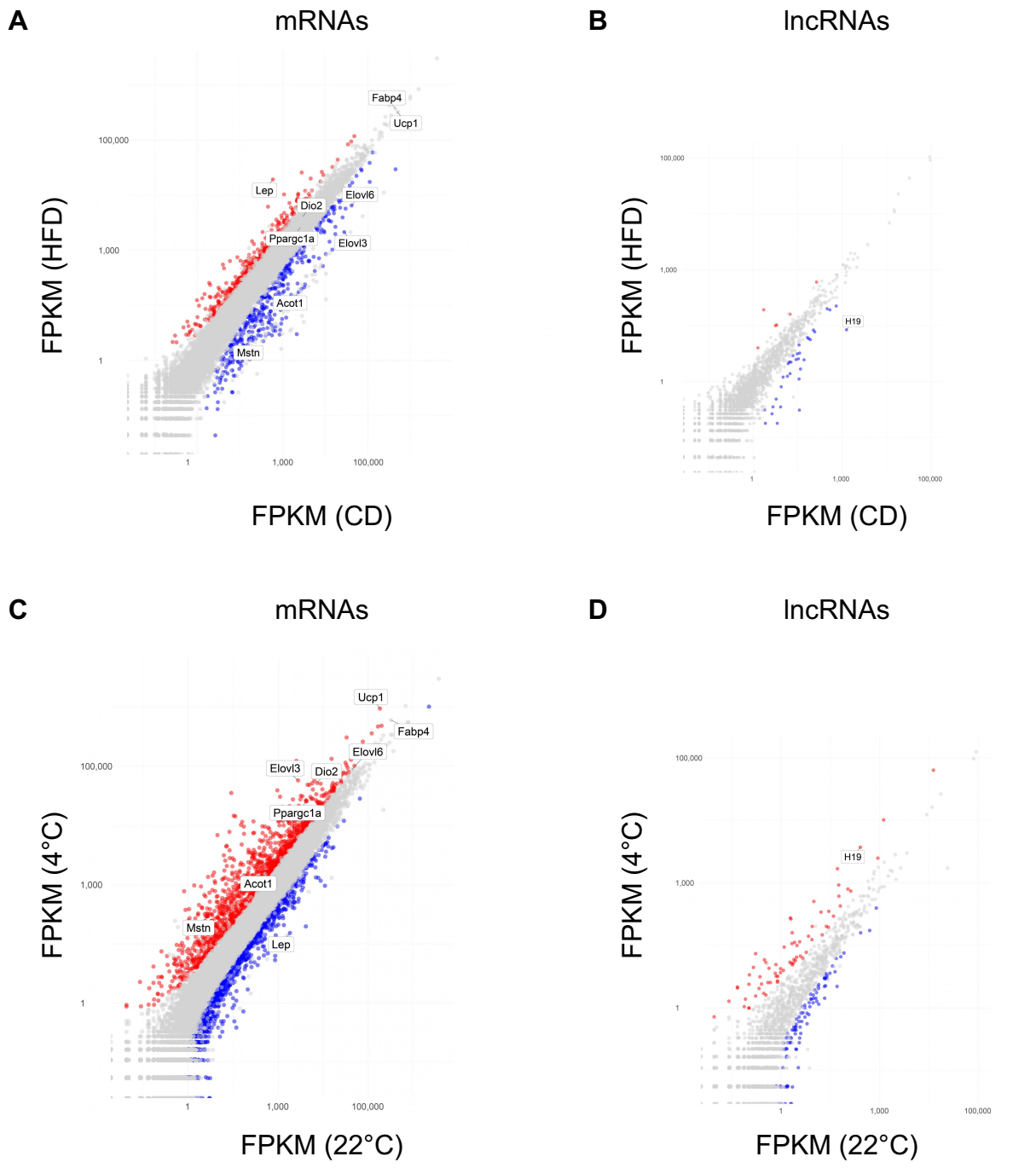

Figure 4: RNA-Seq reveals lncRNAs correlating with BAT function *in vivo*
(A, B) Graph of BAT (A) mRNA or (B) lncRNA expression after chronic (24 weeks) HFD versus CD feeding in male C57BL/6 N mice as obtained by RNA-Seq (n=2 per biological condition). (C, D) Graph of BAT (C) mRNA or (D) lncRNA expression 24 h after exposure to 4°C or 22°C in male C57BL/6 N male mice as obtained by RNA-Seq (n=2 per biological condition). Modified after Schmidt et al. (2018)[204]. Graphs were generated with the help of P. Klemm.

For the verification of the RNA-Seq results, qRT-PCR analysis was performed with an independent set of samples (Figure 5). The analysis of an AT profile showed that BAT associated marker genes (such as *ELOVL Fatty Acid Elongase 3* (*Elovl3*), *Uncoupling Protein 1* (*Ucp1*)) as well as candidate lncRNAs (*1700007Rik15*, *250002B13Rik*, *Gm12319* and *H19)* were mainly expressed in BAT compared to scWAT and vWAT (Figure 5A, B). Moreover, the RNA-Seq results were confirmed by increased and decreased *Ucp1* and *Elovl3* mRNA expression during cold or DIO, respectively (Figure 5C, E). Because of their BAT-selective expression, we focussed on lncRNAs *1700007Rik15*, *250002B13Rik*, *Gm12319,* and *H19*. These lncRNAs revealed the same pattern of expression as *Elovl3* and *Ucp1* upon cold and DIO conditions in BAT (Figure 5D, F). To reveal the expression of the candidate lncRNAs and the browning/'beiging' marker *Ucp1* upon cold exposure and DIO in other ATs, we performed qRT-PCR in scWAT and vWAT (Figure 5G-N). In scWAT the browning/'beiging' marker *Ucp1* was increased upon cold exposure and decreased in DIO. *H19* showed an opposite pattern in expression during both conditions. The three lncRNAs *1700007Rik15*, *250002B13Rik*, *Gm12319* were not altered upon cold conditions whereas upon DIO they were decreased except from *Gm12319* which did not show a difference in expression. In vWAT, *1700007Rik15*, *250002B13Rik*, and *H19* did not show differences in expression whereas *Gm12319* was significantly decreased and *Ucp1* showed a tendency to be decreased upon cold exposure. Upon HFD conditions *H19* and *Ucp1* were both significantly increased whereas *1700007Rik15* was decreased. The expression of *Gm12319* and *250002B13Rik* was not altered upon DIO.

These results show that the verification of RNA-Seq had been successful and that the candidate lncRNAs were mainly enriched in BAT and reveal a similar expression pattern as BAT-associated mRNAs.

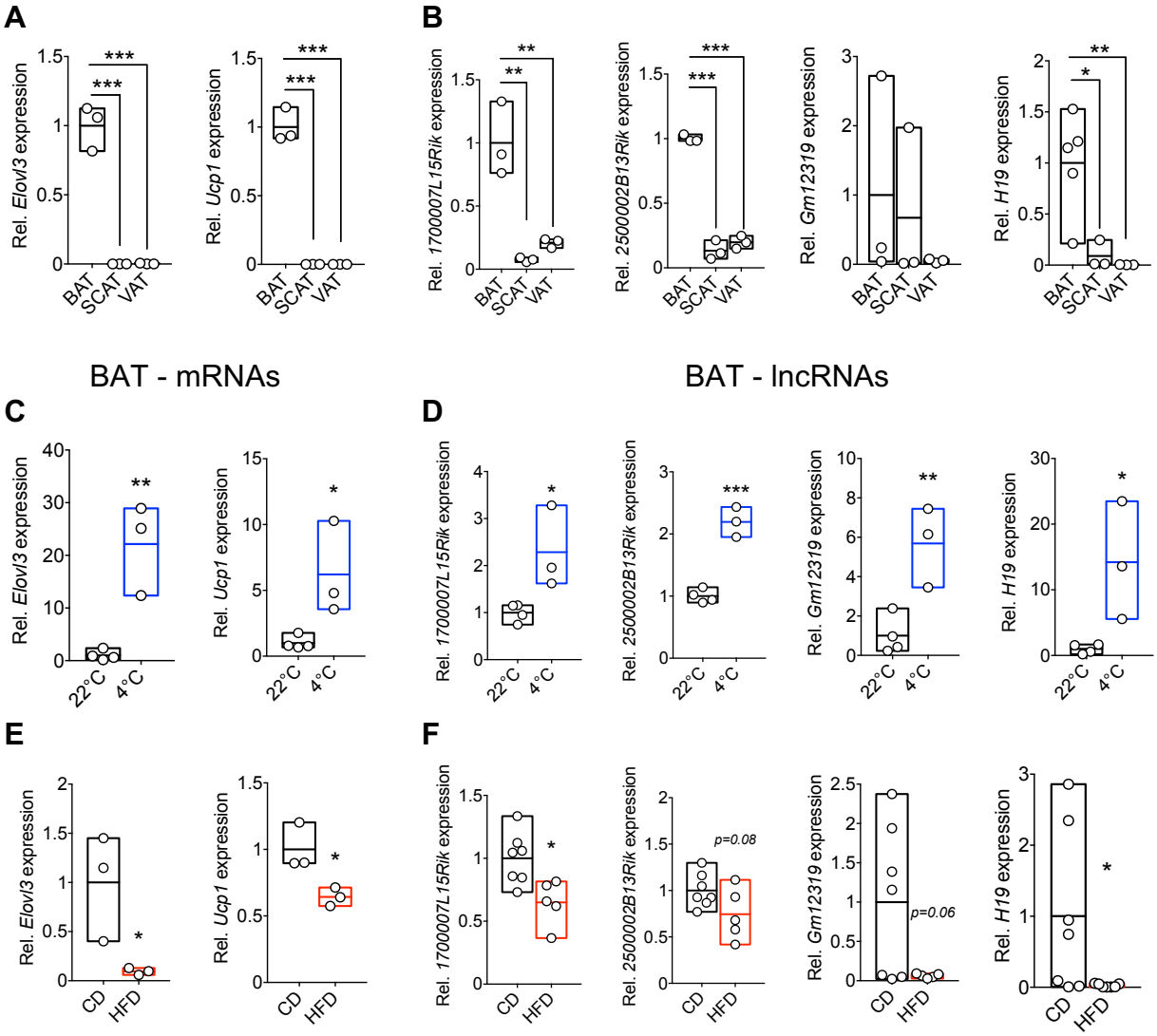

Figure 5: BAT-specific candidate lncRNAs reveal similar expression pattern as BAT-associated mRNAs

Relative BAT, scWAT and vWAT expression of (A) *Elovl3* (n=3) and *Ucp1* (n=3) and (B) *1700007Rik15* (n=3), *2500002B13Rik* (n=3), *Gm12319* (n=3), and *H19* (n=5 for BAT, n=3 for scWAT and vWAT) in lean C57BL/6 N male mice as quantified per qRT-PCR analysis. Relative (C-F) BAT expression of *Elovl3*, *Ucp1*, *1700007Rik15*, *2500002B13Rik*, *Gm12319*, and *H19* in lean C57BL/6 N male mice housed at 22°C (n=4) versus 24h of 4°C (n=3) and C57BL/6 N male mice exposed to chronic HFD (n=3 for *Elovl3* and *Ucp1*, n=5 for *1700007Rik15*, *2500002B13Rik*, *Gm12319*, and *H19)* versus CD (n=3 for *Elovl3* and *Ucp1*, n=7 for *1700007Rik15*, *2500002B13Rik*, *Gm12319*, and *H19)* feeding as quantified by qRT-PCR analysis. Relative (G-J) scWAT expression of *Elovl3*, *Ucp1*, *1700007Rik15*, *2500002B13Rik*, *Gm12319*, and *H19* in lean C57BL/6 N male mice housed at 22°C (n=2 for *Ucp1*, n=4 for *1700007Rik15*, *2500002B13Rik*, *Gm12319*, and *H19*) versus 24h of 4°C (n=2 for *Ucp1*, n=4 for *1700007Rik15*, *2500002B13Rik*, *Gm12319*, and *H19*) and C57BL/6 N male mice exposed to chronic HFD (n=4) versus CD (n=3 for *Ucp1*, n=4 for *1700007Rik15*, *2500002B13Rik*, *Gm12319*, and *H19*) feeding as quantified by qRT-PCR analysis. Relative (K-N) vWAT expression of *Elovl3*, *Ucp1*, *1700007Rik15*, *2500002B13Rik*, *Gm12319*, and *H19* in lean C57BL/6 N male mice housed at 22°C (n=2 for *Ucp1*, n=4 for *1700007Rik15*, *2500002B13Rik*, *Gm12319*, and *H19*) versus 24h of 4°C (n=2 for *Ucp1*, n=4 for *1700007Rik15*, *2500002B13Rik*, *Gm12319*, and *H19*) and C57BL/6 N male mice exposed to chronic HFD (n=3 for *Ucp1*, n=4 for *1700007Rik15*, *2500002B13Rik*, *Gm12319*, and *H19*) versus CD (n=4) feeding as quantified by qRT-PCR analysis. Transcript levels of mRNAs were normalized to *hypoxanthine phosphoribosyltransferase 1* (*Hprt1*) expression. Graphs show floating bars with the line at the mean with all data points plotted; and unpaired two-tailed Student´s t-tests were used to assess statistical significance. *p<0,05, **p<0,01, ***p<0,001. If applicable, p-values are indicated within the panel. blue = 4°C, red = high-fat diet (HFD). Modified after Schmidt et al. (2018)[204]. Figure continued on the next page.

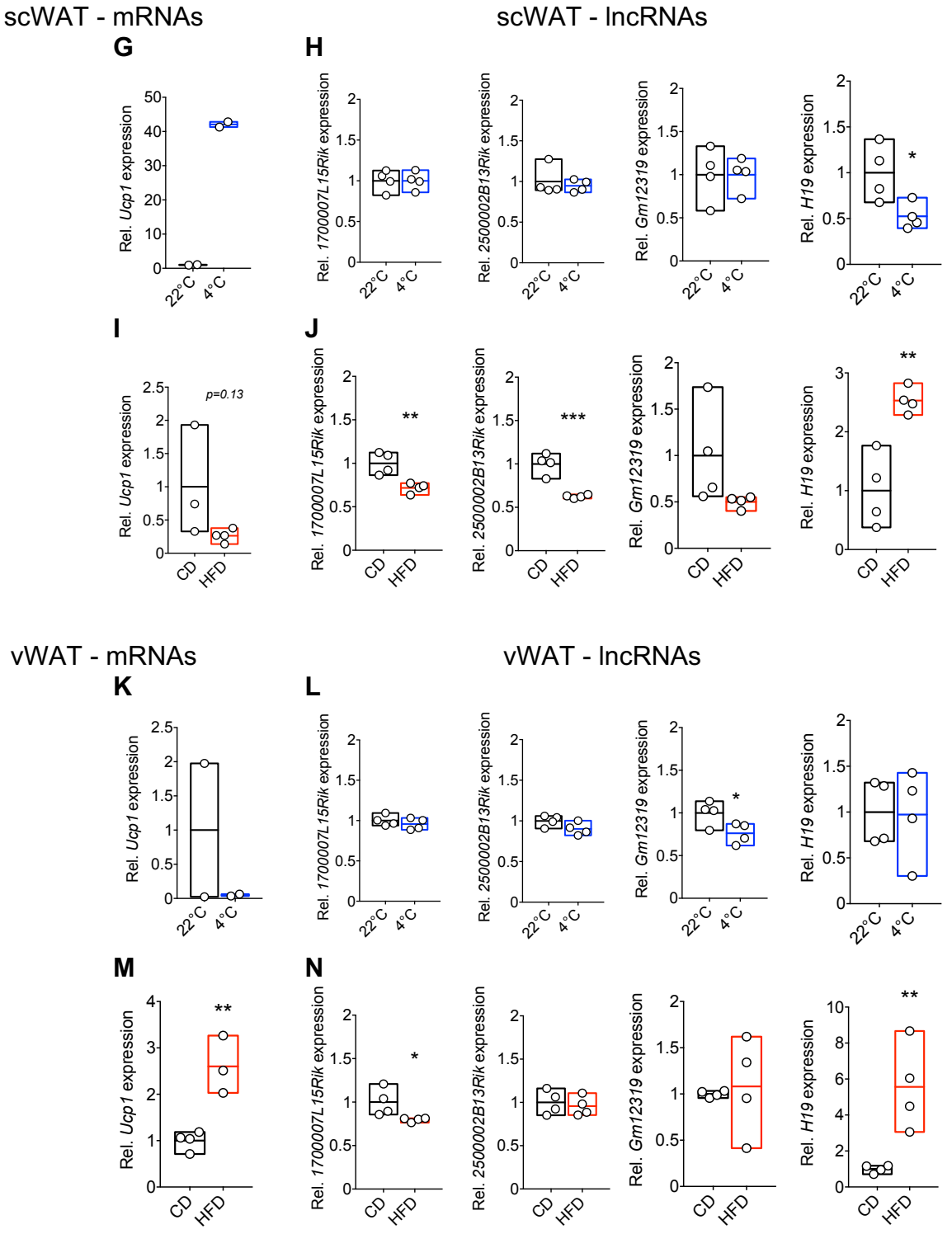
scWAT - mRNAs
scWAT - lncRNAs
G
H
Rel. Ucp1 expression
Rel. 1700007L15Rik expression
Rel. 2500002B13Rik expression
Rel. Gm12319 expression
Rel. H19 expression
22°C
4°C
I
J
p=0.13
CD
HFD
vWAT - mRNAs
vWAT - lncRNAs
K
L
M
N

3.2 LncRNA candidates *2500002B13Rik* and *H19* control brown adipogenesis

To analyse whether the knockdown of the candidate lncRNAs leads to defects in AT differentiation, we performed locked nucleic acid (LNA)-mediated RNA interference (RNAi) in SVF adipocyte precursor cells. Generally, LNA GapmeRs are used for loss-of-function studies of proteins, mRNAs, and lncRNAs. These single stranded antisense oligonucleotides function through catalysis of RNase H-dependent degradation of complementary RNA targets.

For analysis, SVF cells were isolated from three major adipose depots BAT, scWAT, and vWAT. The experiment revealed blunted lipid accumulation upon RNAi of *2500002B13Rik* and *H19* in primary brown adipocyte precursor cells whereas lipid accumulation upon RNAi of *1700007L15Rik* and *Gm12319* in 1° BAT was not affected (Figure 6A). 1° scWAT and 1° vWAT did not show differences in lipid accumulation upon RNAi with candidate lncRNAs (Figure 6B, C). The transfection procedure did not affect lipid accrual as scr-transfected cells revealed equal amounts of lipid accumulation as non-transfected cells.

From these results, we conclude that loss of *2500002B13Rik* and *H19* gene expression leads to a defect in BAT, yet not scWAT or vWAT differentiation.

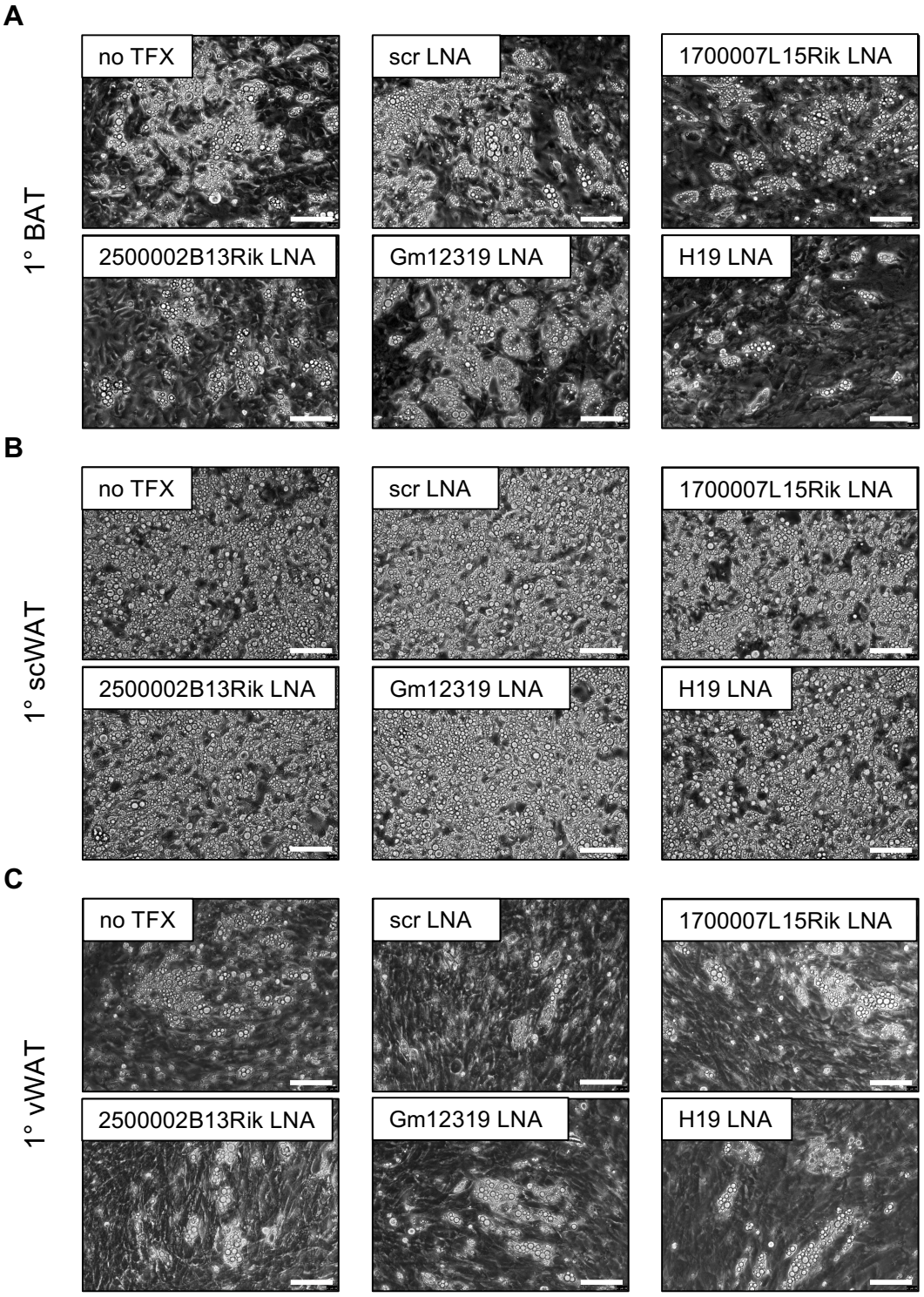

Figure 6: Loss of *2500002B13Rik* and *H19* results in a decrease of lipid accrual
Photomicrograph of (A) BAT, (B) scWAT, and (C) vWAT derived 1° adipocytes after no transfection (no TFX), transfection with 25 nM scrambled (scr), *1700007L15Rik, 2500002B13Rik, Gm12319* or *H19* LNAs. Pictures are representative of n=6 (1° BAT) or n=3 (1° scWAT and 1° vWAT) independent experiments, performed in n=3 technical replicates each. Scale bar = 100 µm. Modified after Schmidt et al. (2018)[204].

Next, we tested which effect RNAi of the candidate genes has on gene expression of browning/'beiging' or common AT markers in 1° SVF adipocyte precursor cells isolated from BAT, scWAT, and vWAT. RNAi of *1700007L15Rik* did not result in changes in adipogenesis markers in all three adipose tissues except from the common AT marker *Peroxisome Proliferator Activated Receptor Gamma* (*Pparγ*) which was significantly decreased in scWAT (Figure 7A). RNAi of *2500002B13Rik* did not show differences in gene expression in scWAT or vWAT whereas BAT markers like *Cell Death-Inducing DFFA-Like Effector A* (*Cidea*) and *Ucp1* were significantly decreased in BAT. Moreover, *CCAAT/Enhancer Binding Protein Alpha* (*Cebpa*), *Iodothyronine Deiodinase 2* (*Dio2*), and *Fatty Acid Binding Protein 4* (*Fabp4*) showed a tendency to be decreased (Figure 7B). RNAi of *Gm12319* resulted in no difference of gene expression in all three AT (Figure 7C). RNAi of *H19* led to a significant decrease of BAT markers such as *Cidea* and *Ucp1* along with *Elovl3* which showed a tendency to be decreased in 1° BAT. In scWAT RNAi of *H19* resulted in a significant decrease of common adipogenesis markers *Fabp4* and *Pparγ* and BAT-specific marker *PPARG Coactivator 1 Alpha* (*Pgc1α*). In vWAT *Adiponectin* (*AdipoQ*), *Cebpa,* and *Fabp4* showed a tendency to be reduced upon RNAi of *H19* (Figure 7D).

These results show that the knockdown of both *2500002B13Rik* and *H19* leads to a decrease in lipid accumulation (Figure 6) and gene expression of adipogenesis markers (Figure 7) in primary adipocytes of BAT whereas the loss of *Gm12319* and *1700007L15Rik* did not have an effect on adipogenesis. Although *H19* loss also resulted in a decrease of adipogenesis markers in primary scWAT and vWAT, the effect was weaker compared to BAT.

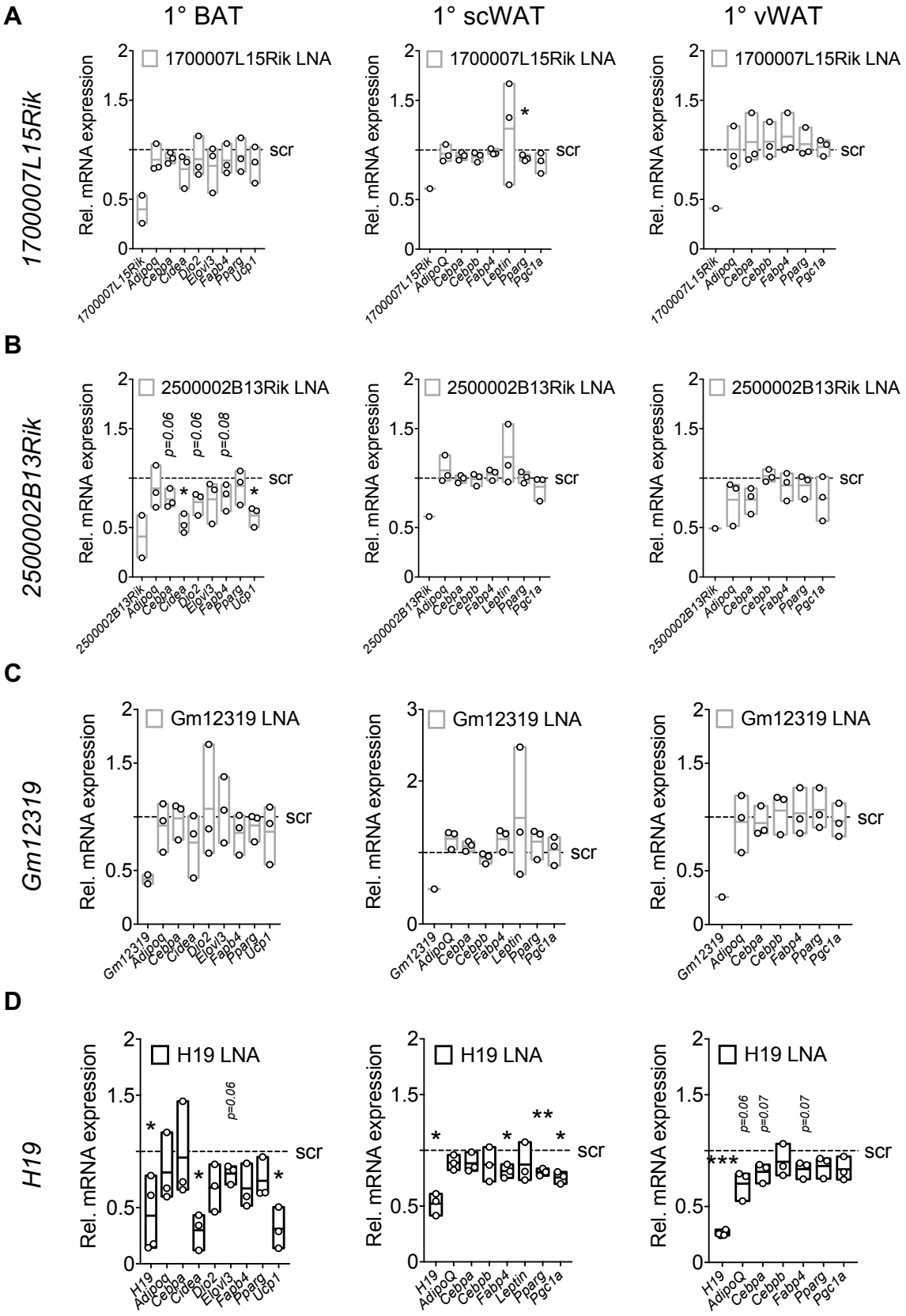

Figure 7: *2500002B13Rik* and *H19* RNAi results in decreased expression of browning markers in 1° BAT

Relative expression of indicated mRNAs in BAT, scWAT, and vWAT derived from 1° adipocytes after transfection with 25 nM scr, (A) *1700007L15Rik* LNAs (n=2 for *1700007L15Rik* in BAT, n=1 for *1700007L15Rik* in scWAT and vWAT, and n=3 for other genes in 1° BAT, scWAT, and vWAT), (B)

2500002B13Rik LNAs (n=2 for *2500002B13Rik* in BAT, n=1 for *2500002B13Rik* in scWAT and vWAT, and n=3 for other genes in 1° BAT, scWAT, and vWAT), (C) *Gm12319* LNAs (n=2 for *Gm12319* in BAT, n=1 for *Gm12319* in scWAT and vWAT, and n=3 for other genes in 1° BAT, scWAT, and vWAT) or (D) *H19* LNAs (n=4 for *H19* in BAT, n=3 for other genes in BAT, scWAT and vWAT). Transcript levels of mRNAs were normalized to *Hprt1* expression. Graphs show floating bars with a line at the mean with all data points plotted. A paired, two-tailed Student´s t-test was used to assess statistical significance across n=3 independent experiments performed in n=3 technical replicates. *p<0,05, **p<0,01, ***p<0,001. If applicable, p-values are indicated within the panel. Modified after Schmidt et al. (2018)[204].

We henceforth only focussed on the lncRNA *H19,* which was induced in cold-exposed and decreased in obese BAT due to its BAT-selective expression, strong sequence conservation among eutherians, and stronger impact on gene expression upon RNAi (compared to *2500002B13Rik*). Notably, *H19* expression was not altered accordingly in scWAT or vWAT depots in contrast to browning/'beiging' markers like *Ucp1*, pointing to a selective involvement of *H19* in brown but not white adipocyte differentiation and function. For further characterisation of the effects of *H19* on adipogenesis, Oil Red O (ORO) staining was performed for quantification of lipid accrual. ORO staining showed that upon RNAi of *H19* significantly less lipid droplets were formed resulting in impaired adipogenesis (Figure 8).

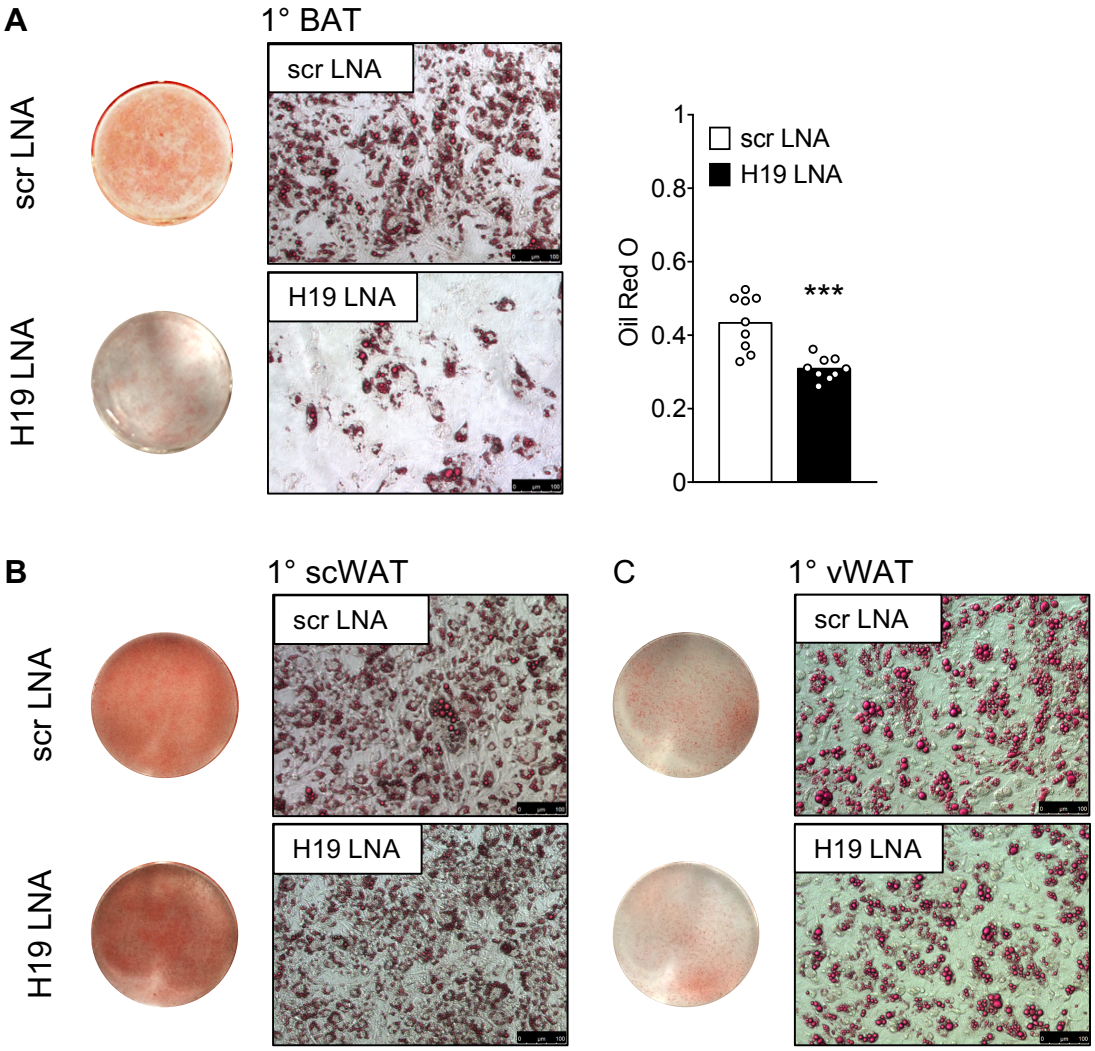

Figure 8: LncRNA *H19* controls brown but not white adipocyte differentiation
Macroscopic view of ORO stained 24-well plates (*left*), photomicrographs of ORO stainings of (A) BAT, (B) scWAT, and (C) vWAT derived 1° adipocytes and densitometric quantification ORO dye incorporation in (A) 1° BAT after transfection with 25nM scr versus H19 LNA. An unpaired, two-tailed Student´s t-test was applied to assess statistical significance across n=3 independent experiments performed in n=3 technical replicates each. ***p<0,001. Scale bar = 100 µm. Modified after Schmidt et al. (2018)[204].

To support the findings of alterations in gene expression in *H19* deficient 1° BAT and the substantial morphological defect seen during brown adipocyte differentiation, we conducted immunoblot analyses and observed a significant reduction of terminal brown adipocyte marker proteins such as UCP1 and PGC1α in *H19*-deficient 1° BAT (Figure 9).

These results show that lncRNA *H19* is required for the commitment of BAT but not scWAT or vWAT-derived progenitors and argue for a selective involvement of the lncRNAs in brown but not 'beige' adipocyte differentiation and function.

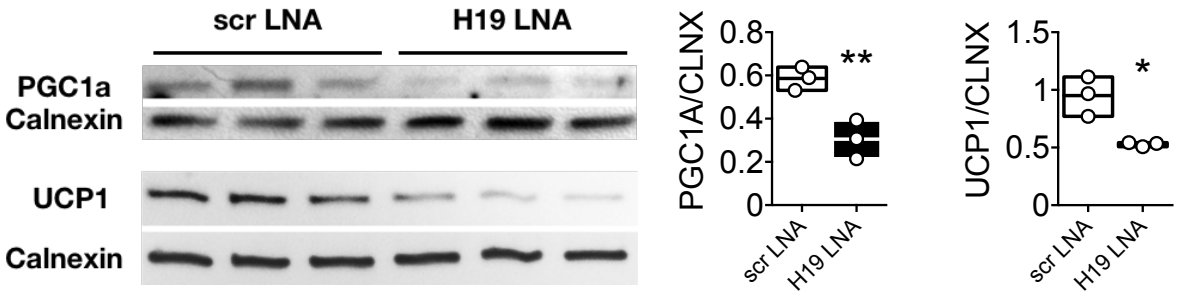

Figure 9: Loss of *H19* results in decreased PGC1α and UCP1 protein expression in 1° BAT
PGC1α and UCP1 immunoblot analysis (*left*) and quantification (*right*) of 1° BAT adipocytes after transfection with 25 nM scr or H19 LNA. Image is representative of three independent experiments. Graphs show floating bars with a line at the mean with all data points plotted. An unpaired, two-tailed Student´s t-test was applied to assess statistical significance across n=3 independent experiments performed in n=3 technical replicates each. *p<0,05, **p<0,01. Modified after Schmidt et al. (2018)[204].

3.3 Second LNA GapmeR (LNA H19_2) confirms *H19* effect on adipogenesis and excludes off-target effects

Although novel technologies like LNA GapmeRs are continuously improved, off-target effects are still a problem which have to be addressed when using these inhibitors. Off-target effects most often arise from partial complementarity of the sense or antisense strand to an unintended gene sequence due to the single sequence of LNA GapmeRs. To exclude off-target effects, we used another LNA GapmeR for *H19* (LNA H19_2) to confirm former results. Knockdown experiments with LNA H19_2 confirmed the results by showing a decrease in the accumulation of lipid droplets as well as a tendency for a decrease in the expression of *Cebpa, Cidea,* and *Ucp1* in 1° BAT whereas no difference in gene expression of adipogenesis genes could be shown in 1° scWAT and 1° vWAT (Figure 10).

These data confirm that the use of two LNA GapmeR inhibitors for *H19* with different sequences leads to the same effects, although RNAi with LNA H19_2 was not as strong as the first inhibitor. Thus, the second inhibitor showed less pronounced effects.

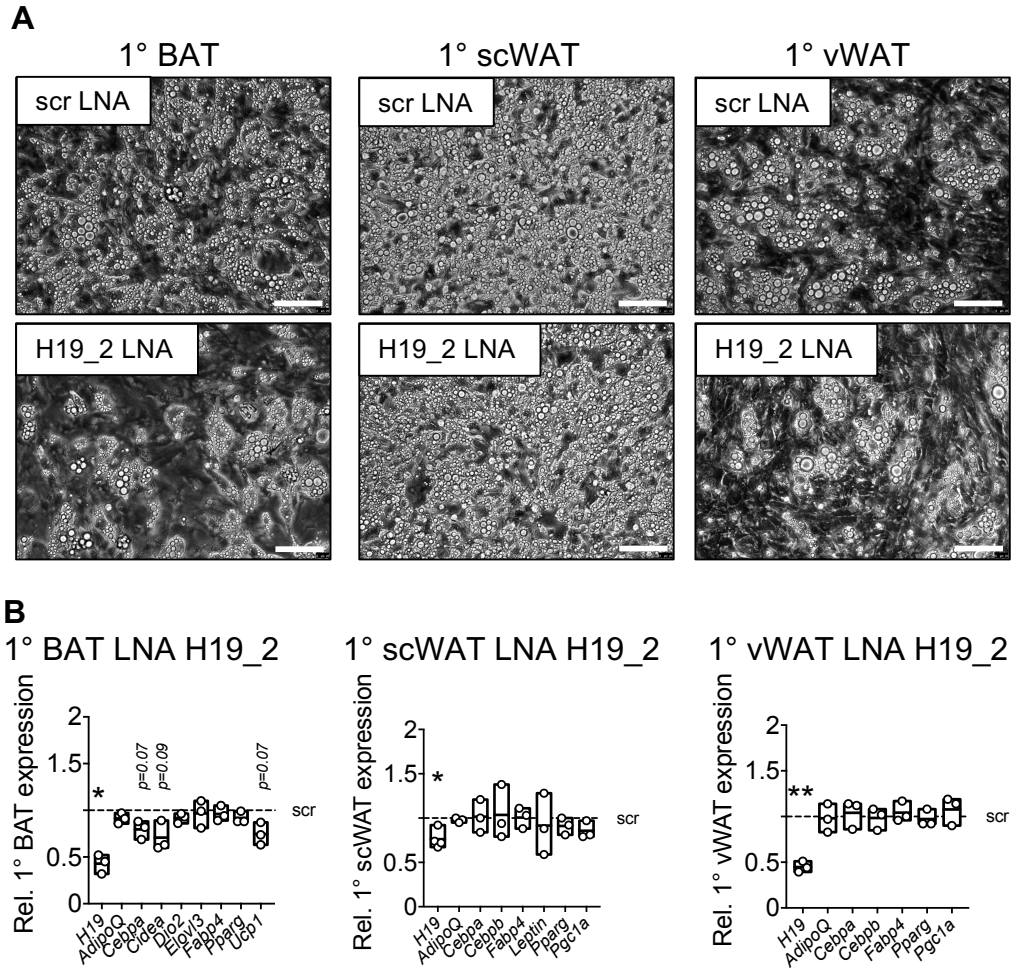

Figure 10: LNA H19_2 confirms *H19* effect on adipogenesis and excludes off-target effects
(A) Photomicrographs and (B) gene expression of the indicated mRNAs in BAT, scWAT, and vWAT derived 1° adipocytes after transfection with 25 nM scr versus H19_2 LNAs. Pictures are representative of n=3 independent experiments. Scale bar = 100 µm. Transcript levels of mRNAs were normalized to *Hprt1* expression. Graphs show floating bars with a line at the mean with all data points plotted. A paired, two-tailed Student´s t-test was used to assess statistical significance across n=3 independent experiments performed in n=3 technical replicates each. *p<0,05, **p<0,01. If applicable, p-values are indicated within the panel. Modified after Schmidt et al. (2018)[204].

3.4 Gene expression of early progenitors remains high in *H19*-ablated differentiated primary brown adipocytes

Protein delta homolog 1 (*Dlk1*), also termed *adipocyte differentiation inhibitor protein* or *preadipocyte factor 1* is known to be mostly expressed in preadipocytes and declines with brown adipocyte differentiation[211]. To analyse whether the expression of *Dlk1* and other preadipocyte markers remained high in the *H19*-ablated cells and whether the defect of adipogenesis resulted from a failure in the repression of preadipocyte markers, we checked the expression of genes relevant to adipocyte progenitor function in SVF adipocyte precursor cells isolated from 1° BAT and treated with RNAi *H19.* In 1° BAT the expression of all adipocyte precursor genes remained high, whereas *Runt Related Transcription Factor 2* (*Runx2*) and *Platelet Derived Growth Factor Receptor Alpha* (*Pdgfra*) were significantly upregulated (Figure 11A). This result demonstrates incomplete differentiation of 1° BAT cells. In scWAT and vWAT no gene was significantly changed upon *H19* loss (Figure 11B, C).

From these results, we conclude that *H19*-ablation leads to a defect in the transcriptional cascade of genes required for terminal brown adipocyte differentiation.

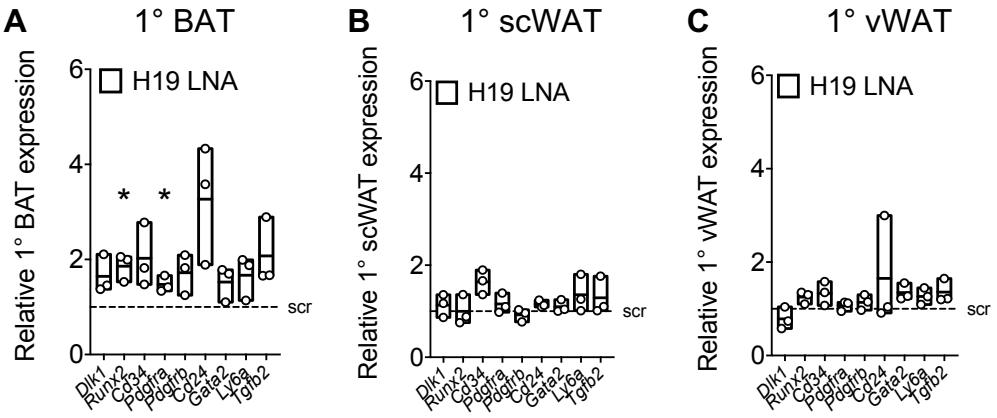

Figure 11: Failed repression of early progenitor genes in committed 1° BAT upon *H19* ablation
Relative expression of indicated mRNAs in (A) BAT, (B) scWAT, and (C) vWAT derived 1° adipocytes after transfection with 25 nM scr versus H19 LNAs. Transcript levels of mRNAs were normalized to *Hprt1* expression. Graphs show floating bars with a line at the mean with all data points plotted. A paired, two-tailed Student´s t-test was used to assess statistical significance across n=3 independent experiments performed in n=3 technical replicates each. *p<0,05. Modified after Schmidt et al. (2018)[204].

3.5 The imprinted lncRNA *H19* controls oxidative metabolism in BAT

To investigate the cell-intrinsic and metaboregulatory properties of *H19* we performed *in vitro* loss-of-function approaches. For this SVFs were isolated from BAT, scWAT, and vWAT from C57BL/6 N mice and *H19* RNAi was performed to analyse *H19*-deficient adipocytes. Cellular analyses using Seahorse technology indicated and calculation of coupling efficiencies (CEs) confirmed that *H19* RNAi impaired oxidative metabolism (Figure 12A, B) and impaired uncoupling (Figure 12C) in fully differentiated brown adipocytes. Calculations of CEs are important for determining brown adipocyte function under conditions where too few brown fat cells are formed. We observed increased CEs (reduced uncoupling), suggesting that not only less brown adipocytes are formed but also that the individual brown adipocyte is less proficient in uncoupled respiration. No alterations in CE were seen for 1° scWAT and 1° vWAT (Figure 12C) which stresses the specificity of *H19* effects in 1° BAT.

Thus, we conclude that *H19* supports oxidative metabolism and mitochondrial dynamics in mature adipocytes in a BAT-specific manner.

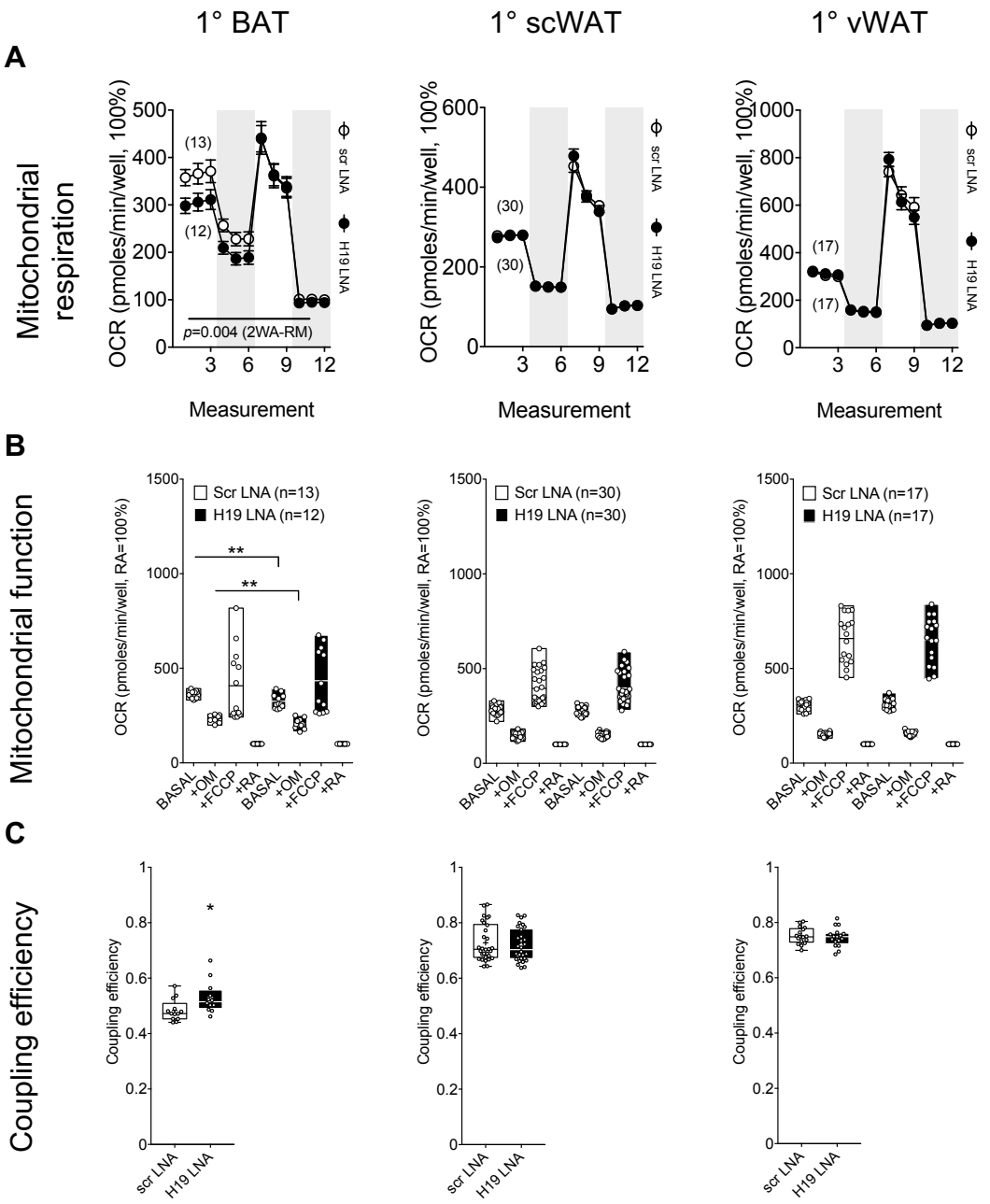

Figure 12: Loss of *H19* in 1° BAT impairs oxidative metabolism and uncoupling
(A) Oxygen consumption rates (OCR) in 1° adipocytes derived from indicated depots transfected with 25 nM scr versus *H19* LNA using Seahorse technology. Alternating white and grey backgrounds depict injections of oligomycin, FCCP, and rotenone plus antimycin A. The number of wells measured are indicated in each panel. A two-way analysis of variance (ANOVA) test with repeated measurements (2WA-RM) was applied to assess statistical significance. (B) Relative OCRs in BAT (*left*), scWAT (*middle*), and vWAT (*right*) derived 1° adipocytes under basal conditions and after addition of oligomycin, FCCP, and rotenone plus antimycin A after transfection with 25 nM scr versus *H19* LNAs. The number of wells measured are indicated in each panel. Graphs represent floating bars with a line at the mean with all data points plotted. Unpaired, two-tailed Student´s t-test was applied to assess statistical significance. (C) Coupling efficiencies (CEs) calculated from absolute OCRs from (A) according to Brand et al. (2011)[212]. Unpaired, two-tailed Student´s t-test was applied to assess statistical significance. *p<0.05, **p<0.01. If applicable, p-values are indicated within the panel. Modified after Schmidt et al. (2018)[204].

3.6 *H19* is located in nuclear and cytoplasmic compartments in 1° BAT

H19 was reported to reside in nuclear, but also cytoplasmic and ribosomal fractions in other cell types[213,214]. To determine localization of *H19* in 1° BAT, subcellular fractionation experiments were performed upon knockdown of *H19* with either H19 LNA (acts mainly in the nuclei) or H19 siRNA (acts preferentially (predominantly) in the cytoplasm). When analysing *H19* gene expression in *scr*-transfected cells we could see that *H19* was equally expressed in the nuclear and cytoplasmic fractions (Figure 13A). Furthermore, *H19* expression was significantly decreased upon RNAi LNA knockdown in both compartments when normalized to *Hprt* or the unspliced heteronuclear RNA (*hnNctc1*) (Figure 13A). Thus, *H19* ablation was observed across subcellular compartments using H19 LNA.

To show that the subcellular fraction was free of contamination from other fractions, a standard procedure[215,216] was used to compare the expression of *hnNctc1* and the nuclear RNA *RNU6* in the cytoplasmic and nuclear fractions. Analysing the localization of *hnNctc1* and *RNU6* RNA, they were found to be highly enriched in nuclear as appose to cytosolic fractions, which was shown for both knockdown techniques (Figure 13B).

Thus, we conclude that *H19* is located equally in nuclear and cytoplasmic fractions and LNA knockdown leads to efficient silencing of both cytosolic as well as nuclear *H19* pools. Moreover, fractions were free of contaminations as shown by the precedence of nuclear RNA transcripts solely in the nucleus.

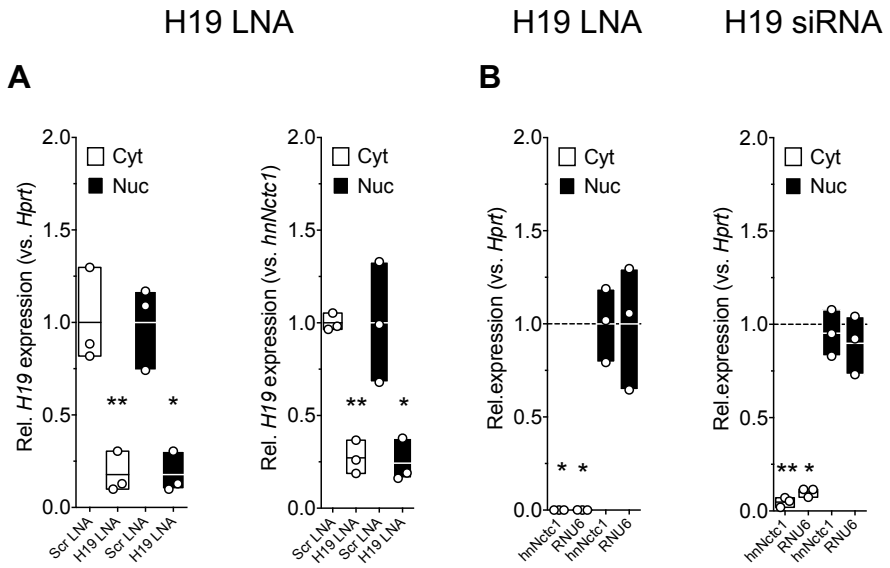

Figure 13: *H19* is located in nuclear and cytoplasmic compartments in 1° BAT
(A) *H19* and (B) nuclear transcripts *HnNctc1* and *RNU6* expression in nuclear and cytoplasmic compartments of 1° BAT transfected with H19 LNA or siH19 inhibitors followed by subcellular fractionation using PARIS kits. Transcript levels of mRNAs were normalized to (A, *left*) and (B) *Hprt1* and (A, *right*) *hnNctc1* expression. Graphs show floating bars with a line at the mean with all data points plotted. An unpaired, two-tailed Student´s t-test was applied to assess statistical significance across n=3 independent experiments performed in n=3 technical replicates each. *p<0.05, **p<0.01. Experiment was performed with kind help by Dr. M. Bilban. Modified after Schmidt et al. (2018)[204].

3.7 Cold/diet-induced obesity (DIO)-evoked alterations in *H19* are independent of *H19-Igf2* imprinting regulation

Historically, *H19* was discovered as monoallelically expressed, maternal gene. The expression of a gene from only one parental strand is an epigenetic process called 'genomic imprinting' (see **1.4**). Here, the reciprocally expressed *H19-Igf2* imprinted gene cluster is regulated by the enhancer-blocking properties of CCCTC-Binding Factor (CTCF) proteins[155,169]. To investigate whether *H19-Igf2* imprinting is altered we performed RNAi of *Ctcf* in primary brown adipocytes and analysed the gene expression of *Ctcf* and *Igf2* in BAT of mice exposed to either 4°C or 22°C and mice which have been fed either a HFD or a CD. No defects in BAT adipogenesis were visible after *Ctcf* RNAi (Figure 14A, B). Furthermore, BAT *Ctcf* and *Igf2* levels were unaltered by cold or DIO conditions (Figure 14C). Thus, we conclude that cold/DIO-evoked alterations in *H19* are not based on altered *H19-Igf2* imprinting.

The first exon of *H19* encodes the *miR-675* gene. To exclude that the *H19*-encoded *miR-675* controls BAT differentiation and function we analysed the expression of *miR-*

675-3p and *miR-675-5p* in BAT of mice exposed to either 4°C or 22°C and mice which have been exposed to either HFD or CD. Both isoforms were not expressed in BAT (Figure 14D, E). Therefore, we conclude that *miR-675* is not involved in brown adipocyte differentiation.

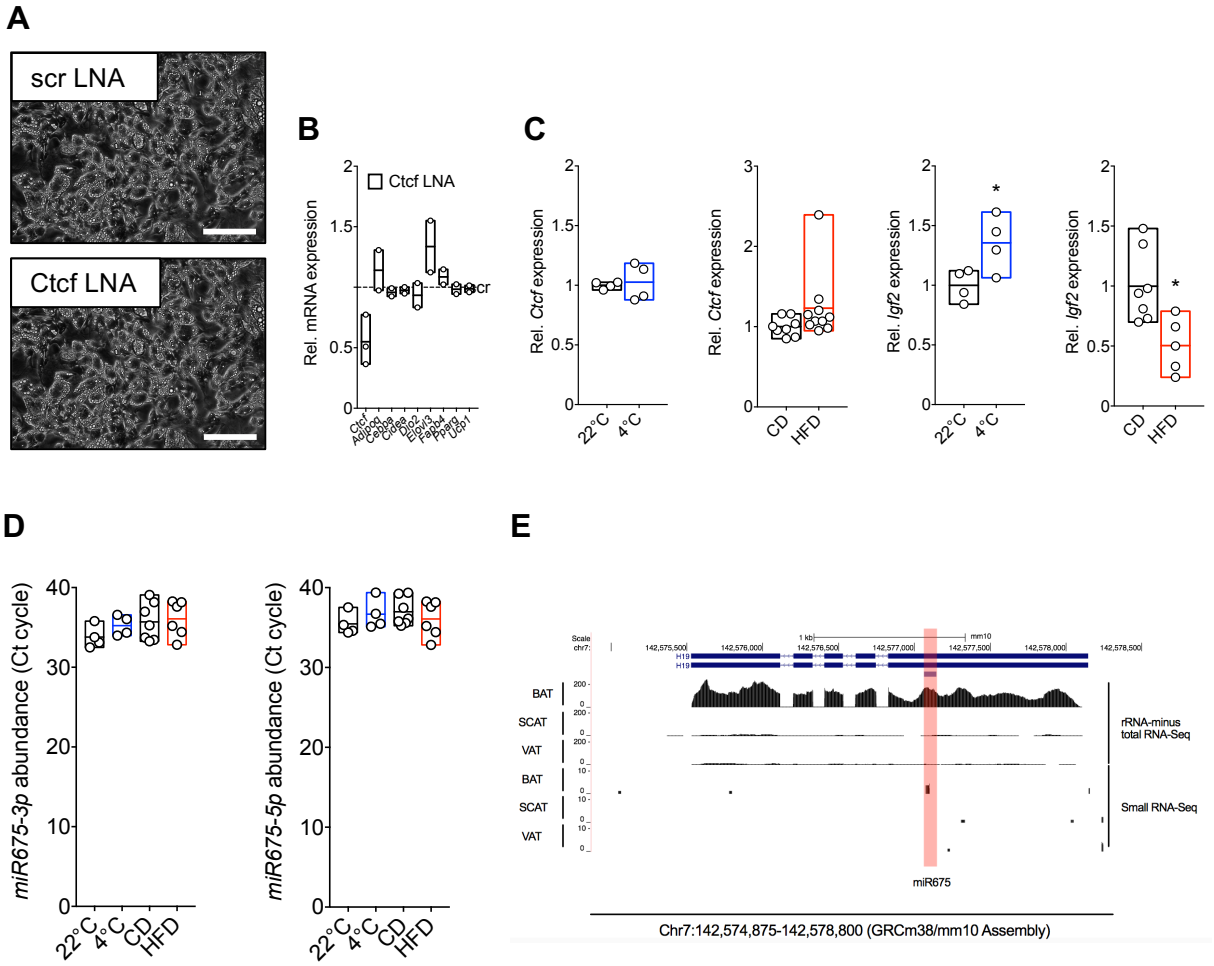

Figure 14: *H19/Igf2* cluster and *miR-675* are not affected by alterations of *H19* upon cold or DIO
(A) Photomicrographs and (B) expression of indicated mRNAs in 1° BAT after transfection with 25 nM scr versus *Ctcf* LNAs. Pictures are representative of n=2 independent experiments. Scale bar = 250 µm. Gene expression analysis was performed twice in n=3 technical replicates each. Transcript levels of mRNAs were normalized to *Hprt1* expression. Graphs show floating bars with a line at the mean with all data points plotted. (C) Relative BAT *Ctcf* expression (*left and middle left*) in lean C57BL/6 N male mice housed at 22°C (n=4) versus 24h of 4°C (n=4) or exposed to chronic HFD (n=10) versus CD (n=8) feeding. Relative BAT *Igf2* (*right and middle right*) expression in lean C57BL/6 N male mice housed at 22°C (n=4) versus 24h of 4°C (n=4) or exposed to chronic HFD (n=5) versus CD (n=7) feeding. Transcript levels of mRNAs were normalized to *Hprt1* expression. Graphs show floating bars with a line at the mean with all data points plotted. An unpaired, two-tailed Student´s t-test was applied to assess statistical significance. (D) Relative *miR-675-3p* and *miR-675-5p* abundance (CT cycle) in lean C57BL/6 N male mice housed at 22°C (n=4) versus 24h of 4°C (n=4) or exposed to HFD (n=6) versus CD (n=7) feeding. (C) and (D) blue = 4°C, red = HFD. Graphs show floating bars with a line at the mean with all data points plotted. (E) Illustration of *H19* (top) and *miR-675* (*bottom*) abundances in indicated ATs determined by total (*top*) or small RNA-Seq (*bottom*, UCSC Genome Browser). *p<0,05. Modified after Schmidt et al. (2018)[204]. DIO = diet induced obesity.

3.8 *H19* overexpression prevents DIO and results in increased BAT energy expenditure *in vivo*

Impairments in EE because of defects in brown fat differentiation and function make mice more susceptible to DIO-induced weight gains. Additionally, they have an increased probability to develop metabolic diseases[217–219]. To investigate the role of *H19* in energy metabolism and EE *in vivo* we exposed *H19* gain-of-function[210] and Control mice to HFD or CD. The mouse model Tg(Igf2/LacZ,H19)YZ15Aco contains a 130 kb YAC transgene, YZ, which harbours the *Igf2* and *H19* genomic regions. In this mouse model the *Igf2* coding sequence is interrupted with the LacZ reporter gene. The YZ15 line carries 10 copies of the transgene. When adjusted for transgene copy number, the level of activity in the ten copy mouse line was suggested to be approximately 20% as transgenic YZ15 embryos express *H19* at two times more compared to non-transgenic littermates, instead of eleven times as would be assumed if the transgene copy was fully active[210].

Metabolic phenotyping of these mice showed that *H19* expression is ubiquitously induced (Figure 15A) without changes in *Ctcf* (Figure 15B) and *Igf2* (Figure 15C) expression or body length (Figure 15D). *H19* overexpression prevented DIO-mediated weight gains (Figure 15E) and improved insulin sensitivity (Figure 15F). Surprisingly, glucose tolerance was decreased (Figure 15G) in *H19* gain-of-function mice[220]. The beneficial effect of *H19* overexpression in DIO was presumably linked to an increase in energy expenditure (EE) (Figure 15I), a trend towards increased lipid mobilisation at 22°C (Figure 15J) and oxygen consumption at 22°C, 4°C, and after norepinephrine (NE) administration at 4°C for 24 h (Figure 15K). Furthermore, the *H19*-dependent induction of EE in obese mice co-occurred with increased scWAT 'beiging' (Figure 15N) despite little alterations in BAT thermogenesis (Figure 15M). The observed rise in EE tended towards prevention of DIO-evoked increases in scWAT and vWAT adiposity (Figure 15H) and precluded DIO-associated elevations in serum cholesterol (Figure 15O) but not triglycerides (Figure 15P). Overall these results indicate an improved BAT function in *H19* TG mice.

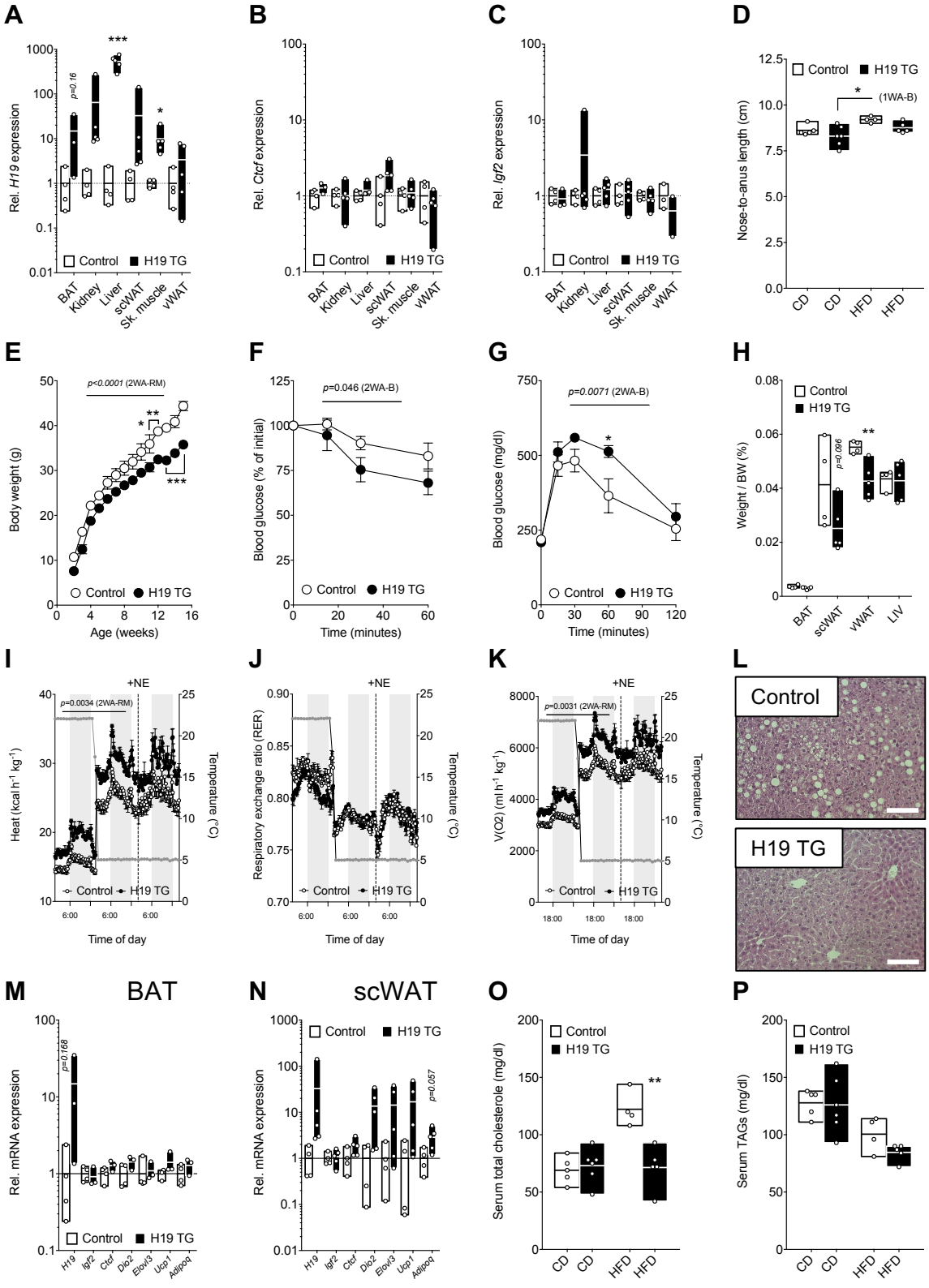

Figure 15: *H19* overexpression protects from obesity by increasing energy expenditure and scWAT 'beiging'

(A) Relative *H19* expression in indicated tissues from male, HFD-fed Control (n=4) versus H19 TG (n=3 for Bat, n=5 for other tissues) mice. (B) Relative *Ctcf* expression in indicated tissues from male, HFD-fed Control (n=4) versus H19 TG (n=3 BAT, n=5 for other tissues) mice. (C) Relative *Igf2* expression in indicated tissues from male, HFD-fed Control (n=4) versus H19 TG (n=2 for vWAT, n=3 BAT and n=5 for other tissues) mice. (A), (B), and (C) Transcript levels of mRNAs were normalized to *Hprt1* expression.

Graphs represent floating bars with a line at the mean and all data points plotted. Unpaired, two-tailed Student´s t-test were used to assess statistical significance. (D) Nose-anus body length in male, CD-fed Control (n=5) versus H19 TG (n=6) and HFD-fed Control (n=4) versus H19 TG (n=5) mice. Graphs represent floating bars with a line at the mean and all data points plotted. One-Way ANOVAs with Bonferroni *post hoc* tests (1WA-B) were used to assess statistical significance. (E) Body weight of male, HFD-fed Control (n=4-5) versus H19 TG (n=4-5) mice. A 2WA-RM with Bonferroni *post hoc* correction for multiple comparisons (2WA-B) was applied to assess statistical significance. (F) Insulin tolerance test of male, HFD-fed Control (n=4) versus H19 TG (n=6) mice. (G) Glucose tolerance test of male, HFD-fed Control (n=5) versus H19 TG (n=5) mice. For ITT and GTT, a 2WA-RM with Bonferroni *post hoc* correction for multiple comparisons (2WA-B) was applied to assess statistical significance. (H) Tissue/body weight (BW) ratios in male, HFD-fed Control (n=4) versus H19 TG (n=5) mice. Graphs represent floating bars with a line at the mean and all data points plotted. An unpaired, two-tailed Student´s t-test was applied to assess statistical significance between genotypes. (I) EE in male, HFD-fed Control (n=4) versus H19 TG (n=5) mice. A 2WA-RM with Bonferroni *post hoc* correction (2WA-B) was applied to assess statistical significance. (J) Respiratory Exchange Rations (RER) in male, HFD-fed Control (n=4) versus H19 TG (n=5) mice. (K) Oxygen consumption in male, HFD-fed Control (n=4) versus H19 TG (n=5) mice. A 2WA-RM with repeated measures plus Bonferroni *post hoc* test was applied to assess statistical significance. (L) Representative photomicrograph of liver sections from HFD-fed Control versus H19 TG mice. Scale bar = 100 µm. (M) Relative BAT expression of indicated mRNAs from male, HFD fed Control (n=4) versus H19 TG (n=3) mice. (N) Relative scWAT expression of indicated mRNAs from male, HFD-fed Control (n=4) versus H19 TG (n=5) mice. (M, N) Transcript levels of mRNAs were normalized to *Hprt1* expression. Graphs represent floating bars with a line at the mean and all data points plotted. An unpaired, two tailed Student´s t-test was used to assess statistical significance. (O) Serum cholesterol levels in HFD-fed Control (n=4) versus H19 TG mice (n=5). (P) Serum triglyceride levels in HFD-fed Control (n=4) versus H19 TG (n=5) mice. For (O) and (P), graphs represent floating bars with a line at the mean and all data points plotted. Unpaired, two-tailed Student´s t-test were applied to assess statistical significance between genotypes. *p<0,05, **p<0,01, ***p<0,001. If applicable p-values are indicated within the panel. Modified after Schmidt et al. (2018)[204].

When analysing adipocyte and liver morphologies microscopically, we observed that *H19* overexpression prevented 'whitening' of BAT (Figure 16, *left*), reduced vWAT (Figure 16, *right*) but not scWAT (Figure 16, *middle*) hypertrophy and the development of steatosis in obese animals (Figure 15L).

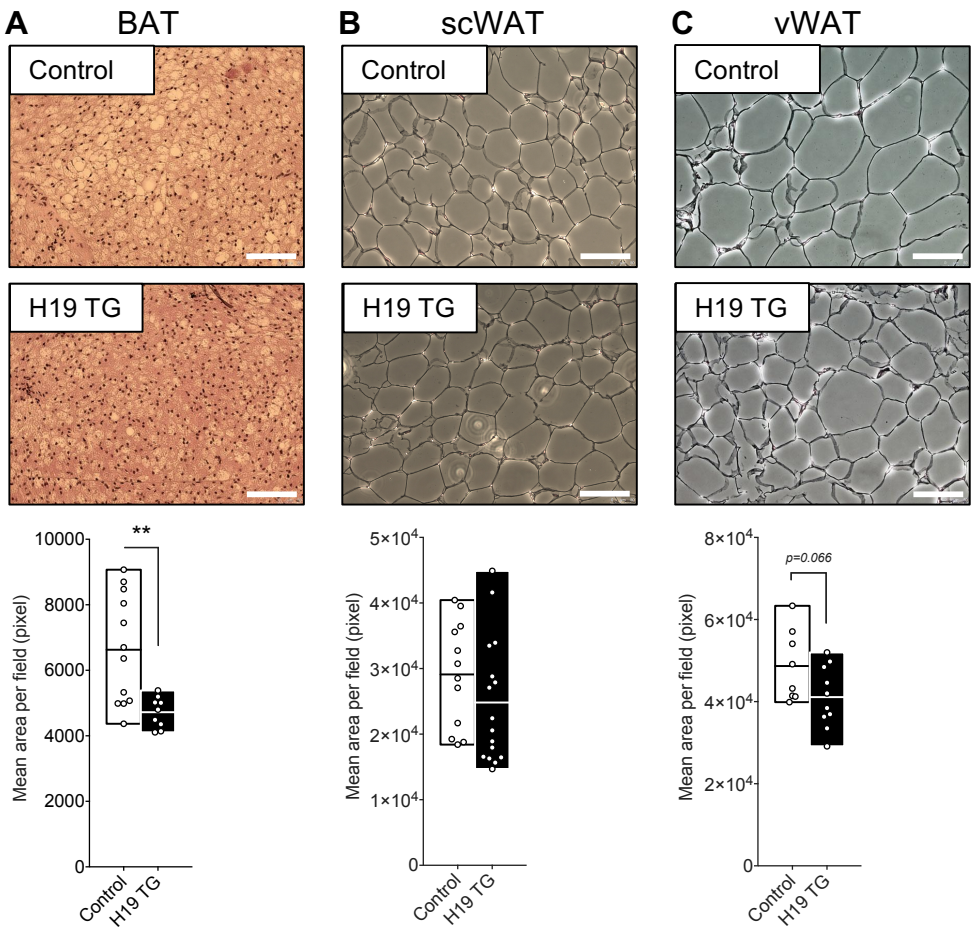

Figure 16: *H19* prevents whitening of BAT and reduces vWAT hypertrophy
Representative photomicrograph of (A, *top*) BAT, (B, *top*) scWAT and (C, *top*) vWAT from HFD-fed Control versus H19 TG mice (A, B, C; *middle*). Scale bar = 100 µm. Automated quantification of adipocyte mean area per field in H&E stained (A, *bottom*) BAT sections from male, HFD-fed Control (n=12 fields) versus H19 TG (n=9 fields) mice, (B, *bottom*) scWAT sections from male, HFD-fed Control (n=12 fields) versus H19 TG (n=16 fields) mice, and (C, *bottom*) vWAT sections from male, HFD-fed Control (n=8 fields) versus H19 TG (n=10 fields) mice. Graphs represent floating bars with a line at the mean and all data points plotted. An unpaired, two-tailed Student´s t-test was applied to assess statistical significance between genotypes. **p<0.01. If applicable p-values are indicated within the panel. Modified after Schmidt et al. (2018)[204].

H19 overexpression in lean mice led to little changes in body weight (Figure 17A), insulin sensitivity (Figure 17B), glucose clearance (Figure 17C), EE (Figure 17D), and did not affect lipid mobilisation (Figure 17 E), oxygen consumption (Figure 17 F), BAT thermogenesis (Figure 17G), adiposity (Figure 17I) or scWAT 'beiging' (Figure 17H).

Furthermore, food and water intake as well as locomotion was unchanged between H19 TG and Control mice on both diets (Figure 18).

Here, we conclude that *H19* is beneficial during DIO, but does not cause detrimental effects in lean mice.

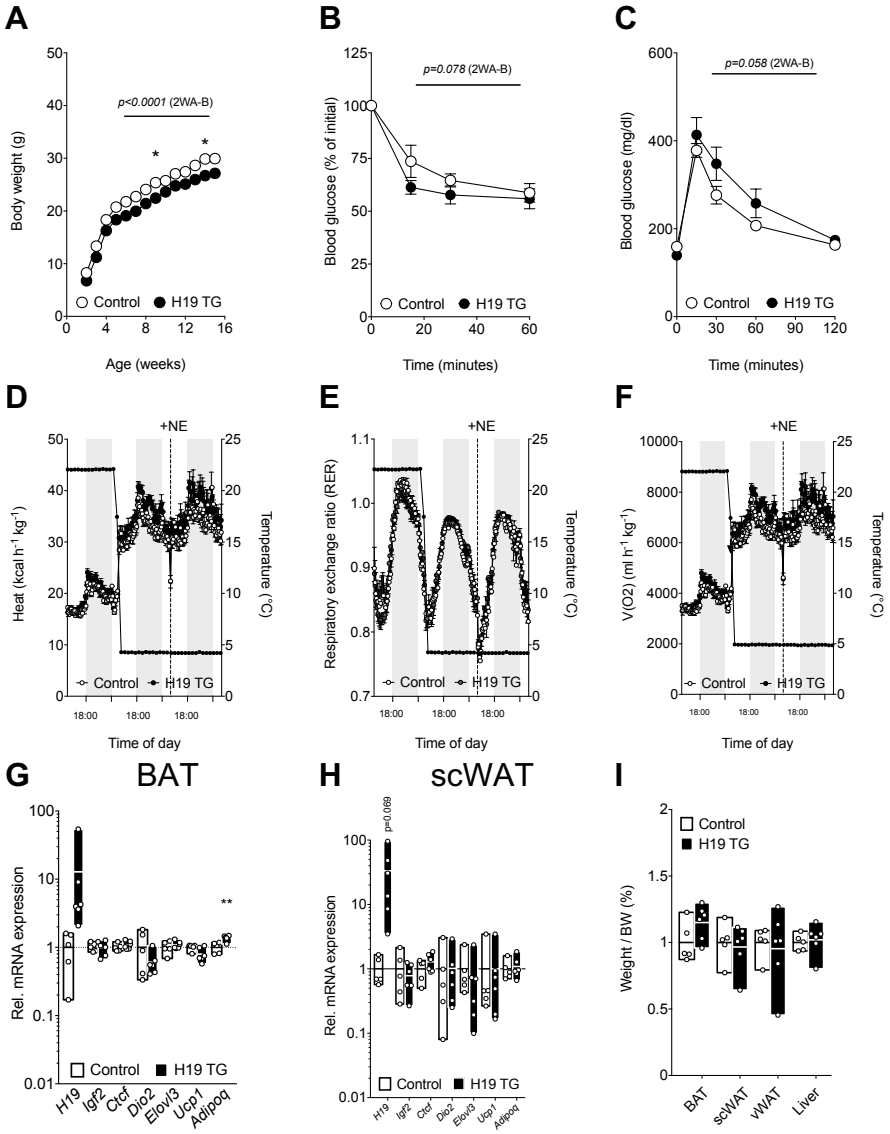

Figure 17: *H19* overexpression causes minor increases of energy expenditure in lean mice
(A) Body weight of CD-fed Control (n=5) versus H19 TG (n=6) mice. A 2WA-RM with repeated measures plus Bonferroni *post hoc* test was applied to assess statistical significance. (B) Insulin tolerance test of male, CD-fed Control (n=6) versus H19 TG (n=5) mice. (C) Glucose tolerance test of male, CD-fed Control (n=5) versus H19 TG (n=5) mice. For the ITT and the GTT a 2WA-RM with repeated measures plus Bonferroni *post hoc* test was applied to assess statistical significance. (D) EE and (E) RER in male, CD-fed Control (n=4) versus H19 TG (n=6) mice. (F) Oxygen consumption in male, HFD-fed Control versus H19 TG mice. (G) Relative BAT expression of indicated mRNAs from male, CD-fed Control (n=5) versus H19 TG (n=6) mice. (H) Relative scWAT expression of indicated mRNAs from male, CD-fed Control (n=5) versus H19 TG (n=6) mice. (G, H) Transcript levels of mRNAs were normalized to *Hprt1* expression. (I) Tissue/body weight ratio in male, CD-fed Control (n=5) versus H19 TG (n=6) mice. (G, H, I) Graphs represent floating bars with a line at the mean with all data points plotted and unpaired, two-tailed Student´s t-test were used to assess statistical significance. *p<0,05, **p<0,01. If applicable p-values are indicated within the panel. Modified after Schmidt et al. (2018)[204].

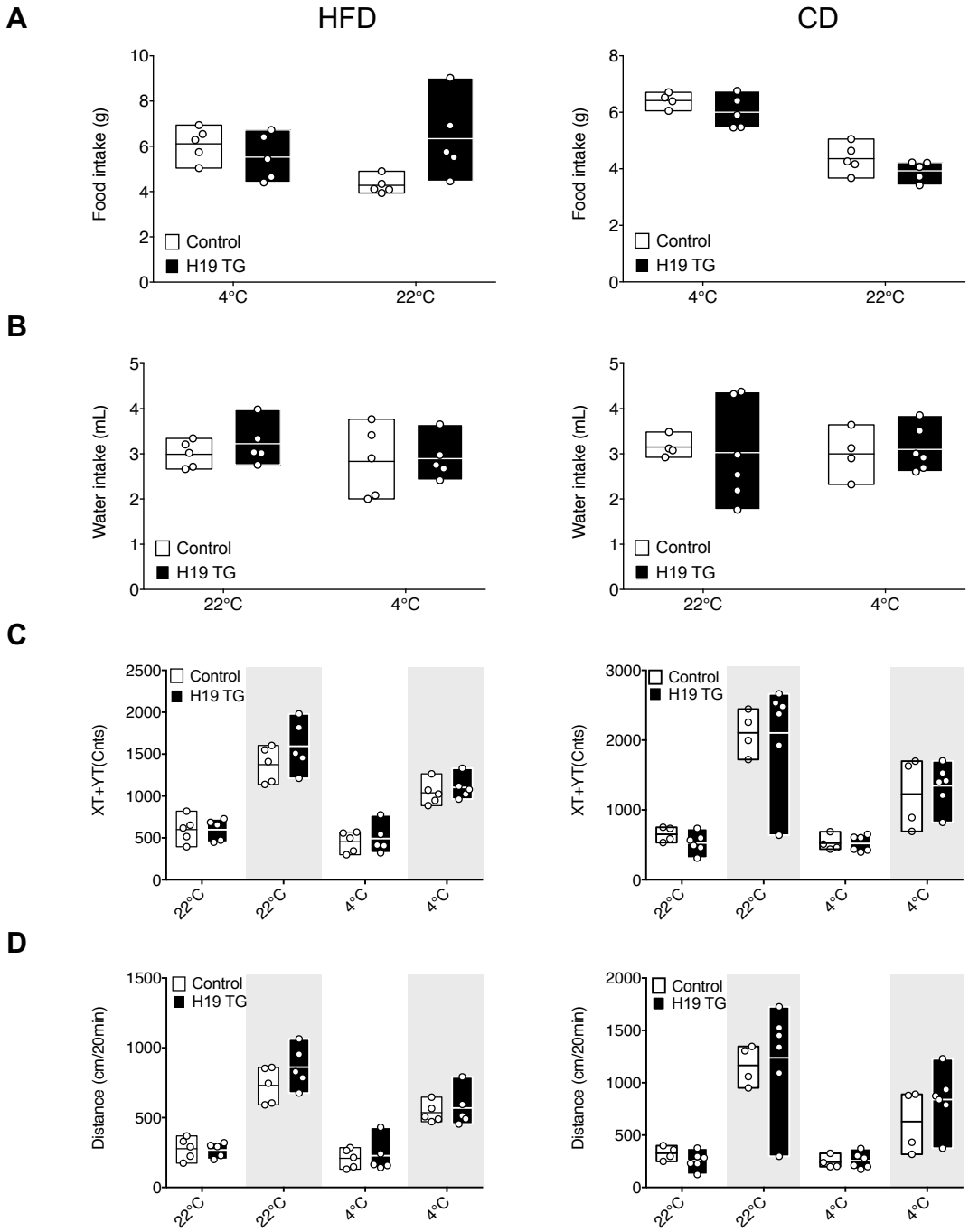

Figure 18: Systemic overexpression of *H19* does not influence food intake, water intake, and locomotion

(A) Food intake of HFD-fed (*left*) Control (n=5) versus H19 TG (n=5) mice and of CD-fed (*right*) Control (n=5 at 22°C and n=4 at 4°C) versus H19 TG (n=5) mice. (B) Water intake of HFD-fed (*left*) Control (n=5) versus H19 TG (n=5) mice and of CD-fed (*right*) Control (n=4) versus H19 TG (n=6) mice. (C) Locomotion of HFD-fed (*left*) Control (n=5) versus H19 TG (n=5) mice and of CD-fed (*right*) Control (n=4) versus H19 TG (n=6) mice. (D) Distance of HFD-fed (*left*) Control (n=5) versus H19 TG (n=5) mice and of CD-fed (*right*) Control (n=4) versus H19 TG (n=6) mice. Graphs represent floating bars with a line at the mean.

3.9 *H19* loss in fat impairs energy expenditure (EE) and sensitizes towards DIO-induced weight gain

To investigate the fat-intrinsic effects of *H19* in an adipocyte-intrinsic manner, we conditionally deleted H19-DMR (an epigenetic regulator that controls expression of *H19*) by crossing female $H19^{flDMR/flDMR}$ mice with male *Adipoq-cre* expressing mice ($H19^{\Delta AT}$) (Figure 19A). $H19^{\Delta AT}$ mice showed decreased *H19* expression in BAT (Figure 19B) and 1° BAT cells (Figure 19C) whereas no decrease in expression was observed in other tissues (Figure 19B). $H19^{\Delta AT}$ mice gained more body weight compared to Control mice upon HFD (Figure 19D) but not on CD feeding (Figure 20A). The alterations in insulin sensitivity (Figure 19E, Figure 20B) and glucose tolerance (Figure 19F, Figure 20C) were negligible on both diets. Importantly, BAT-specific *H19* loss decreased EE (Figure 19H, Figure 20E) and oxygen consumption (Figure 19J, Figure 20G) on both diets, tended towards decreased lipid oxidation (Figure 19I) at 4°C, and increased scWAT adiposity (Figure 19G) in obese, but not lean knockout mice (Figure 20D, F). Food and water intake as well as locomotion was unchanged between $H19^{\Delta AT}$ and Control mice on both diets (Figure 21).

From these results, we conclude that BAT function is decreased in $H19^{\Delta AT}$ mice, especially under DIO condition.

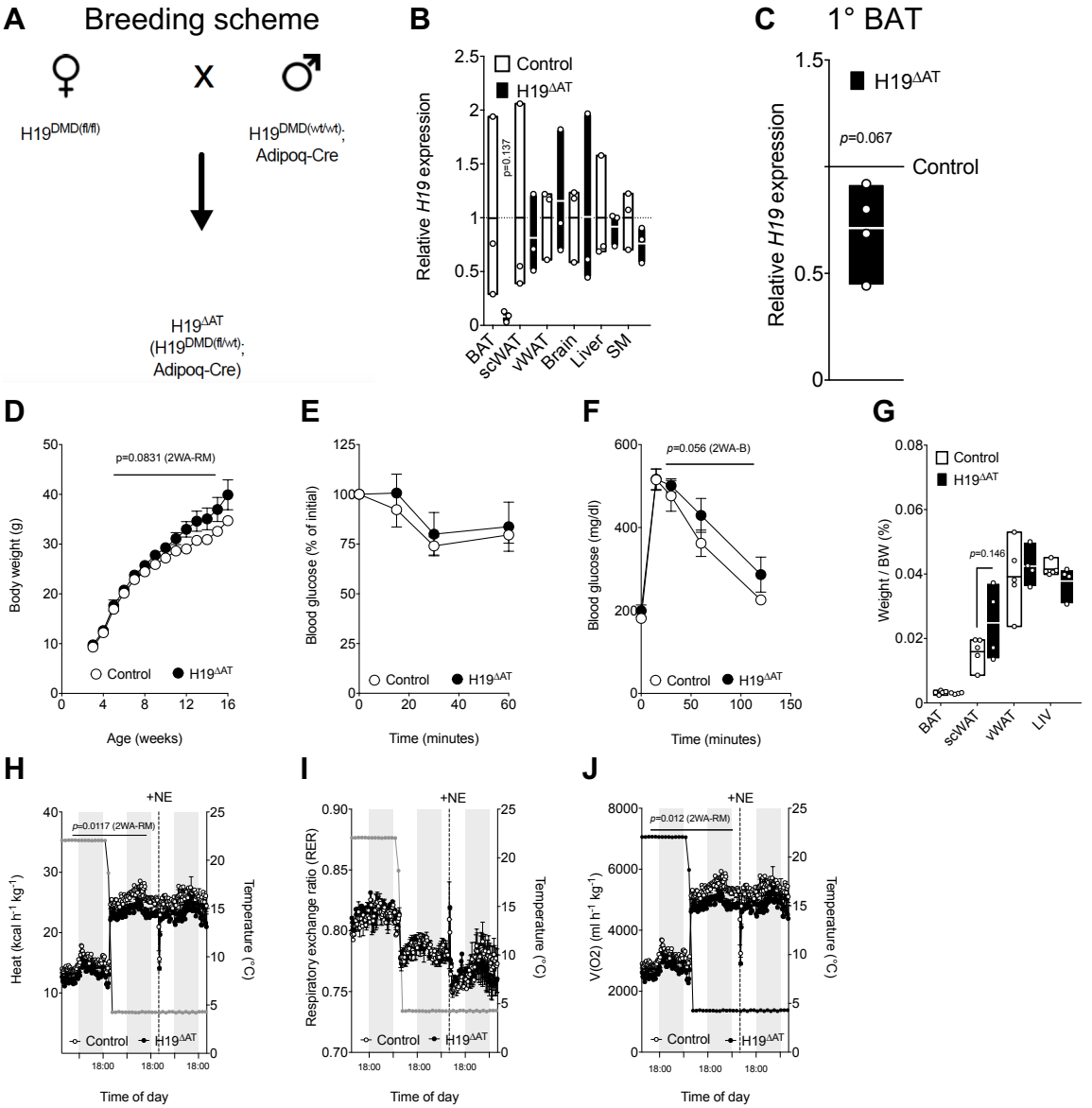

Figure 19: Fat-specific deletion of *H19* sensitizes towards DIO-associated weight gains and impairments in energy expenditure

(A) Mating strategy for parental allele-of-origin specific deletion of the *H19* differentially methylated domain (DMD) in adipose tissue. (B) *H19* expression in indicated tissues from male Control (n=3) versus H19$^{\Delta AT}$ (n=3) mice. Transcript levels of mRNAs were normalized to *Hprt1* expression. Graphs represent floating bars with a line at the mean. An unpaired, two-tailed Student´s t-test was applied to asses statistical significance. (C) *H19* expression in BAT derived 1° adipocytes from male Control versus H19$^{\Delta AT}$ mice. Transcript levels of mRNAs were normalized to *Hprt1* expression. Graphs represent floating bars with a line at the mean. A paired, two-tailed Student´s t-test was applied to assess statistical significance across n=4 independent experiments performed in n=3 technical replicates each. (D) Body weight of male, HFD-fed Control (n=5) versus H19$^{\Delta AT}$ (n=4) mice. A 2WA-RM with plus Bonferroni *post hoc* test was applied to assess statistical significance. (E) Insulin tolerance test of male, HFD-fed Control (n=5) versus H19$^{\Delta AT}$ (n=4) mice. (F) Glucose tolerance test of male, HFD-fed Control (n=5) versus H19$^{\Delta AT}$ (n=4) mice. For (E) and (F), a 2WA-RM plus Bonferroni *post hoc* test was applied to assess statistical significance. (G) Tissue/body weight ratio in male, HFD-fed Control (n=5) versus H19$^{\Delta AT}$ (n=4) mice. Graphs represent floating bars with a line at the mean. An unpaired, two-tailed Student´s t-test was applied to assess statistical significance. (H) EE in male, HFD-fed Control (n=5) versus H19$^{\Delta AT}$ (n=4) mice. A 2WA-RM test was applied to assess statistical significance. (I) RER in male, HFD-fed Control (n=5) versus H19$^{\Delta AT}$ (n=4) mice. (J) Oxygen consumption in male, HFD-fed Control (n=5) versus H19$^{\Delta AT}$ (n=4) mice. A 2WA-RM test was applied to assess statistical significance. If applicable p-values are indicated within the panel. Modified after Schmidt et al. (2018)[204].

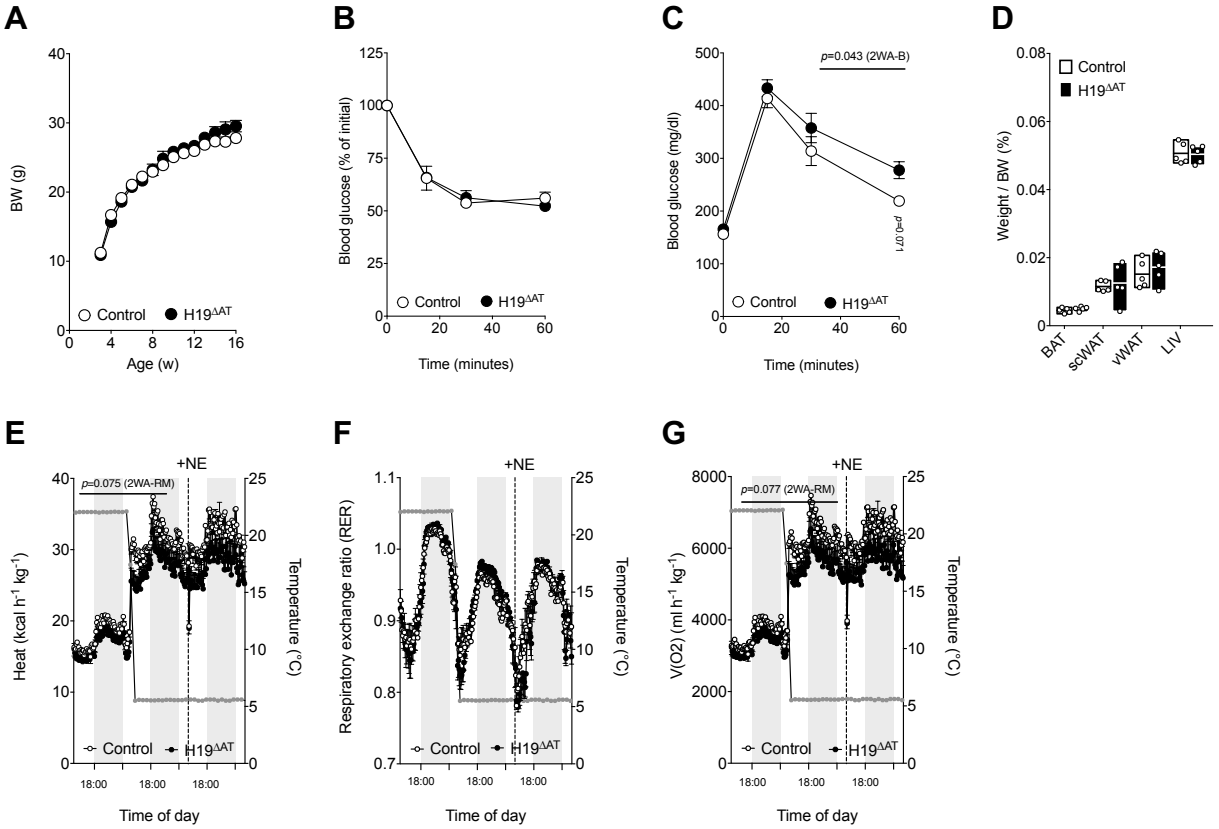

Figure 20: Fat-specific deletion of *H19* causes minor decreases in energy expenditure in lean mice
Body weight of male, CD-fed Control (n=5) versus H19$^{\Delta AT}$ (n=5) mice. (B) Insulin tolerance test of male, CD-fed Control (n=5) versus H19$^{\Delta AT}$ (n=5) mice. (C) Glucose tolerance test of male, CD-fed Control (n=5) versus H19$^{\Delta AT}$ (n=5) mice. A 2WA-RM with repeated measures plus Bonferroni *post hoc* test was applied to assess statistical significance. (D) Tissue/body weight ratio in male, CD-fed Control (n=5) versus H19$^{\Delta AT}$ (n=5) mice. Graphs represent floating bars with a line at the mean. (E) EE in male, CD-fed Control (n=5) versus H19$^{\Delta AT}$ (n=5) mice. A 2WA-RM with repeated measures plus Bonferroni *post hoc* test was applied to assess statistical significance. (F) RER in male, CD-fed Control (n=5) versus H19$^{\Delta AT}$ (n=5) mice. A 2WA-RM with repeated measures plus Bonferroni *post hoc* test was applied to assess statistical significance. (G) Oxygen consumption in male, CD-fed Control (n=5) versus H19$^{\Delta AT}$ (n=5) mice. A 2WA-RM with repeated measures plus Bonferroni *post hoc* test was applied to assess statistical significance. If applicable p-values are indicated within the panel. Modified after Schmidt et al. (2018)[204].

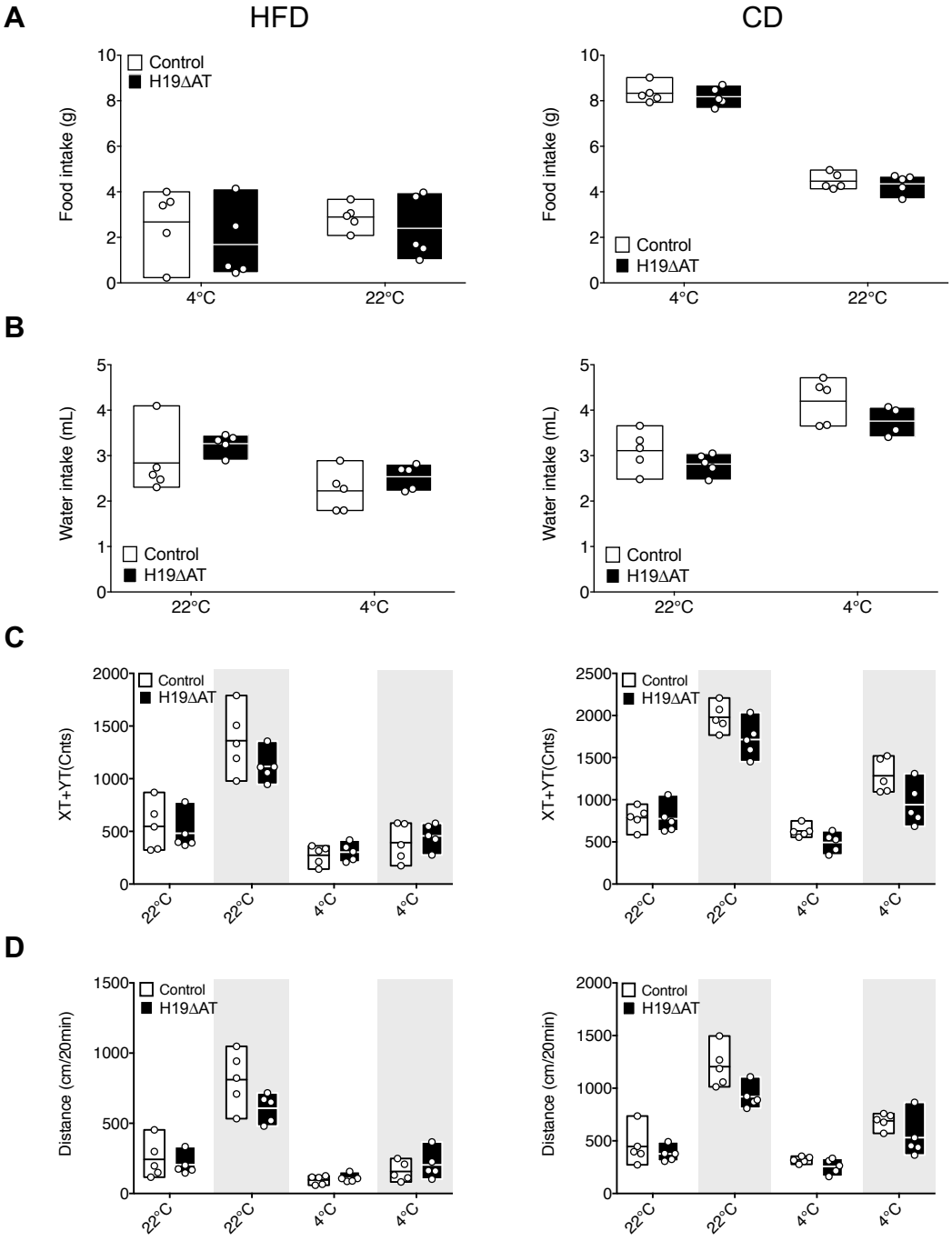

Figure 21: Fat-specific deletion of *H19* does not influence food intake, water intake, and locomotion

(A) Food intake of HFD-fed (*left*) Control (n=5) versus H19$^{\Delta AT}$ (n=5) mice and of CD-fed (*right*) Control (n=5) versus H19$^{\Delta AT}$ (n=5) mice. (B) Water intake of HFD-fed (*left*) Control (n=5) versus H19$^{\Delta AT}$ (n=5) mice and of CD-fed (*right*) Control (n=5) versus H19$^{\Delta AT}$ (n=5 at 22°C and n=4 at 4°C) mice. (C) Locomotion of HFD-fed (*left*) Control (n=5) versus H19$^{\Delta AT}$ (n=5) mice and of CD-fed (*right*) Control (n=5) versus H19$^{\Delta AT}$ (n=5) mice. (D) Distance of HFD-fed (*left*) Control (n=5) versus H19$^{\Delta AT}$ (n=5) mice and of CD-fed (*right*) Control (n=4) versus H19$^{\Delta AT}$ (n=5) mice. Graphs represent floating bars with a line at the mean.

3.10 *H19* regulates brown adipose mitochondrial biogenesis *in vitro* and *in vivo*

Chronic induction of thermogenesis through cold temperature requires mitochondrial biogenesis and rearrangements of mitochondrial network via fission and fusion in BAT[221,222]. As we observed cell-intrinsic differences in oxidative metabolism of *H19*-deficient (Chapter 3.5) adipocytes, we wanted to investigate whether mitochondrial morphology in BAT was changed using electron microscopy (EM). Global factors such as mitochondrial perimeter (Figure 22G) and area (Figure 22H) were unchanged. However, we observed defects in mitochondrial architecture. Cristae formation was perturbed in obese BAT of Control mice (Figure 22B, C) but not *H19* TG mice (Figure 22E, F). In addition, we analysed the gene expression of mitochondrial biogenesis as well as fission and fusion markers. The expression of genes involved in mitochondrial biogenesis was decreased in BAT and scWAT of obese mice (Figure 22I). *H19* overexpression was able to reverse the DIO-evoked defects in gene expression in BAT (Figure 22I), but not in scWAT (Figure 22J). Mitochondrial fission and fusion marker *dynamin-related protein 1* (*Drp1*) and *mitochondrial fission factor* (*Mff*) were significantly decreased along with other markers of the panel which showed a tendency to be downregulated in BAT of Control mice on HFD. When analysing the same panel of genes in H19 TG mice on HFD, expression of markers tended to be slightly increased compared to Control mice, although this effect was not significant (Figure 22K). In scWAT of H19 TG and Control mice on HFD, mitochondrial fission and fusion markers were not altered compared to Control mice on CD (Figure 22L).

These results lead to the conclusion that *H19* reverses detrimental DIO-induced defects on mitochondrial morphology and biogenesis in BAT whereas effects of *H19* on fission and fusion is weaker.

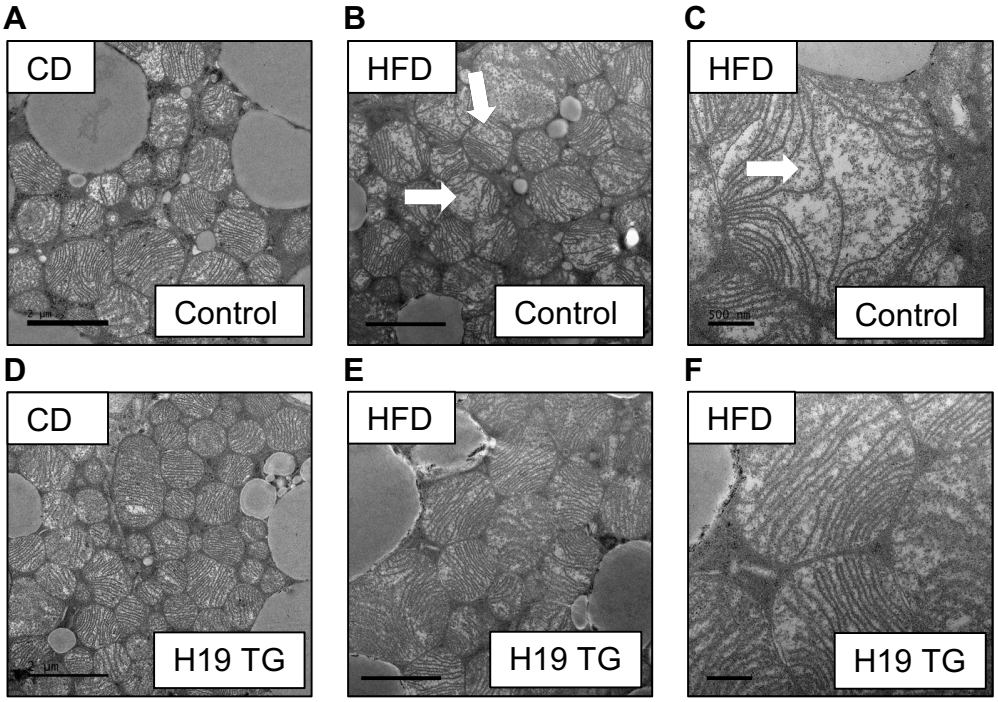

Figure 22: *H19* overexpression promotes brown adipose mitochondrial biogenesis *in vitro* and *in vivo*

(A-F) Representative EM images from BAT mitochondria across diets and genotypes. White arrows depict cristae structures. Scale bar (A, B, D, E) = 2 µm, (C, F) = 500 nM. (G) Quantification of mitochondrial perimeters (total mitochondria numbers in brackets) in BAT of indicated diets and genotypes. (H) Quantification of mitochondrial area (total mitochondria number in brackets) in BAT of indicated diets and genotypes. (G, H) Graphs represent floating bars with a line at the mean. An unpaired, two-tailed Student´s t-test was applied to assess statistical significance between genotypes. (I) Relative BAT expression of indicated mRNAs in age-matched HFD-fed H19 TG (n=3), HFD-fed Control (n=4) and CD-fed Control (n=5) male mice. (J) Relative scWAT expression of indicated mRNAs in age-matched HFD-fed H19 TG (n=3), HFD-fed Control (n=4), and CD-fed Control (n=5) male mice. (I, J) Transcript levels of mRNAs were normalized to *Hprt1* expression. Graphs represent floating bars with a line at the mean. A One-Way ANOVA plus Bonferroni *post hoc* test was applied to assess statistical significance; [(a)]= Significance versus CD-fed Control, [(b)]= Significance versus HFD-fed Control. (K) Relative BAT expression of indicated mRNAs in HFD-fed H19 TG (n=3), HFD-fed Control (n=4), and CD-fed Control (n=5) male mice. Transcript levels of mRNAs were normalized to *Hprt1* expression. Graphs represent floating bars with a line at the mean. A One-Way ANOVA test with Bonferroni *post hoc* test was applied to assess statistical significance; [(a)]= Significance versus CD-fed Control. (L) Relative scWAT expression of indicated mRNAs in HFD-fed H19 TG (n=3), HFD-fed Control (n=4), and CD-fed Control (n=5) male mice. Transcript levels of mRNAs were normalized to *Hprt1* expression. Graphs represent floating bars with a line at the mean. *p<0.05, **p<0.01, ***p<0.001. Modified after Schmidt et al. (2018)[204]. Figure continued on the next page.

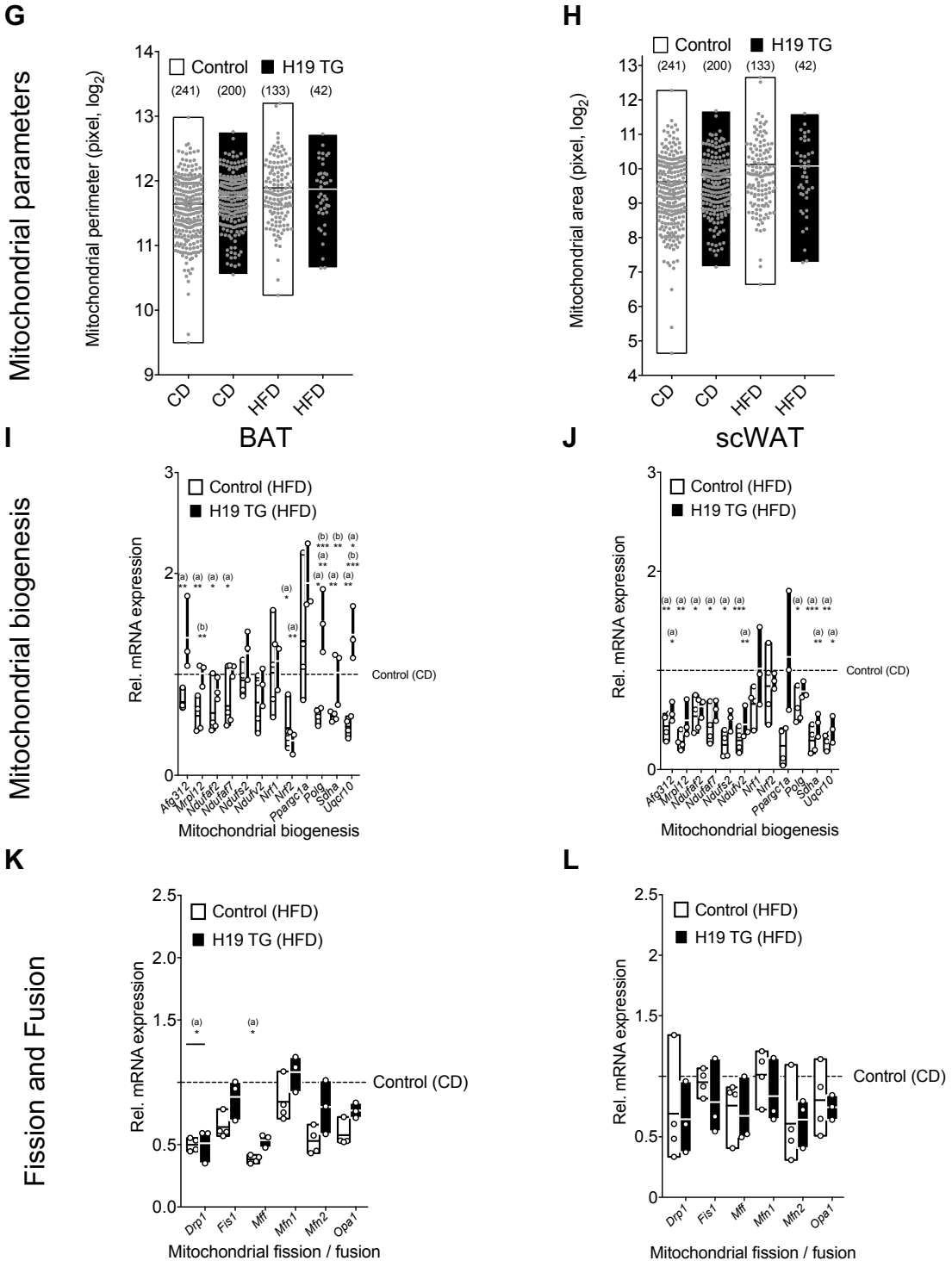
G
H
Mitochondrial parameters
Mitochondrial perimeter (pixel, log2)
Mitochondrial area (pixel, log2)
Control
H19 TG
(241) (200) (133) (42)
CD CD HFD HFD
I
J
BAT
scWAT
Mitochondrial biogenesis
Rel. mRNA expression
Control (HFD)
H19 TG (HFD)
Control (CD)
Atg312 Mrpl12 Ndufaf2 Ndufaf7 Ndufs2 Ndufv2 Nrf1 Nrf2 Ppargc1a Polg Sdha Uqcr10
K
L
Fission and Fusion
Mitochondrial fission / fusion
Drp1 Fis1 Mff Mfn1 Mfn2 Opa1

The protective effects of *H19* overexpression on BAT mitochondria spurred interest in analysing its effect on mitochondria in more detail. Consequently, we wanted to investigate whether *H19* ablation leads to an opposite effect on mitochondria in BAT of $H19^{\Delta AT}$ mice and performed EM imaging and gene expression analyses.

The experiments revealed pathological alterations in mitochondrial morphology, specifically cristae shape, of BAT in $H19^{\Delta AT}$ mice coupled with DIO (Figure 23A-D). To support these morphological findings, we analysed genes involved in mitochondrial biogenesis in BAT of $H19^{\Delta AT}$ mice and observed that *NADH dehydrogenase [ubiquinone] flavoprotein 2* (*Ndufv2*) was significantly decreased and other genes of the investigated panel were also reduced compared to BAT of Control mice (Figure 23E). In scWAT gene expression of mitochondrial biogenesis markers was unaltered (Figure 23F). The expression of fission and fusion parameters in BAT showed a decreased expression of *mitochondrial fission 1 protein* (*Fis1*) and *Mitofusin-1* (*Mfn1*) in $H19^{\Delta AT}$ mice compared to Control mice (Figure 23G). In scWAT of $H19^{\Delta AT}$ mice fission and fusion markers tended to be increased compared to Control mice, although this effect was not significant (Figure 23H).

Interestingly, cell-intrinsic defects in mitochondriogenesis occurred also in mature adipocytes from *de novo* differentiated SVFs of *H19* RNAi treated 1° BAT cells (Figure 23I) and $H19^{\Delta AT}$ mice (Figure 23J). These observations in 1° BAT adipocytes are in accordance with the expression defects observed in the same gene set seen *in vivo* with $H19^{\Delta AT}$ BAT. In addition, we used SVF isolated BAT from $H19^{\Delta AT}$ mice and differentiated them into mature adipocytes to perform Seahorse experiments. We observed a tendency towards reduced basal OCRs, which we take as measure of general mitochondrial function of brown adipocytes selective lacking *H19* in mature cells (Figure 23K).

From these results, we conclude that *H19* loss in AT causes mice to be more susceptible to DIO weight gains and leads to impairments in EE, possibly due to the control of mitochondrial dynamics by the lncRNA *H19*.

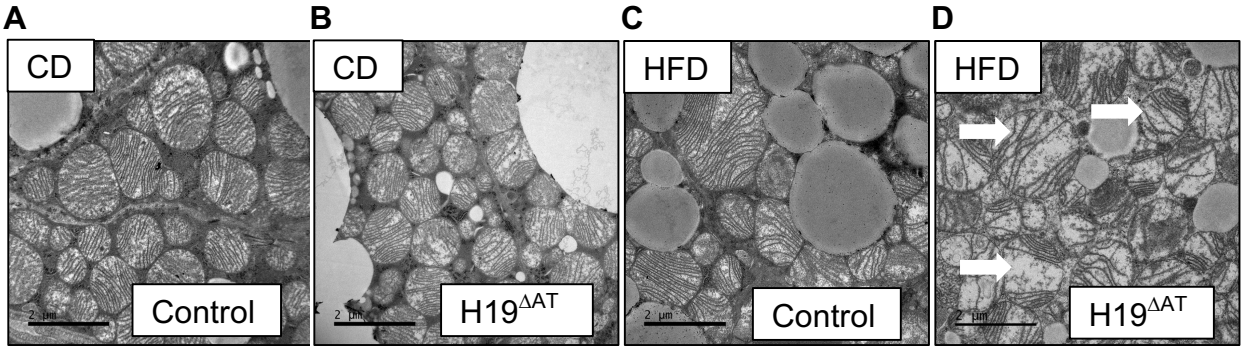

Figure 23: *H19* ablation exacerbates HFD-induced detrimental effects on mitochondrial biogenesis
(A-D) Representative EM images from BAT mitochondria across diets and genotypes. White arrows depict cristae structures. Scale bar = 2 µm. (E) Relative BAT expression of indicated mRNAs in HFD-fed Control (n=4) versus HFD-fed H19$^{\Delta AT}$ (n=3) male mice. (F) Relative scWAT expression of indicated mRNAs HFD-fed Control (n=4) versus HFD-fed H19$^{\Delta AT}$ (n=3) male mice. For (E) and (F), transcript levels of mRNAs were normalized to *Hprt1* expression. Graphs represent floating bars with a line at the mean. An unpaired, two-tailed Student´s t-test was applied to assess statistical significance between genotypes. (G) Relative BAT expression of indicated mRNAs in HFD-fed Control (n=4) versus HFD-fed H19$^{\Delta AT}$ (n=3) male mice. (H) Relative scWAT expression of indicated mRNAs in HFD-fed Control (n=4) versus HFD-fed H19$^{\Delta AT}$ (n=3) male mice. For (G) and (H), transcript levels of mRNAs were normalized to *Hprt1* expression. Graphs represent floating bars with a line at the mean. An unpaired, two-tailed Student´s t-test was applied to assess statistical significance between genotypes. (I) Relative expression of indicated mRNAs in BAT derived 1° adipocytes after transfection with 25 nM scr versus H19 LNA. (J) Relative expression of indicated mRNAs in BAT 1° adipocytes from Control versus H19$^{\Delta AT}$ mice. For (I) and (J), transcript levels of mRNAs were normalized to *Hprt1* expression. Graphs represent floating bars with a line at the mean. A paired, two-tailed Student´s t-test was applied to assess statistical significance across n=3 independent experiments performed in n=3 technical replicates each. (K) OCRs in 1° BAT from Control or H19$^{\Delta AT}$ mice. Alternating backgrounds depict injections of medium, oligomycin, FCCP and rotenone plus antimycin A. Numbers of measured wells per genotype are indicated. *p<0.05, **p<0.01. If applicable p-values are indicated within the panel. Modified after Schmidt et al. (2018)[204]. Figure continued on the next page.

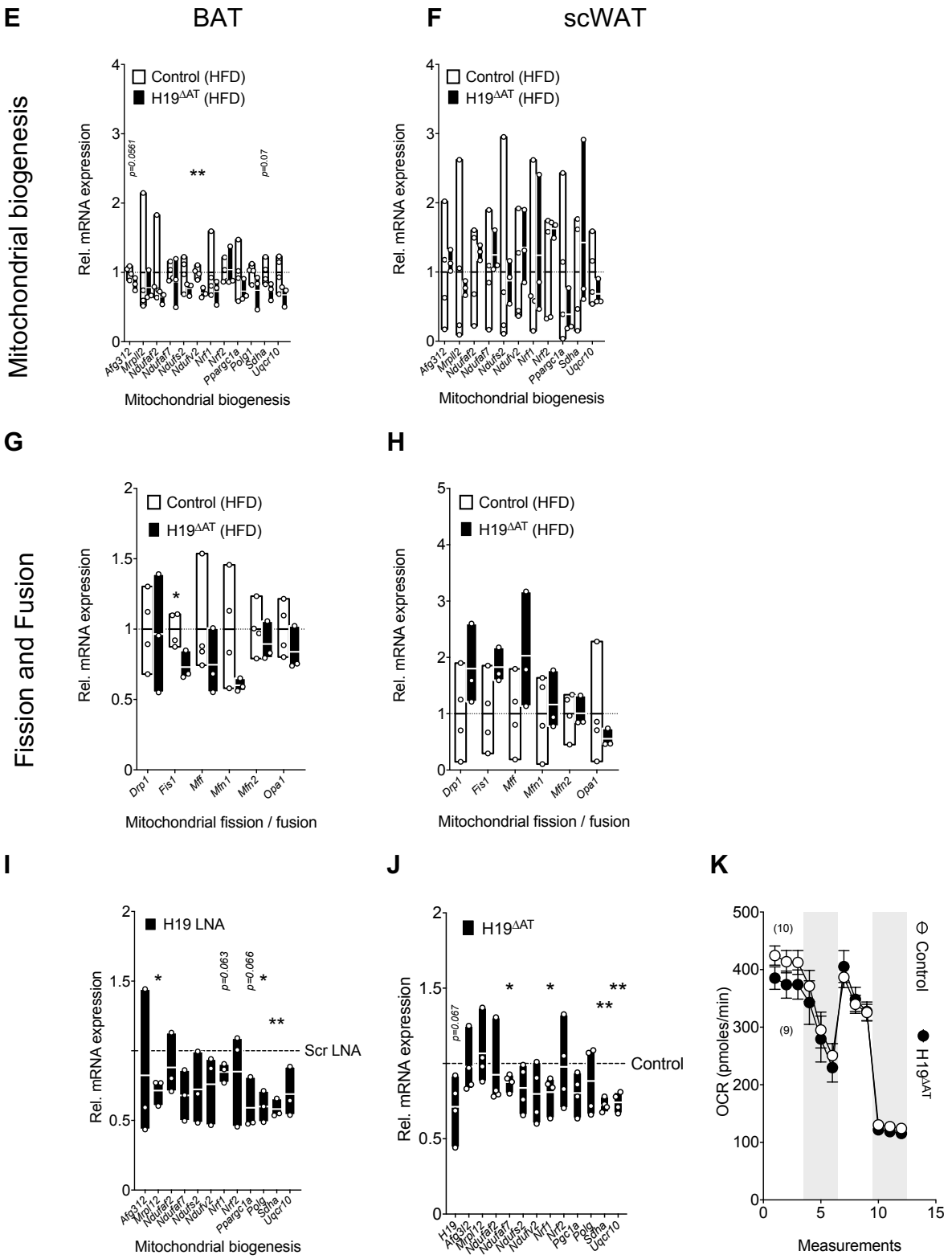
E
BAT
F
scWAT
Mitochondrial biogenesis
Control (HFD)
H19ΔAT (HFD)
Rel. mRNA expression
p=0.0561
**
p=0.07
Afg3l2
Mrpl12
Ndufaf2
Ndufaf7
Ndufs2
Ndufv2
Nrf1
Nrf2
Ppargc1a
Polg1
Sdha
Uqcr10
Mitochondrial biogenesis
G
H
Fission and Fusion
Drp1
Fis1
Mff
Mfn1
Mfn2
Opa1
Mitochondrial fission / fusion
I
J
K
H19 LNA
p=0.063
p=0.066
Scr LNA
H19ΔAT
p=0.067
Control
OCR (pmoles/min)
(10)
(9)
Measurements

3.11 BAT represents a unique case of tissue-specific imprinting and PEG loss

Mechanistically, the lncRNA *H19* is a rather well understood example of imprinted genes, which are exclusively transcribed from one parental allele[169,223]. Research has shown that *H19* belongs to an imprinted gene network (IGN) and regulates the expression of eight imprinted genes, both maternally and paternally expressed, within this cluster[224].

Based on the BAT-selectivity of *H19* and its novel role in the regulation of brown adipocyte differentiation and function, we were interested in the transcriptome-wide expression of paternally expressed genes (PEGs) and maternally expressed genes (MEGs) across fat depots. RNA-Seq from C57BL/6 N mice revealed no differences in MEGs abundances between BAT, scWAT or vWAT (Figure 24A, B). However, seven fat-abundant protein-coding genes (such as *G Protein Coupled Receptor 1* (*Gpr1*), *Insulin Like Growth factor 2* (*Igf2*), *Mesoderm Specific Transcript* (*Mest*), *Neuronatin* (*Nnat*), *Paternally Expressed 3* and *10* (*Peg3*, *Peg10*) and *Plagl1 Like Zinc Finger 1* (*Plagl1*) and three microRNA PEGs (*miR-184*, *miR-298* and *miR-335*)) and many others were absent from BAT yet robustly expressed in scWAT and vWAT (Figure 24C-E).

From this result, we conclude that MEGs are equally distributed between adipose tissues, whereas PEGs are mainly absent from BAT but enriched in WAT.

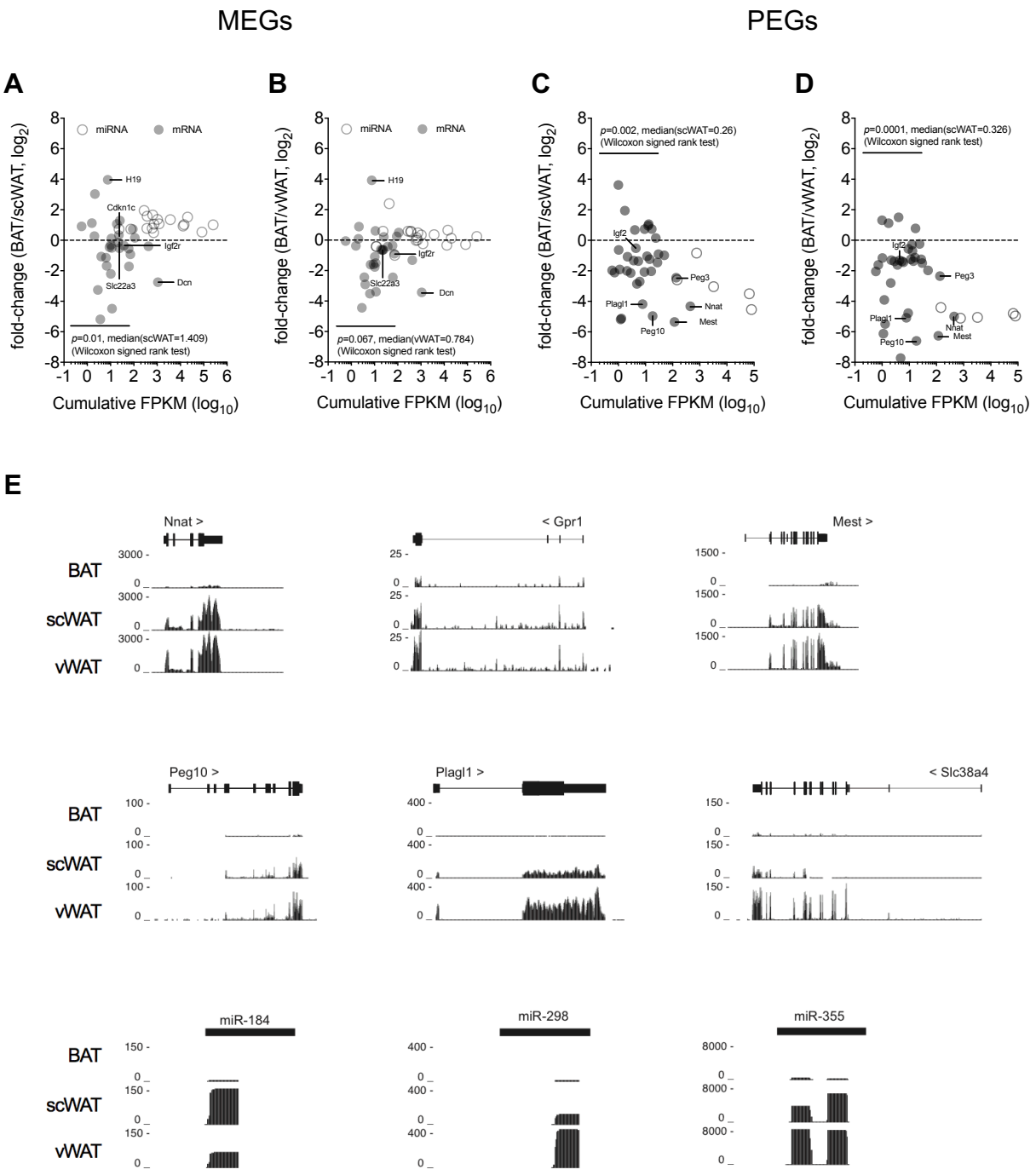

Figure 24: Repression of paternal monoallelic gene expression in BAT
(A, B) Plot of expression fold-changes of maternally expressed genes (MEGs) in BAT versus (A) scWAT and (B) vWAT. (C, D) Plot of expression fold-changes of paternally expressed genes (PEGs) between BAT versus (C) scWAT and (D) vWAT. A Wilcoxon matched-pairs signed rank test was used to assess statistical significance for up- or downregulation of PEGs/MEGs. (E) UCSC Genome Browser illustration of PEG abundances in BAT, scWAT, and vWAT. If applicable p-values are indicated within the panel. Modified after Schmidt et al. (2018)[204].

3.12 *H19* recruits MBD1 chromatin modifier in mature BAT

As expression of *H19* was not altered during BAT, scWAT, and vWAT differentiation (Figure 25), we next wanted to discern if *H19* interacts with specific protein interactors to repress PEGs in brown adipocytes.

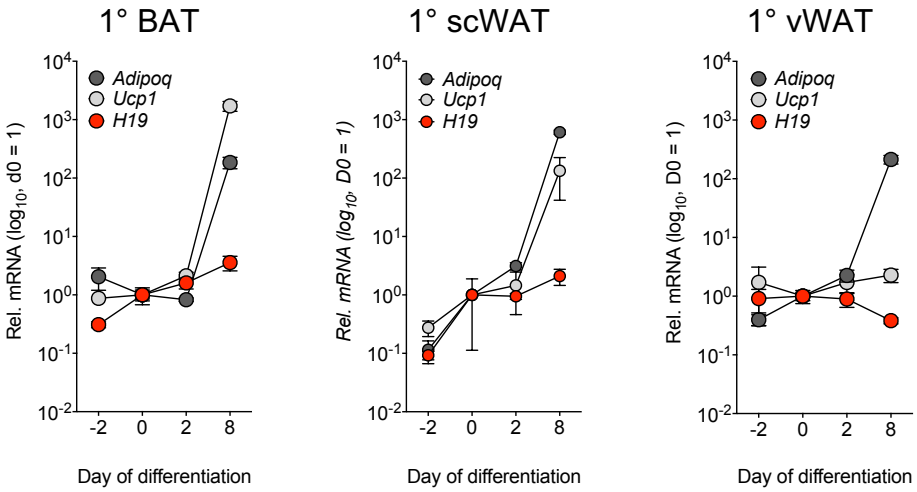

Figure 25: Timecourse of *AdipoQ, H19* and *Ucp1* expression in 1° adipocytes during differentiation
Relative expression of indicated mRNAs in 1° BAT, scWAT, and vWAT adipocytes during the course of differentiation. Transcript levels of mRNAs were normalized to *Hprt1* expression. Data represent one experiment, performed in n=3 technical replicates. Modified after Schmidt et al. (2018)[204].

To investigate this, we performed **C**apture **H**ybridisation **A**nalysis of **R**NA **T**argets[225] coupled to mass spectrometry (CHART-MS) from confluent and differentiated PIBA cells. ChART is a technique that uses complementary oligonucleotides to purify an RNA with its associated proteins from formaldehyde cross-linked chromatin (more details on this technique can be found in chapter 2.8). In total 3,590 proteins that were associated with *H19* were detected by MS. Of those proteins, 168 were enriched in *H19* antisense, not sense, oligonucleotide co-immunoprecipitation samples. 76 proteins were bound to *H19* in confluent and 54 proteins in differentiated cells, whereas 38 proteins were bound to *H19* in both conditions (Figure 26A). Next, we performed Ingenuity Pathway Analysis (IPA) to construct a *H19*-protein interactome comprised of 61 proteins (Figure 26C). IPA is an analysis and search tool with which interaction network analyses can be performed to explore, among other options, RNA-protein networks. When performing gene ontology (GO) analyses using Ami Gene Ontology 2 (AMIGO2), a multiplatform software tool for browsing the Gene Ontology database[226], we could see that in immature BAT *H19* mainly recruited proteins annotated as 'RNA-binding proteins' (RBPs, e.g. *H19* interactors like *Insulin Like Growth Factor 2 Binding Protein 3* (*IGFBP3*))

whereas in differentiated cells *H19* primarily recruited proteins classified as 'chromatin binders' or 'chromatin modifiers' (Figure 26B). The protein DNA methyltransferase MBD1 (and its homologue MECP2) was found to only bind to *H19* in differentiated PIBA cells.

From this result, we conclude that *H19* interacts with proteins to fulfil its function in BAT and might even recruit the chromatin modifier MBD1 during BAT differentiation to suppress PEGs in BAT.

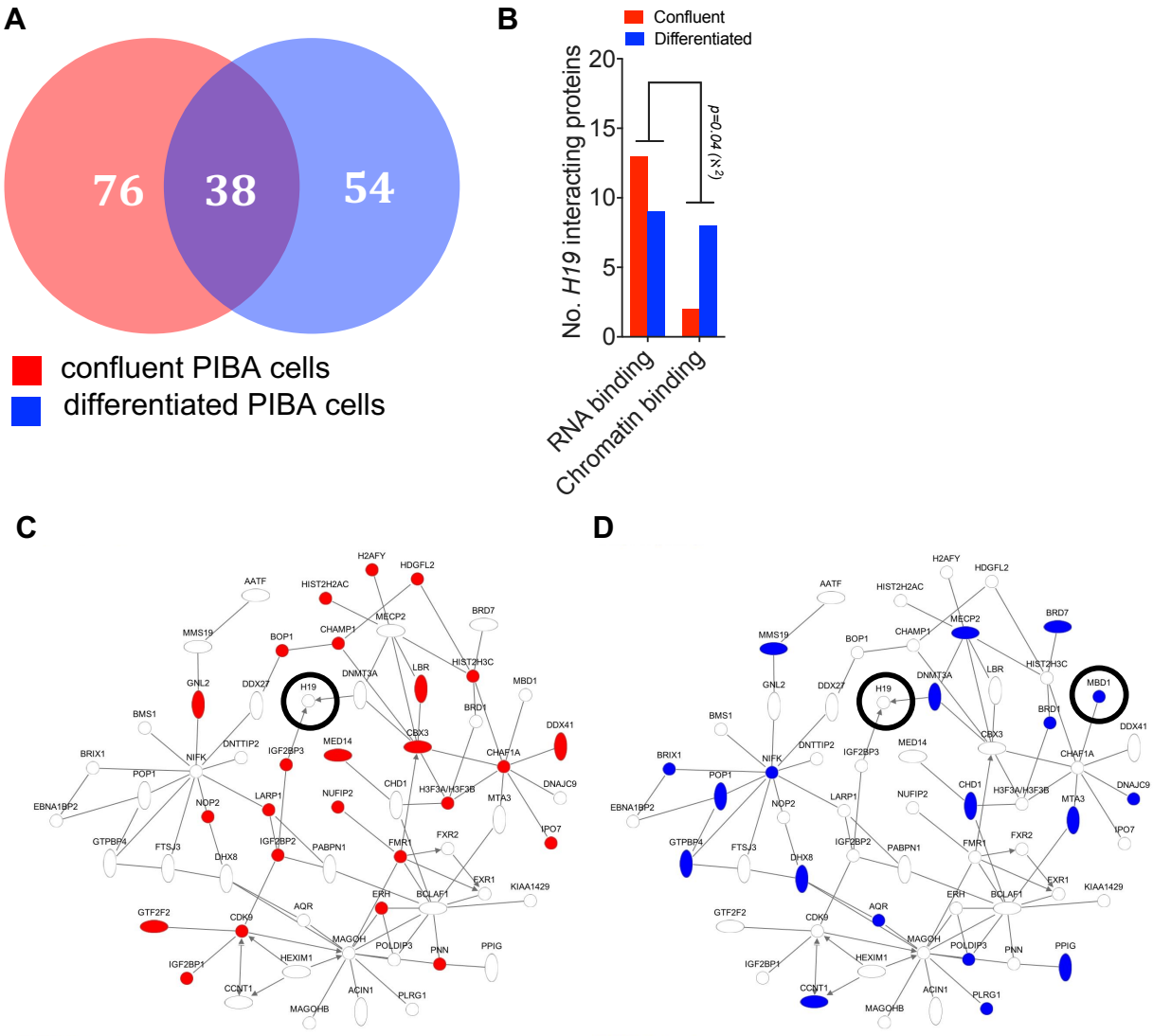

Figure 26: ChART-MS reveals *H19*-associated proteins in confluent and differentiated PIBA cells
(A) Quantification and overlap of *H19*-associated proteins in confluent (red) and differentiated (blue) PIBA cells determined by ChART-MS. Pulldown of *H19*-interacting proteins was performed using pools of six *H19*-specific antisense/sense oligonucleotides in n=3 replicates. (B) AMIGO2 GO classification of *H19* interactors across cellular states. (C, D) Illustration of *H19* protein interaction network comprising n=61 proteins generated using Ingenuity Pathway Analysis (IPA). Red and blue nodes depict proteins co-immunoprecipitating in confluent and differentiated cells, respectively. Modified after Schmidt et al. (2018)[204].

3.13 Fat tissue human *H19* (*hH19*) is reduced in obese humans and correlates positively with browning markers

H19 is strongly conserved at the transcript level[227]. Therefore, we next wanted to decipher if *hH19* is also affected by obesity and T2DM in humans. We henceforth quantified *hH19* abundances in scWAT (Table 6) and vWAT (Table 7) biopsies from 169 lean and obese patients and observed that *hH19* expression decreased with increasing BMIs in both adipose depots. Moreover, *hH19* correlated positively with markers of adipose 'beiging' like *UCP1* mRNA levels.

Therefore, we conclude that *hH19* can support EE and acquisition of catabolic expression profiles in human fat.

Table 6: Correlation of human scWAT *H19* with obesity cohort patient characteristics, serum parameters and gene markers of adipose tissue browning.
Data were obtained from a human study and provided by Prof. Matthias Blüher.

sc_H19 [AU] vs	*All*	*n*	*Mean (95% CI)*	*Rho*	*p-Value*	*w/o T2D*	*n*	*Mean (95% CI)*	*Rho*	*p-Value*
CIDEA [AU]		163	2.438 (2.026-2.85)	0.01288	0.8704		**80**	**3.161 (2.481-3.841)**	**0.1873**	**0.0963[#]**
PRDM16 AU]		164	2.254 (1.917-2.592)	-0.04605	0.5582		80	2.415 (1.876-2.953)	0.07682	0.4982
UCP1 [AU]		**61**	**1.486 (0.9696-2.002)**	**0.4615**	**0.0002[C]**		**33**	**1.831 (1.003-2.659)**	**0.535**	**0.0013**
BMI		**169**	**44.14 (42.21-46.07)**	**-0.1359**	**0.0781[#]**		**82**	**38.9 (36.02-41.97)**	**-0.2745**	**0.0126**
Creatinin [µmol/l]		168	76.17 (72.01-80.32)	-0.02076	0.7894		81	70.88 (67.33-74.43)	-0.09806	0.3838
CrP [mg/l]		168	11.84 (9.376-14.31)	-0.02313	0.766		81	11.53 (7.551-15.5)	-0.06706	0.5519
FPG [mmol/l]		158	6.725 (6.266-7.183)	-0.06038	0.451		**74**	**5.395 (5.161-5.629)**	**-0.2118**	**0.0701[#]**
Leucocyte		166	7.957 (7.469-8.445)	0.06575	0.4		80	8.044 (7.183-8.905)	0.04563	0.6877
ALAT [µkat/l]		164	0.5891 (0.5306-0.6476)	-0.07846	0.318		79	0.562 (0.49-0.633)	-0.1768	0.119
ASAT [µkat/l]		158	0.4839 (0.4535-0.7074)	0.01569	0.8449		77	0.459 (0.414-0.505)	-0.01391	0.9045
gGT [µkat/l]		163	0.8485 (0.7074-0.9896)	0.04341	0.5822		78	0.826 (0.595-1.056)	-0.004883	0.9662
TSH [mU/l]		144	1.554 (1.387-1.721)	-0.1279	0.1267		**71**	**1.523 (1.27-1.775)**	**-0.2558**	**0.0313[A]**

Table 7: Correlation of human vWAT *H19* with obesity cohort patient characteristics, serum parameters and gene markers of adipose tissue browning.
Data were obtained from a human study and provided by Prof. Matthias Blüher.

visc_H19[AU] vs	*All*	*n*	*Mean (95% CI)*	*Rho*	*p-Value*	*w/o T2D*	*n*	*Mean (95% CI)*	*Rho*	*p-Value*
CIDEA [AU]		165	2.429 (2.004-2.854)	-0.01972	0.8015		80	3.09 (2.355-3.825)	0.05031	0.6576
PRDM16 AU]		165	2.951 (2.419-3.484)	-0.0285	0.7163		81	3.899 (2.936-4.863)	-0.0172	0.8789
UCP1 [AU]		113	2.925 (1.683-4.167)	0.1075	0.2571		**57**	**4.172 (1.834-6.509)**	**0.2804**	**0.0347[A]**
BMI		**169**	**44.14 (42.21-46.07)**	**-0.2549**	**0.0008[C]**		**82**	**38.9 (36.02-41.97)**	**-0.3144**	**0.004[B]**
Creatinin [µmol/l]		168	76.17 (72.01-80.32)	0.01963	0.8006		81	70.88 (67.33-74.43)	0.02555	0.8209
CrP [mg/l]		168	11.84 (9.376-14.31)	-0.05255	0.4988		81	11.53 (7.551-15.5)	-0.08711	0.4394
FPG [mmol/l]		158	6.725 (6.266-7.183)	-0.1038	0.1945		74	5.395 (5.161-5.629)	-0.08031	0.4964
Leucocyte		166	7.957 (7.469-8.445)	0.02613	0.7383		80	8.044 (7.183-8.905)	-0.01946	0.864
ALAT [µkat/l]		164	0.5891 (0.5306-0.6476)	-0.1263	0.1071		79	0.562 (0.49-0.633)	-0.1552	0.1721
ASAT [µkat/l]		158	0.4839 (0.4535-0.7074)	0.0002603	0.9974		77	0.459 (0.414-0.505)	0.06409	0.5798
gGT [µkat/l]		163	0.8485 (0.7074-0.9896)	-0.1104	0.1606		78	0.826 (0.595-1.056)	-0.09666	0.3999
TSH [mU/l]		144	1.554 (1.387-1.721)	-0.08148	0.3316		71	1.523 (1.27-1.775)	-0.09212	0.4448

4 Discussion

Obesity is a serious medical and social problem all over the world that results from chronic imbalances between energy intake and expenditure. If untreated obesity can lead to life-threatening diseases such as type 2 diabetes mellitus. For counteracting obesity and related metabolic disorders, activation of BAT thermogenesis has moved into focus for therapeutic purposes due to its unique capacity for dissipating energy as heat through the unique action of UCP1-mediated chemical uncoupling. Because of BAT´s beneficial effects on body metabolism, understanding and harnessing the molecular circuits activating BAT function is of great interest. Several protein-coding genes, mRNAs, and miRNAs have been identified that play a role in adipocyte development. LncRNAs, however, a class of RNAs that have been identified only recently, are not well understood but have received a lot of attention due to their broad involvement in different physiological processes and their tissue-specific character which stresses their high potential as drug target.

In this study, we identified the maternally expressed lncRNA *H19* as a novel regulator of BAT differentiation and function. *H19* protects from dietary obesity by controlling mitochondrial biogenesis in mature adipocytes and interacts with MBD1 which potentially results in maintenance of quiescence of obesity-predisposing PEGs in BAT. The findings discussed in this thesis have implications both for the understanding of how monoallelic gene expression affects metabolism in rodents and, potentially, in humans but also for finding new treatment possibilities via the manipulation of *H19* expression in BAT.

4.1 Maternally expressed lncRNA *H19* regulates BAT differentiation and function independent of imprinting gene cluster *in vitro*

For the identification of lncRNAs correlating with BAT function, total RNA-Seq in BAT (as well as in cold-evoked subcutaneous white adipose tissue) was conducted. This screening approach is in accordance with several recently published studies in which different whole genome sequencing techniques were applied and resulted in the identification of regulators of adipogenesis[108,120,228]. Whilst some of them focused on adipogenesis in general, including WAT, in our study, we exclusively searched for lncRNAs regulating BAT homeostasis. At the moment, a variety of sequencing

approaches to identify lncRNAs are available and applied by the experimenter's demands[229]. In our study, we performed total RNA-Seq as it broadly identifies not only coding but also multiple forms of noncoding RNAs[230]. Additionally, the sequencing technique can accurately measure the abundance of genes and transcripts based on which known and novel features of the transcriptome can be defined. This gave us the possibility to find and finally characterize novel lncRNA candidates that are associated with BAT.

After applying a stringent filter to the found candidates, we decided to begin with the characterization of the following lncRNA candidates: *1700007L15Rik*, *2500002B13Rik*, *Gm12319,* and *H19.* All candidates showed increased expression upon cold-mediated BAT activation and were decreased upon chronic diet-induced obesity (DIO) BAT dysfunction. While *1700007L15Rik*, *2500002B13Rik* and *Gm12319* are all transcripts with unknown function, the lncRNA *H19* is widely studied and one of the best researched imprinting genes.

For further functional characterization, we investigated the effect of lncRNA candidate ablation on adipogenesis by performing locked nucleic acid (LNA)-mediated RNA interference (RNAi) in SVF adipocyte precursor cells isolated from three major adipose depots (BAT, scWAT, and vWAT). With this, we could show that the lack of both *2500002B13Rik* and *H19* expression led to a decrease in lipid accrual and a proper expression of browning markers, whereas we did not observe these differences for lncRNAs *1700007L15Rik* or *Gm12319*.

Antisense oligonucleotides (ASOs) or LNA GapmeRs, used for RNAi experiments in this study, have gained recognition as therapeutic tools[231]. Many are in advanced clinical trials as oligonucleotide drug candidates or even approved by the FDA, such as mipomersen (trade name Kynamro) which targets apolipoprotein B (apoB) and is used for homozygous familial hypercholesterolemia (HoFH)[232]. With the use of ASOs in the laboratory there are still safety and technical limitations such as affinity to unintended targets with partial sequence complementarity which might lead to hybridization-dependent off-target effects (OTEs)[233]. The risks for OTEs are not yet fully investigated, and thus RNAi experiments *ex vivo* were performed with two different LNA GapmeRs to exclude that effects seen stem from OTEs.

Of all four candidates, *H19* revealed the most pronounced effects on adipogenesis. This outcome and its BAT-selective expression and sequence conservation among eutherians led to the decision to only focus on the characterization of *H19* in BAT

homeostasis. The current research has shown that *H19* is abundantly expressed maternally in embryonic tissues, decreases after birth, and its transcription persists only in skeletal muscle[173] and liver[234]. Additionally, in our study, we could for the first time show that *H19* expression also remained high in BAT after birth. BAT and skeletal muscle both originate from a mesodermal progenitor population in the somites. With that, they are sharing the same origins, and thus are closely related in their development[66]. Different studies have investigated the involvement of *H19* and its encoded *miR-675* in muscle differentiation and regeneration[173,235] and have demonstrated that *H19* contributes to glucose metabolism in muscle cells[197]. Yet, how *H19* affects BAT homeostasis after birth has not been studied until now.

To find out more about what led to the defect in proper adipogenesis we analysed BAT progenitor expression to see whether cells that lacked *H19* expression stayed in a progenitor-like state, and thus were unable to continue in the differentiation process. One example of a preadipocyte marker that is known to be mostly expressed in preadipocytes and declines with brown adipocyte differentiation is *Delta Like Non-Canonical Notch Ligand 1* (*Dlk1*)[211]. When analyzing the expression of *Dlk1* and additional preadipocyte markers after *H19* ablation we observed that only in BAT and not in scWAT and vWAT the expression of various progenitors remained high, showing that *H19* is indeed required for the commitment of BAT but not scWAT or vWAT-derived progenitors.

Two early progenitor genes we found significantly expressed in BAT cells are *Runx2* and *Pdgfra*. *Runx2* is an osteogenic transcription factor that is required for osteogenic differentiation[236]. Adipocytes and osteoblasts both stem from mesenchymal stem cells, a non-hematopoietic stem cell population which was first discovered in bone marrow. The differentiation commitment for both cell types is tightly regulated and several *in vitro* studies have demonstrated that fat-induction factors inhibit osteogenesis and at the same time bone-induction factors prevent adipogenesis[237]. Thus, the failure in repression of *Runx2* in mature brown adipocytes upon *H19* loss might hint to a defect in the adipo-osteogenic balance as shown recently[237–239].

Pdgfra is a receptor located on the surface of different cell types and is involved in cell signaling pathways leading to cellular growth and differentiation. Normally, it is used as a marker for fibroblasts and undifferentiated mesenchymal cells and not expressed in mature adipocytes[240]. Moreover, *Pdgfra* has been shown to regulate the balance of stromal and adipogenic cells during AT organogenesis. An increased activity

of *Pdgfra* has been shown to cause AT fibrosis in adult mice[240]. This shows that proper functioning of *H19* expression is necessary to prevent the development of diseased tissue.

Next, we aimed to dissect the cell intrinsic and metaboregulatory properties of *H19* using Seahorse technology. *H19* RNAi impaired oxidative metabolism and uncoupling in differentiated brown adipocytes. Experiments with 1° BAT of *H19* overexpression mice, performed by a Master student from the lab and not included in this PhD thesis, showed improved oxidative metabolism, uncoupling, and extracellular acidification rates (ECAR) in differentiated brown adipocytes. These experiments demonstrated that *H19* supports adipocyte differentiation and thermogenic gene expression, oxidative metabolism, and mitochondrial dynamics in mature adipocytes in a BAT-specific manner and gave a first hint that *H19* is not only involved in the process of adipogenesis but also in the function of BAT.

H19 has been reported to reside in nuclear, but also cytoplasmic and ribosomal fractions in various cell types[186,213,214]. In the nucleus, it has been shown to interact with chromatin-modifying complexes such as methyl-CpG-binding domain protein 1 (MBD1) to control gene expression of the imprinting gene network (IGN)[190] or serve as a microRNA precursor for *miR-675-3p* and *miR-675-5p*[241,242]. In the cytoplasm it can control myogenic differentiation by binding to RNA binding proteins[243] or it can act as a molecular sponge for miRNA *let-7*[127,197]. When analyzing *H19* localization in 1° BAT cells, we could show that *H19* is located in nuclear and cytoplasmic compartments of brown adipocytes pointing to the fact that *H19* fulfills different actions in different compartments of the cell. As LNA-mediated RNAi acts via RNAse H-mediated transcript decay predominantly in nuclei, we also targeted *H19* using siRNAs, which act preferentially in the cytoplasm. *H19* loss was observed across all subcellular compartments using both techniques and led to equal results.

Historically, *H19* was discovered as monoallelically expressed gene in which solely maternal alleles express *H19* in an epigenetic process termed 'genomic imprinting'. In the *H19-Igf2* imprinted gene cluster the reciprocally regulation critically depends on the enhancer-blocking properties of CCCTC-Binding Factor (Ctcf) proteins[155,169]. As no effects on BAT adipogenesis occurred after *Ctcf* RNAi and as *Ctcf* and *Igf2* BAT levels were unchanged by DIO or cold, we concluded that cold/DIO-evoked alterations in *H19* are not secondary to altered *H19-Igf2* imprinting. This is in

accordance with earlier reports on reduced *H19* expression independent from traditional *H19-Igf2* imprinting control[244].

Moreover, the *H19*-encoded microRNA *miR-675* was not expressed in BAT, arguing against the involvement of *miR-675* in brown adipocyte differentiation as observed for myogenic lineage determination[173].

Collectively, we showed that the conserved lncRNA *H19* promoted brown adipocyte differentiation and function *in vitro* and *in vivo* independently of the imprinting gene cluster.

4.2 *H19* regulates BAT function via regulating mitochondrial biogenesis

Defects in BAT differentiation and function as well as concomitant impairments in EE render mice susceptible to DIO-induced weight gain and the development of metabolic diseases[217–219]. In a study by Ellis et al. (2013) it has been shown that gene expression of lncRNA *CRNDE* was affected by the anabolic master regulator insulin and insulin-like growth factor 1 (IGF1) signaling, pointing for the first time to the fact that lncRNAs might be implicated in the metabolic effects of insulin and the development of insulin resistance[138].

To analyze whether *H19* is involved in glucose metabolism in mice, we performed gain-and loss-of function studies of *H19* in mice. We exposed *H19* gain-of-function mice[210] and Controls to HFD and CD. *H19* overexpression strongly prevented DIO-mediated weight gains and improved insulin sensitivity whereas glucose tolerance was decreased. This unexpected result is in accordance with a study by Zhang et al. (2018) who showed that elevated hepatic expression of *H19* promoted hepatic glucose production and insulin resistance[220]. Furthermore, we observed an increase in EE. This rise in energy catabolism tended towards prevention of DIO-induced increases in scWAT and vWAT adiposity and prevented the 'whitening' of BAT. In lean mice *H19* overexpression elicited little changes showing that counteracting the HFD-induced *H19* decline is beneficial during DIO, but does not cause detrimental effects in lean mice.

To show that the effects of *H19* overexpression on energy metabolism are due to *H19* induced alteration in BAT function and not due to other tissues, experiments at thermoneutrality could be performed to assess changes upon conditions in which BAT activity is low. In general, thermoneutrality is important because people tend to live at thermoneutral conditions with the aid of clothing and heating whereas for mice Rtemp

is not thermoneutral and they need to spend extra energy to uphold their body temperature[49]. However, in our experiments the exposure to thermal stress was a performed experimental approach for physiologically relevant BAT activation. We housed H19 TG and H19$^{\Delta AT}$ mice at 4°C for 4 days, a condition in which mice expend 60% of their energy for thermoregulation through BAT non-shivering thermogenesis (NST)[245,246]. Muscle shivering thermogenesis (ST) can be seen only in the early phases, for several hours, of cold adaptation[247] and should not significantly contribute to EE afterwards. As we observed elevated Ees in cold-exposed H19 TG mice beyond the point of muscle ST but also, crucially, in H19$^{\Delta AT}$ where *H19* is ablated only in mature adipose tissue, we could demonstrate an (B)AT-specific effect of altered *H19* levels *in vivo*.

H19 TG mice ubiquitously overexpress *H19*. To ablate *H19* specifically in AT, we crossed female mice harbouring loxP-flanked *H19* methylation-sensitive ICRs with male *Adipoq-cre* expressing animals. *Adipoq-cre* mice harbour the *Adipoq-cre* BAC transgene and express Cre recombinase under control of the mouse *adiponectin* (*Adipoq*) promoter/enhancer regions within the BAC transgene. Thus, *Adipoq-cre* transgenic mice delete floxed sequences in WAT and BAT. Since *H19* remains expressed in adult BAT, the H19$^{\Delta AT}$ knockout mice provide an interesting model to study the role of this gene in the adult. Surprisingly, we did not observe a knockdown or deletion of *H19* in other AT like scWAT or vWAT which could come from undetectable expression levels of *H19* in both tissues. This made the H19$^{\Delta AT}$ mouse model interesting to exclusively analyse *H19* function in BAT.

H19$^{\Delta AT}$ knockout mice gained more weight compared to Control mice on a HFD, whereas alterations in insulin sensitivity and glucose tolerance were negligible. BAT-specific *H19* loss decreased EE and oxygen consumption on both diets suggesting a decrease in BAT function. *Adipoq-cre* is not active in adipocyte progenitors, and thus results can only be ascribed to mature adipocytes. To specifically ask whether *H19*`s effect on metabolism/EE runs via alteration of brown adipogenesis, one would need to ablate *H19* or the *H19* DMD using adipocyte progenitor recombinases, examples are *Pdgfrα-Cre* or *Prx1-Cre*. Unfortunately, both recombinases are not useful for studies of brown preadipocytes as *Pdgfrα-Cre* deletes also in muscle stem cell progenitors and liver[248] and *Prx1-Cre* expression is confined to subcutaneous adipocyte precursors[249]. Apart from adipocyte progenitor recombinases, one could also use *Ucp1-Cre* to specifically ablate *H19* in interscapular BAT at ambient temperatures and after 6 days of cold exposure in inguinal and epididymal WAT. The results from this mouse model

would give more insight about the function of *H19* in beige adipocytes about which we received only little information in our study.

The difference in EE spurred the analysis of mitochondrial constitution in BAT of *H19* gain- and loss-of-function mice. Cold-induced adaptive thermogenesis and the turnover of nutrients require active mitochondrial biogenesis and rearrangements of mitochondrial networks via fission and fusion. While studying mitochondrial morphologies using EM we observed perturbed cristae formation in Control mice on HFD. This effect was diminished in H19 TG mice on HFD. When we analysed the cristae formation in $H19^{\Delta AT}$ mice compared with Control mice, both fed a HFD, we observed that the deformation of cristae structure was worsened in mice lacking *H19* in BAT compared to Control mice.

Cristae are functional dynamic compartments whose shape is maintained by the cooperation of mitochondrial-shaping proteins such as Mfn1 and 2, Optic Atrophy 1 (Opa1), as well as the cytosolic Drp1 and its receptor which is located on the outer mitochondrial membrane Fis1[250]. Perturbations of mitochondrial-shaping proteins disrupt cristae shape and influence the structure of the oxidative phosphorylation system, thereby impairing cellular metabolism and growth[251]. When analysing mitochondrial fission and fusion markers in H19 TG BAT, we observed a trend that all markers in Control mice on HFD compared to Control mice on CD were decreased among which *Drp1* and *Mff* were significantly decreased. When analysing the same set of genes in H19 TG mice fed a HFD markers showed a tendency to be increased compared to Control mice fed a HFD pointing to a rescue of diminished gene expression of fission and fusion markers upon gain of *H19* expression. The expression of this set of markers in BAT of $H19^{\Delta AT}$ mice revealed that, specifically upon *H19* loss, markers decreased in expression and for *Fis1* the effect was significant. Thus, the gene expression of mitochondrial-shaping proteins reflected cristae morphology. In scWAT of both mouse lines the expression of fission and fusions markers was unchanged.

The expression of genes involved in mitochondrial biogenesis was blunted in obese BAT, but *H19* overexpression reversed these DIO-evoked defects in gene expression in BAT but not scWAT. $H19^{\Delta AT}$ mice showed less pronounced reductions of the same gene set in BAT yet not scWAT. The rescue in H19 TG mice was especially strong for *mitochondrial ribosomal protein MRPL12* (*Mrpl12*)*, DNA polymerase subunit gamma* (*Polg*), *succinate dehydrogenase* (*Sdha*), and *Ubiquinol-cytochrome c reductase complex* (*Uqcr10*). When analysing mitochondrial biogenesis markers in 1° BAT cells

treated with *H19* RNAi we observed a significant downregulation of various markers whereas *Mrpl12*, *Polg* and *Sdha* were significantly decreased and *Pgc1a* and *nuclear respiratory factor 1* (*Nrf1*) showed a tendency to be decreased. When investigating the same set of genes in 1° BAT cells isolated from $H19^{\Delta AT}$ we could see that the genes *NADH:Ubiquinone Oxidoreductase Complex Assembly Factor 7* (*Ndufaf7*), *Uqcr10,* and *Nrf1* as well as *Sdha*, already observed partly in isolated BAT tissue and in H19 LNA treated cells, were significantly downregulated.

The product of *Mrpl12* is a protein of the mitochondrial ribosome and helps in protein synthesis[252,253]. POLG is a catalytic subunit of the mitochondrial DNA polymerase[254]. SDHA is the major catalytic subunit of succinate-ubiquinone oxidoreductase of complex II and participates in both the citric acid cycle and the respiratory chain[255]. NRF1 is a transcription factor that activates the transcription of some key metabolic genes required for respiration and mitochondrial DNA transcription and replication[256]. NDUFAF7 is an assembly factor protein and methyltransferase which helps in the assembly and stabilization of complex I[257] and the gene product of *Uqcr10* is a subunit of the respiratory chain protein ubiquinol cytochrome c reductase (Complex III)[258].

The above-described deregulation of genes involved in oxidative phosphorylation shows that *H19* loss leads to a global defect in the functions of mitochondria in BAT whereas gain of *H19* function was partially able to diminish this effect. This defect in oxidative phosphorylation could result also in defects in EE and explain why the mice are more susceptible to DIO weight gains.

4.3 *H19* interacts with MBD1 to repress genes of the imprinting gene network

Expression levels of *H19* were not altered during BAT, scWAT, and vWAT differentiation. Therefore, we asked whether specific protein interactors of *H19* control its function selectively in brown adipocytes. The interaction of *H19* with different factors such as transcriptional repressors (MBD1)[259], RNA binding proteins (K homology-type splicing regulatory protein (KSPR))[243], miRNAs (*miR-17-5p*) [260], chromatin modifiers (MBD1)[190], and enzymes (S-adenosylhomocysteine hydrolase (SAHH))[261] has been shown recently.

In order to address our question, we conducted Capture Hybridization Analysis of RNA Targets coupled to mass spectrometry (CHART-MS) with confluent and

differentiated PIBA cells. The construction of an interconnected *H19* binding protein network using Ingenuity Pathway Analysis (IPA) led to the identification of 61 interesting proteins. Gene ontology analysis showed that in immature brown adipocytes *H19* mostly recruited proteins annotated as 'RNA-binding proteins' and, in differentiated cells, *H19* preferentially associated with proteins classified as 'chromatin binders' or 'chromatin modifiers'. We specifically searched for a protein which was only bound by *H19* in differentiated cells and found the DNA methyltransferase MBD1 (and its homologue MECP2).

MBD1 belongs to a group of methyl-CpG-binding proteins that are epigenetic 'readers' by connecting DNA methylation to the regulation of transcription[262]. *H19* is part of an IGN and controls the expression of other eight imprinted genes within this network: *IGF2, SLC38A4, DCN, DLK1, PEG1, GTL2, CDKN1C* and *IGF2R*. All genes are known regulators of embryonic growth in mouse and human[224]. The interaction of *H19* with MBD1 as a physical and functional partner has already been shown previously in a paper by Monnier et al. (2013) which demonstrated that the *H19*-MBD1 complex is required for the control of several genes of the IGN[190]. Specifically, they showed that *H19*-MBD1 complexes affect histone 3 lysine methyltransferases (KMT) dependent deposition of repressive H3K27 trimethylation marks. *H19* or MBD1 loss both resulted in reduced H3K9me3, and thus de-repression at PEG loci like *Igf2*, *Solute Carrier Family 38 Member 4* (*Slc38a4*), and *Mest/Paternally Expressed 1* (*Peg1*)[190]. In light of these results, we suggest that *H19*-mediated alterations of IGNs constitute an important regulatory layer of BAT development and function, by influencing cell-intrinsic control of mitochondrial biogenesis in mature brown adipocytes, according to which PEGs have a negative effect on brown fat (*Dlk1*, *Peg1*, *Ndn*, paternally expressed GNAS isoform *XLαs*) whereas MEGs (*Gαs*) have a positive effect on BAT[148]. Furthermore, *H19* maintains quiescence of obesity-predisposing PEGs in BAT. These hypotheses are supported by the finding that PEGs, such as *Mest,* regulate WAT-associated processes like adipogenesis and adipocyte cell size and number regulation[263] whereas the MEG *Ndn* has been shown to suppress adipocyte cell proliferation. Loss of *Ndn* expression resulted in increased adiposity due to hyperplasia of WAT cells[264]. Moreover, data have shown that DIO-induced 'whitening' of BAT leads to brown adipocyte death[265], a process which is suppressed by *H19*.

These overall results are is in accordance with the kinship theory of imprinting (see **1.4**) that predicts that PEGs should act to reduce energy-costly thermogenic

output[266] whilst MEGs are predicted to support higher levels of thermogenesis[167]. Data of a Master´s student of our lab, not included in this PhD thesis, were broadly consistent with this prediction as a loss of *H19* in brown preadipocytes led to a coordinated transcriptional upregulation of PEGs (*Igf2*, *Mest*, *Nnat*, *Peg3*, *Peg10*, *Plagl1* and *Gpr1*) whereas MEGs (*Cdkn1c*, *Dcn*, *Igf2r*, *Slc22a3*) were not affected. Accordingly, after conducting siH19 and or siMBD1 RNAi in 1° BAT, performed by a collaborator and not included in this thesis, we observed that BAT-abundant PEGs were increased with similar tendencies supporting the claim of functional *H19*/MBD1 complexes in these cells.

A publication by Ripoche et al. (1997) showed that a deletion of the *H19* gene resulted in an upregulation of the IGN and culminated in an overgrowth phenotype in mice and human[194]. This overgrowth phenotype has as well been associated with IDs, a group of rare congenital diseases affecting growth, development, and metabolism[267]. One of these diseases associated with the human *H19-Igf2* locus is the Beckwith-Wiedemann syndrome (BWS), (also called 'overgrowth disorder') in which affected children possess among other symptoms of macrosomnia. In this syndrome, a mutation in a specific region of the short arm of chromosome 11 referred to as 11p15 results in an over-activity of the IGF-2 gene, which is a growth factor[268]. However, different genetic defects have been identified in BWS patients such as maternal chromosomal rearrangements of 11p15, paternal uniparental disomy (UPD) of chromosome 11, abnormal DNA methylation, or that a single gene copy is located within 11p15 instead of two copies[269].

Another developmental growth restriction disorder characterised by low birth weight and neonatal hypoglycemia is Silver-Russell syndrome (SRS). Several epigenetic and genetic mutations have been linked to SRS, mainly involving imprinted genes[270]. In a study by Van de Pette et al. (2016), a mouse model was described which displayed a rare microduplication and with this, a double dose of the MEG *Cdkn1c,* often reported in some SRS patients[271]. These mice possessed substantially more BAT, something which is in accordance with our *H19* overexpression mouse model as that both MEGs *Cdkn1c* and *H19* supported either growth (*Cdkn1c*) or function (*H19*) of BAT. These observations are also supported by the kinship theory. A two-fold *Cdkn1c* expression resulted in fetal growth restriction with characteristics of SRS whereas the loss of *Cdkn1c* led to fetal overgrowth and characteristics of BWS[270]. This result was in accordance with both our gain- and loss-of-function mouse models as *H19* overexpression resulted in a smaller

and slimmer body shape on both diets, whereas *H19* loss resulted in an opposite phenotype. These results show that *H19* functions as a key player in the strict regulation of the IGN by inhibiting other imprinting genes and that the dysregulation of the IGN may result in serious diseases.

To investigate whether *H19* recruits specific BAT differentiation interaction partners that are not relevant for vWAT adipocyte formation or whether it is simply more abundant in BAT, it would be interesting to use depot-specific immortalized adipocytes and perform *H19* ChART experiments in these depot-specific cell systems as we already did with immortalized PIBA cells. Moreover, to uncover more interaction partners of *H19* one could also perform other techniques such as, e.g., chromatin isolation by RNA purification (ChIRP) and its applications to capture and purifiy specific lncRNA –chromatin complexes from the cell or also RNA-RNA interactions[272]. These experiments would further reveal the molecular mechanism through which *H19* affects and controls its targets.

4.4 Difficulties in obtaining human BAT biopsies justify the need for mouse studies

H19 is strongly conserved[227]. Therefore, we were curious to investigate whether human *H19* (*hH19*) could also be affected by obesity in humans. We quantified *hH19* levels in scWAT and vWAT biopsies from 169 lean and obese patients. *hH19* expression declined with increasing BMIs in both depots and correlated positively with markers of adipose 'beiging' like *UCP1* mRNA levels. Unfortunately, gene expression levels could not be determined in human BAT tissue due to the difficulties that still exist in obtaining human BAT biopsies for *ex vivo* studies.

Although human and mouse BAT mitochondria have comparable functions of UCP1[273], several intrinsic differences between human and mouse adipocytes such as the response to adrenocorticotropic hormone[274] have been observed. This stresses that not all findings in mouse models can be applied to the human context and that proper human-derived cell models are necessary to study human physiology and pathophysiology. The availability of those cell lines, however, is still difficult as primary human brown adipocytes are mainly available by surgical procedures, where cancer is suspected, in cervical and supraclavicular regions. As expected, the amount of the obtained material in these regions is most often limited[275]. Moreover, it is likely that the

metabolism of BAT cells obtained from those patients is changed as it is known from the 'emerging hallmark of cancer: reprogramming energy metabolism' that cancer is capable to modify, or reprogram cellular metabolism in order to fuel cell growth and division[276–278]. Thus, it has been shown that head and neck squamous cell carcinoma (HNSCC) used glycolytic and oxidative metabolism to support tumorigenesis[279]. Furthermore, Curry et al. (2014) demonstrated that genetic changes in HNSCC cells can affect the tumour microenvironment, and with this probably the adjacent BAT, by increasing reactive oxygen species (ROS), the production of cytokines and epithelial to mesenchymal transition (EMT)[279].

Only recently, Ding et al. (2018) have published the first comprehensive *de novo*-reconstructed human lncRNA catalog with 909 lncRNAs specifically detected in BAT by performing RNA-Seq on adult subcutaneous, omental WAT and fetal BAT[228]. Fetal BAT, however, was obtained from deceased donors, questioning which effect the death of the donor had on tissue conservation and gene expression[280].

Until proper methods are established to obtain primary human brown adipocytes, mouse studies are the most suitable resource to provide insights into the regulation of brown fat, especially for follow-up studies such as the characterization of candidate genes via gain- and loss-of-function experiments. Here the strong conservation of *H19* between mouse and human, the exciting results we obtained with the human cohort as well as the broad involvement of *hH19* in different biological processes, as presented earlier in this thesis, give reasons to specifically pursue further *H19* studies in mice.

4.5 First-line medication for T2DM Metformin influences *H19* expression in liver

When analysing *H19*, we could show that it has a supportive function in BAT and a positive influence on whole body metabolism in mice and, potentially, in humans. In contrast to that, when elevated in the liver *H19* has been shown to favour diabetic hyperglycemia[220]. The biological significance of these tissue-specific, and even opposing, effects is highlighted by the observation of similar findings in parallel studies, showing that lncRNAs can have varying biological functions within the individual tissue they are expressed[281].

Metformin is a biguanide compound and one of the most commonly used drugs for the treatment of T2DM worldwide due to its high efficacy and minimal side effects. Although its target has proved elusive, a recent study by Madiraju et al. (2014) has shown that Metformin suppresses hepatic gluconeogenesis[282]. Additionally, a recent study by Breining et al. (2018) identified BAT as putative metformin target as injected [^{11}C]-metformin was avidly taken up in the murine interscapular BAT depot[283]. One mechanism of how Metformin acts is by inducing genome-wide alterations in DNA methylation. More specifically, it modulates the activity of S-adenosylhomocysteine hydrolase (SAHH), the only mammalian enzyme capable of hydrolysing S-adenosylhomocysteine (SAH), to homocysteine and adenosine. SAH acts as a feedback inhibitor of S-adenosylmethionine (SAM)-dependent methyltransferases that methylate various cellular components, such as DNA, RNA, proteins, lipids, neurotransmitters and histones. Interestingly, during that process, microRNA *let-7* is up-regulated through AMPK activation, which leads to *H19* degradation[284]. The outcome of that process is the hypermethylation of genes.

Similar to these results, a study by Zhou et al. (2015), demonstrated that *H19* was able to influence genome-wide methylation by binding and subsequently inhibiting SAHH[261] opposite to the actions of Metformin. *H19* knockdown activated SAHH, resulting in active DNA methylation by DNMT3B. When *H19* was present, SAH accumulated and decreased DNMT3B-mediated methylation[261] resulting in hypomethylation of genes. Metformin and *H19* are therefore involved in a similar mechanism and are both able to influence genome-wide methylation patterns. One mechanism of how *H19* leads to differences in global methylation is via forming complexes with MBD1 and acting through a *trans* signalling mechanism.

Other human and animal studies that show a connection of Metformin and H19 have demonstrated that prenatal metformin exposure may lead to increased risk for metabolic disorders in adult offspring[285,286]. Fetuses exposed to metformin exhibited increased *H19* expression, which resulted in hypomethylation and elevated expression of *hepatocyte nuclear factor 4a* (*HNF4a*), a key factor for liver development and function. A perturbation of this pathway may contribute to the fetal origin of metabolic abnormalities in the adult[286].

From these studies, we learn that metformin targets both liver and BAT and that *H19* expression supports diabetes development in the liver whereas we could show that it has protective functions in BAT. Although the overall results of Metformin are without

a doubt promising, it would be interesting to explore the connection of Metformin and *H19* in more detail, especially the effect of Metformin-induced *H19* degradation in BAT.

4.6 Conclusions and future perspectives

Collectively, the data presented in this work revealed a novel crucial role for the conserved lncRNA *H19* in regulating BAT differentiation and function.

We demonstrated that the maternally expressed imprinted lncRNA *H19* increased upon cold-activation and decreased in obesity in BAT, which is in accordance with our human data that also showed an inverse correlation of *H19* with BMI. By using two genetic mouse models for gain- and loss-of-function, we demonstrated that *H19* overexpression promoted adipogenesis, oxidative metabolism, and mitochondrial respiration in brown but not white adipocytes *ex vivo* whereas silencing of *H19* resulted in impairment of these processes. *In vivo*, *H19* overexpression protected against DIO, increased energy dissipation, improved insulin sensitivity, and mitochondrial biogenesis whereas *H19* loss in AT sensitized towards HFD weight gains. Additionally, we observed that PEGs were largely absent from BAT and we demonstrated that *H19* recruits PEG-inactivating *H19*-MBD1 complexes, and thus acts possibly as a BAT-selective 'PEG gatekeeper'. These results have implications for our understanding of how monoallelic gene expression affects metabolism in rodents and, potentially, in humans.

In the future, it would be interesting to investigate whether *H19* is located in the mitochondrion and exhibits a specific interactome, in addition to MBD1 in the nucleus. This information, especially the molecular mechanisms, could be useful to develop therapeutic strategies to counteract obesity-associated pathologies. Although we have reasons to assume that *H19* regulates BAT homeostasis by its cell-intrinsic control of mitochondrial biogenesis in mature adipocytes and by maintaining quiescence of obesity-predisposing PEGs in BAT, the molecular effects through which *H19* affects its targets should be the object of further studies in order to develop specific therapeutic strategies for obesity associated diseases targeting *H19* or its interaction partners.

5 Summary

In light of the continuously rising number of patients suffering from obesity or its closely related, often life-threatening, diseases such as type 2 diabetes mellitus, the development of novel preventative or therapeutic measures is of utmost importance. Increasing brown adipose tissue (BAT) thermogenesis in mice and humans improves metabolic health. Therefore, understanding and controlling BAT function is of great interest for novel approaches to counteract obesity. Long noncoding RNAs (lncRNAs) emerged as potential targets for novel therapies due to their diverse functions, and tissue-specific effects, in the regulation of metabolic processes. However, the role of lncRNAs during BAT differentiation and function is not yet understood.

To explore this, we performed RNA-Sequencing and identified the maternally expressed lncRNA *H19* which was increased upon cold-mediated BAT activation and decreased upon chronic diet-induced obesity BAT dysfunction. Inverse correlations of *hH19* with Body-Mass-Index were also observed in a human cohort. We showed that *H19* overexpression promoted adipogenesis, oxidative metabolism, and mitochondrial respiration in brown but not white adipocytes whilst the silencing of *H19* impaired these processes. *In vivo*, *H19* overexpression protected against diet-induced-obesity, improved energy expenditure, insulin sensitivity, and mitochondrial biogenesis whereas the ablation of *H19* in fat sensitized towards high-fat diet (HFD) weight gains. Strikingly, paternally expressed genes (PEGs) were largely absent from BAT and we demonstrated, by performing Capture hybridization analysis of RNA targets coupled to Mass Spectrometry, that *H19* recruits PEG-inactivating *H19*-MBD1 complexes and potentially acts as BAT-selective 'PEG gatekeeper'.

Taken together, the results presented in this work reveal a novel function for the maternally expressed lncRNA *H19* as a BAT-regulatory lncRNA regulating BAT differentiation and function, thereby protecting from diet-induced obesity. Moreover, the results show how monoallelic gene expression affects metabolic homeostasis in both rodent models and, potentially, in human patients. Future studies will uncover the molecular mechanisms of how *H19* affects its molecular targets in more detail.

6 Zusammenfassung

Angesichts der stetig steigenden Anzahl an Patienten, welche mit Übergewicht oder damit assoziierten, oftmals lebensbedrohlichen Krankheiten, wie Typ 2 Diabetes Mellitus diagnostiziert werden, steigt die Notwendigkeit der Entwicklung präventiver und neuartiger Behandlungsmöglichkeiten. Vermehrte Thermogenese des braunen Fettgewebes (BAT) verbessert den Stoffwechsel in Mäusen und Menschen. Deshalb ist es wichtig die Funktion des braunen Fettgewebes zu analysieren und besser zu verstehen, damit neue Ansätze gefunden werden können, die dem Übergewicht entgegenwirken. Lange nicht-kodierende RNAs (lncRNAs) haben aufgrund ihrer diversen Funktionen und gewebespezifischen Effekte in der Regulation von Stoffwechselprozessen, als potentielle Kandidaten für neue Behandlungstherapien an Bedeutung gewonnen. Die Rolle von lncRNAs in der Differenzierung und Funktion von braunem Fettgewebe ist jedoch weiterhin unklar.

Um dies zu untersuchen haben wir eine RNA-Sequenzierung durchgeführt und die maternal exprimierte lncRNA *H19* identifiziert. *H19* zeigte eine erhöhte Genexpression während kälteinduzierter Aktivierung des braunen Fettgewebes, wohingegen die Expression durch ernährungsbedingtes Übergewicht und daraus resultierender Dysfunktion des braunen Fettgewebes verringert war. Zudem wurde eine inverse Korrelation von humanem *H19* (*hH19*) mit dem Body-Mass-Index einer humanen Kohorte beobachtet. Wir konnten zeigen, dass die Überexpression von *H19* die Fettbildung, den oxidativen Stoffwechsel und die mitochondriale Atmung in braunen, aber nicht in weißen Adipozyten verbesserte, wohingegen das Stilllegen von *H19* diese Prozesse negativ beeinträchtigte. Im lebenden Organismus, schützte die Überexpression von *H19* vor ernährungsbedingtem Übergewicht, verbesserte den Energieumsatz, die Insulin-Sensitivität und die mitochondriale Biogenese. Eine Entfernung von *H19* im Fettgewebe führte zu einem gegenteiligen Effekt und begünstigte die Gewichtszunahme durch Ernährung mit hohem Fettanteil. Eindrucksvoll konnten wir zeigen, dass paternal exprimierte Gene (PEG) im braunen Fettgewebe vorwiegend abwesend waren. Zudem haben wir entdeckt, dass *H19* PEG-inaktivierende *H19*-MBD1 Komplexe rekrutiert und als „PEG-Torwächter“ im braunen Fettgewebe fungiert.

Zusammenfassend zeigen die Ergebnisse dieser Arbeit eine neue Funktion für die maternal exprimierte lncRNA *H19* als eine BAT-regulatorische lncRNA, die die Differenzierung und die Funktion von braunem Fettgewebe reguliert und somit vor

ernährungsbedingtem Übergewicht schützt. Zudem zeigen die Ergebnisse, wie monoallelische Genexpression das metabolische Gleichgewicht in Nagetieren und möglicherweise auch in Menschen beeinflusst. Zukünftige Studien werden die molekularen Mechanismen, durch welche *H19* seine molekularen Zielmoleküle beeinflusst, detaillierter entschlüsseln.

7 References

1. World Health Organization. Obesity and overweight. *2018-02-16* (2018). Available at: http://www.who.int/en/news-room/fact-sheets/detail/obesity-and-overweight. (Accessed: 11th July 2018)
2. Kelly, T., Yang, W., Chen, C.-S., Reynolds, K. & He, J. Global burden of obesity in 2005 and projections to 2030. *Int. J. Obes.* **32,** 1431–1437 (2008).
3. Yazdi, F. T., Clee, S. M. & Meyre, D. Obesity genetics in mouse and human: back and forth, and back again. *PeerJ* **3,** e856 (2015).
4. Vogt, M. C. *et al.* Neonatal Insulin Action Impairs Hypothalamic Neurocircuit Formation in Response to Maternal High-Fat Feeding. *Cell* **156,** 495–509 (2014).
5. Van Gaal, L. F., Mertens, I. L. & De Block, C. E. Mechanisms linking obesity with cardiovascular disease. *Nature* **444,** 875–880 (2006).
6. Hotamisligil, G. S. Endoplasmic reticulum stress and atherosclerosis. *Nat. Med.* **16,** 396–399 (2010).
7. Rosen, E. D. & Spiegelman, B. M. What We Talk About When We Talk About Fat. *Cell* **156,** 20–44 (2014).
8. Torres, D. M., Williams, C. D. & Harrison, S. A. Features, Diagnosis, and Treatment of Nonalcoholic Fatty Liver Disease. *Clin. Gastroenterol. Hepatol.* **10,** 837–858 (2012).
9. Berrington de Gonzalez, A. *et al.* Body-Mass Index and Mortality among 1.46 Million White Adults. *N. Engl. J. Med.* **363,** 2211–2219 (2010).
10. NCD Risk Factor Collaboration (NCD-RisC). Trends in adult body-mass index in 200 countries from 1975 to 2014: a pooled analysis of 1698 population-based measurement studies with 19·2 million participants. *Lancet (London, England)* **387,** 1377–1396 (2016).
11. Haslam, D. W. & James, W. P. T. Obesity. *Lancet (London, England)* **366,** 1197–209 (2005).
12. World Health Organization. The top 10 causes of death. *2018-05-24* (2018). Available at: http://www.who.int/news-room/fact-sheets/detail/the-top-10-causes-of-death. (Accessed: 11th July 2018)
13. International Diabetes Federation. International Diabetes Federation - Facts & figures. (2018). Available at: https://www.idf.org/aboutdiabetes/what-is-

diabetes/facts-figures.html. (Accessed: 11th July 2018)

14. World Health Organization. Diabetes. *2017-11-15* (2017). doi:10.1371/journal.pmed.0030442
15. Biddinger, S. B. & Kahn, C. R. FROM MICE TO MEN: Insights into the Insulin Resistance Syndromes. *Annu. Rev. Physiol.* **68,** 123–158 (2006).
16. Boucher, J., Kleinridders, A. & Kahn, C. R. Insulin receptor signaling in normal and insulin-resistant states. *Cold Spring Harb. Perspect. Biol.* **6,** a009191 (2014).
17. Prentki, M. & Nolan, C. J. Islet beta cell failure in type 2 diabetes. *J. Clin. Invest.* **116,** 1802–12 (2006).
18. World Health Organization. WHO | About diabetes. *WHO* (2014).
19. Belgardt, B. F. & Brüning, J. C. CNS leptin and insulin action in the control of energy homeostasis. *Ann. N. Y. Acad. Sci.* **1212,** 97–113 (2010).
20. Lenard, N. R. & Berthoud, H.-R. Central and Peripheral Regulation of Food Intake and Physical Activity: Pathways and Genes. *Obesity* **16,** S11–S22 (2008).
21. Sanchez-Gurmaches, J., Hung, C.-M. & Guertin, D. A. Emerging Complexities in Adipocyte Origins and Identity. *Trends Cell Biol.* **26,** 313–326 (2016).
22. Cannon, B. & Nedergaard, J. Brown Adipose Tissue: Function and Physiological Significance. *Physiol Rev.* (2004)
23. Ibrahim, M. M. Subcutaneous and visceral adipose tissue: structural and functional differences. *Obes. Rev.* **11,** 11–18 (2010).
24. Wang, W. & Seale, P. Control of brown and beige fat development. *Nat. Rev. Mol. Cell Biol.* **17,** 691–702 (2016).
25. Hudak, C. S. & Sul, H. S. Pref-1, a Gatekeeper of Adipogenesis. *Front. Endocrinol. (Lausanne).* **4,** 79 (2013).
26. Farmer, S. R. Transcriptional control of adipocyte formation. *Cell Metab.* **4,** 263–273 (2006).
27. Bartelt, A. & Heeren, J. The holy grail of metabolic disease. *Curr. Opin. Lipidol.* **23,** 190–195 (2012).
28. Rothwell, N. J. & Stock, M. J. Luxuskonsumption, diet-induced thermogenesis and brown fat: the case in favour. *Clin. Sci. (Lond).* **64,** 19–23 (1983).
29. Luo, L. & Liu, M. Adipose tissue in control of metabolism. *J. Endocrinol.* **231,** R77–R99 (2016).
30. Wajchenberg, B. L. Subcutaneous and Visceral Adipose Tissue: Their Relation to the Metabolic Syndrome. *Endocr. Rev.* **21,** 697–738 (2000).

31. Arner, P. Regional adipocity in man. *J. Endocrinol.* **155,** 191–2 (1997).
32. Pellegrinelli, V., Carobbio, S. & Vidal-Puig, A. Adipose tissue plasticity: how fat depots respond differently to pathophysiological cues. *Diabetologia* **59,** 1075–1088 (2016).
33. Freedland, E. S. Role of a critical visceral adipose tissue threshold (CVATT) in metabolic syndrome: implications for controlling dietary carbohydrates: a review. *Nutr. Metab. (Lond).* **1,** 12 (2004).
34. Lee, M.-J., Wu, Y. & Fried, S. K. Adipose tissue heterogeneity: Implication of depot differences in adipose tissue for obesity complications. *Mol. Aspects Med.* **34,** 1–11 (2013).
35. Tran, T. T. & Kahn, C. R. Transplantation of adipose tissue and stem cells: role in metabolism and disease. *Nat. Rev. Endocrinol.* **6,** 195–213 (2010).
36. Thyagarajan, B. & Foster, M. T. Beiging of white adipose tissue as a therapeutic strategy for weight loss in humans. *Horm. Mol. Biol. Clin. Investig.* **31,** (2017).
37. Harms, M. J. *et al.* Prdm16 Is Required for the Maintenance of Brown Adipocyte Identity and Function in Adult Mice. *Cell Metab.* **19,** 593–604 (2014).
38. Wang, W. *et al.* Ebf2 is a selective marker of brown and beige adipogenic precursor cells. *Proc. Natl. Acad. Sci. U. S. A.* **111,** 14466–71 (2014).
39. Seale, P. *et al.* PRDM16 controls a brown fat/skeletal muscle switch. *Nature* **454,** 961–967 (2008).
40. Atit, R. *et al.* β-catenin activation is necessary and sufficient to specify the dorsal dermal fate in the mouse. *Dev. Biol.* **296,** 164–176 (2006).
41. Cypess, A. M. *et al.* Anatomical localization, gene expression profiling and functional characterization of adult human neck brown fat. *Nat. Med.* **19,** 635–639 (2013).
42. Timmons, J. A. *et al.* Myogenic gene expression signature establishes that brown and white adipocytes originate from distinct cell lineages. *Proc. Natl. Acad. Sci. U. S. A.* **104,** 4401–6 (2007).
43. Forner, F. *et al.* Proteome Differences between Brown and White Fat Mitochondria Reveal Specialized Metabolic Functions. *Cell Metab.* **10,** 324–335 (2009).
44. Ohno, H., Shinoda, K., Ohyama, K., Sharp, L. Z. & Kajimura, S. EHMT1 controls brown adipose cell fate and thermogenesis through the PRDM16 complex. *Nature* **504,** 163–167 (2013).
45. Trajkovski, M., Ahmed, K., Esau, C. C. & Stoffel, M. MyomiR-133 regulates brown fat

differentiation through Prdm16. *Nat. Cell Biol.* **14,** 1330–1335 (2012).

46. Yin, H. *et al.* MicroRNA-133 Controls Brown Adipose Determination in Skeletal Muscle Satellite Cells by Targeting Prdm16. *Cell Metab.* **17,** 210–224 (2013).
47. Petrovic, N., Shabalina, I. G., Timmons, J. A., Cannon, B. & Nedergaard, J. Thermogenically competent nonadrenergic recruitment in brown preadipocytes by a PPARγ agonist. *Am. J. Physiol. Metab.* **295,** E287–E296 (2008).
48. Wu, J. *et al.* Beige adipocytes are a distinct type of thermogenic fat cell in mouse and human. *Cell* **150,** 366–76 (2012).
49. Harms, M. & Seale, P. Brown and beige fat: development, function and therapeutic potential. *Nat. Med.* **19,** 1252–1263 (2013).
50. Sanchez-Gurmaches, J. *et al.* PTEN Loss in the Myf5 Lineage Redistributes Body Fat and Reveals Subsets of White Adipocytes that Arise from Myf5 Precursors. *Cell Metab.* **16,** 348–362 (2012).
51. Vitali, A. *et al.* The adipose organ of obesity-prone C57BL/6J mice is composed of mixed white and brown adipocytes. *J. Lipid Res.* **53,** 619–29 (2012).
52. Wang, Q. A., Tao, C., Gupta, R. K. & Scherer, P. E. Tracking adipogenesis during white adipose tissue development, expansion and regeneration. *Nat. Med.* **19,** 1338–1344 (2013).
53. Ikeda, K., Maretich, P. & Kajimura, S. The Common and Distinct Features of Brown and Beige Adipocytes. *Trends Endocrinol. Metab.* **29,** 191–200 (2018).
54. Klaus, S., Ely, M., Encke, D. & Heldmaier, G. Functional assessment of white and brown adipocyte development and energy metabolism in cell culture. Dissociation of terminal differentiation and thermogenesis in brown adipocytes. *J. Cell Sci.* **108 (Pt 10),** 3171–80 (1995).
55. Ohno, H., Shinoda, K., Spiegelman, B. M. & Kajimura, S. PPARγ agonists induce a white-to-brown fat conversion through stabilization of PRDM16 protein. *Cell Metab.* **15,** 395–404 (2012).
56. Guerra, C., Koza, R. A., Yamashita, H., Walsh, K. & Kozak, L. P. Emergence of brown adipocytes in white fat in mice is under genetic control. Effects on body weight and adiposity. *J. Clin. Invest.* **102,** 412–20 (1998).
57. Nedergaard, J. *et al.* UCP1: the only protein able to mediate adaptive non-shivering thermogenesis and metabolic inefficiency. *Biochim. Biophys. Acta - Bioenerg.* **1504,** 82–106 (2001).
58. Puigserver, P. & Spiegelman, B. M. Peroxisome Proliferator-Activated Receptor-γ

Coactivator 1α (PGC-1α): Transcriptional Coactivator and Metabolic Regulator. *Endocr. Rev.* **24,** 78–90 (2003).

59. Uldry, M. *et al.* Complementary action of the PGC-1 coactivators in mitochondrial biogenesis and brown fat differentiation. *Cell Metab.* **3,** 333–341 (2006).
60. Chechi, K., Nedergaard, J. & Richard, D. Brown adipose tissue as an anti-obesity tissue in humans. *Obes. Rev.* **15,** 92–106 (2014).
61. Shi, F. & Collins, S. Second messenger signaling mechanisms of the brown adipocyte thermogenic program: an integrative perspective. *Horm. Mol. Biol. Clin. Investig.* **31,** (2017).
62. Butow, R. A. & Bahassi, E. M. Adaptive thermogenesis: Orchestrating mitochondrial biogenesis. *Curr. Biol.* **9,** R767–R769 (1999).
63. Shadelt, G. S. & Clayton, D. A. Mitochondrial Transcription Initiation. *J. Biol. Chem*. **268,** 16083–16086 (1993).
64. Nicholls, D. G. & Locke, R. M. Thermogenic mechanisms in brown fat. *Physiol. Rev.* **64,** 1–64 (1984).
65. Scarpulla, R. C. Nuclear Control of Respiratory Chain Expression in Mammalian Cells. *J. Bioenerg. Biomembr.* **29,** 109–119 (1997).
66. Wang, W. & Seale, P. Control of brown and beige fat development. *Nat. Rev. Mol. Cell Biol.* **17,** 691–702 (2016).
67. Lidell, M. E. *et al.* Evidence for two types of brown adipose tissue in humans. *Nat. Med.* **19,** 631–634 (2013).
68. Cypess, A. M. *et al.* Identification and importance of brown adipose tissue in adult humans. *N. Engl. J. Med.* **360,** 1509–17 (2009).
69. Saito, M. *et al.* High incidence of metabolically active brown adipose tissue in healthy adult humans: effects of cold exposure and adiposity. *Diabetes* **58,** 1526–31 (2009).
70. Virtanen, K. A. *et al.* Functional Brown Adipose Tissue in Healthy Adults. *N. Engl. J. Med.* **360,** 1518–1525 (2009).
71. Nedergaard, J., Bengtsson, T. & Cannon, B. Unexpected evidence for active brown adipose tissue in adult humans. *Am. J. Physiol. Metab.* **293,** E444–E452 (2007).
72. Rogers, N. H., Landa, A., Park, S. & Smith, R. G. Aging leads to a programmed loss of brown adipocytes in murine subcutaneous white adipose tissue. *Aging Cell* **11,** 1074–83 (2012).
73. Villarroya, J., Cereijo, R. & Villarroya, F. An endocrine role for brown adipose

tissue? *Am. J. Physiol. Metab.* **305,** E567–E572 (2013).

74. Jespersen, N. Z. *et al.* A classical brown adipose tissue mRNA signature partly overlaps with brite in the supraclavicular region of adult humans. *Cell Metab.* **17,** 798–805 (2013).
75. Enerbäck, S. *et al.* Mice lacking mitochondrial uncoupling protein are cold-sensitive but not obese. *Nature* **387,** 90–94 (1997).
76. Keipert, S. *et al.* Long-Term Cold Adaptation Does Not Require FGF21 or UCP1. *Cell Metab.* **26,** 437–446.e5 (2017).
77. Rothwell, N. J. & Stock, M. J. A role for brown adipose tissue in diet-induced thermogenesis. *Nature* **281,** 31–35 (1979).
78. Feldmann, H. M., Golozoubova, V., Cannon, B. & Nedergaard, J. UCP1 Ablation Induces Obesity and Abolishes Diet-Induced Thermogenesis in Mice Exempt from Thermal Stress by Living at Thermoneutrality. *Cell Metab.* **9,** 203–209 (2009).
79. Lowell, B. B. *et al.* Development of obesity in transgenic mice after genetic ablation of brown adipose tissue. *Nature* **366,** 740–742 (1993).
80. Kopecky, J., Clarke, G., Enerbäck, S., Spiegelman, B. & Kozak, L. P. Expression of the mitochondrial uncoupling protein gene from the aP2 gene promoter prevents genetic obesity. *J. Clin. Invest.* **96,** 2914–23 (1995).
81. Stanford, K. I. *et al.* Brown adipose tissue regulates glucose homeostasis and insulin sensitivity. *J. Clin. Invest.* **123,** 215–23 (2013).
82. van Marken Lichtenbelt, W. D. *et al.* Cold-Activated Brown Adipose Tissue in Healthy Men. *N. Engl. J. Med.* **360,** 1500–1508 (2009).
83. Yoneshiro, T. *et al.* Recruited brown adipose tissue as an antiobesity agent in humans. *J. Clin. Invest.* **123,** 3404–3408 (2013).
84. Hanssen, M. J. W. *et al.* Short-term cold acclimation improves insulin sensitivity in patients with type 2 diabetes mellitus. *Nat. Med.* **21,** 863–865 (2015).
85. Cypess, A. M. *et al.* Activation of human brown adipose tissue by a β3-adrenergic receptor agonist. *Cell Metab.* **21,** 33–8 (2015).
86. Djebali, S. *et al.* Landscape of transcription in human cells. *Nature* **489,** 101–108 (2012).
87. Consortium, T. E. P. An integrated encyclopedia of DNA elements in the human genome. *Nature* **489,** 57–74 (2012).
88. Catalanotto, C., Cogoni, C. & Zardo, G. MicroRNA in Control of Gene Expression: An Overview of Nuclear Functions. *Int. J. Mol. Sci.* **17,** (2016).

89. Weick, E.-M. & Miska, E. A. piRNAs: from biogenesis to function. *Development* **141,** 3458–71 (2014).
90. Dupuis-Sandoval, F., Poirier, M. & Scott, M. S. The emerging landscape of small nucleolar RNAs in cell biology. *Wiley Interdiscip. Rev. RNA* **6,** 381–397 (2015).
91. Mattick, J. S. & Makunin, I. V. Non-coding RNA. *Hum. Mol. Genet.* **15,** R17–R29 (2006).
92. Rinn, J. L. & Chang, H. Y. Genome regulation by long noncoding RNAs. *Annu. Rev. Biochem.* **81,** 145–66 (2012).
93. Cech, T. R. & Steitz, J. A. The Noncoding RNA Revolution—Trashing Old Rules to Forge New Ones. *Cell* **157,** 77–94 (2014).
94. Kapranov, P. *et al.* Large-scale transcriptional activity in chromosomes 21 and 22. *Science* **296,** 916–9 (2002).
95. Rinn, J. L. *et al.* The transcriptional activity of human Chromosome 22. *Genes Dev.* **17,** 529–40 (2003).
96. Maeda, N. *et al.* Transcript Annotation in FANTOM3: Mouse Gene Catalog Based on Physical cDNAs. *PLoS Genet.* **2,** e62 (2006).
97. Guttman, M. *et al.* Chromatin signature reveals over a thousand highly conserved large non-coding RNAs in mammals. *Nature* **458,** 223–227 (2009).
98. Cabili, M. N. *et al.* Integrative annotation of human large intergenic noncoding RNAs reveals global properties and specific subclasses. *Genes Dev.* **25,** 1915–27 (2011).
99. Guttman, M. *et al.* Ab initio reconstruction of cell type–specific transcriptomes in mouse reveals the conserved multi-exonic structure of lincRNAs. *Nat. Biotechnol.* **28,** 503–510 (2010).
100. Iyer, M. K. *et al.* The landscape of long noncoding RNAs in the human transcriptome. *Nat. Genet.* **47,** 199–208 (2015).
101. Anderson, D. M. *et al.* A micropeptide encoded by a putative long noncoding RNA regulates muscle performance. *Cell* **160,** 595–606 (2015).
102. Lin, M. F., Jungreis, I. & Kellis, M. PhyloCSF: a comparative genomics method to distinguish protein coding and non-coding regions. *Bioinformatics* **27,** i275–i282 (2011).
103. Kong, L. *et al.* CPC: assess the protein-coding potential of transcripts using sequence features and support vector machine. *Nucleic Acids Res.* **35,** W345–W349 (2007).

104. Arrial, R. T., Togawa, R. C. & Brigido, M. Screening non-coding RNAs in transcriptomes from neglected species using PORTRAIT: case study of the pathogenic fungus Paracoccidioides brasiliensis. *BMC Bioinformatics* **10,** 239 (2009).
105. Wang, L. *et al.* CPAT: Coding-Potential Assessment Tool using an alignment-free logistic regression model. *Nucleic Acids Res.* **41,** e74–e74 (2013).
106. Gupta, R. a *et al.* Long non-coding RNA HOTAIR reprograms chromatin state to promote cancer metastasis. *Nature* **464,** 1071–6 (2010).
107. Huarte, M. *et al.* A large intergenic non-coding RNA induced by p53 mediates global gene repression in the p53 response. *Cell* **142,** 409–419 (2010).
108. Sun, L. *et al.* Long noncoding RNAs regulate adipogenesis. *Proc. Natl. Acad. Sci. U. S. A.* **110,** 3387–92 (2013).
109. Vollmers, C. *et al.* Circadian oscillations of protein-coding and regulatory RNAs in a highly dynamic mammalian liver epigenome. *Cell Metab.* **16,** 833–45 (2012).
110. Wilusz, J. E., Sunwoo, H. & Spector, D. L. Long noncoding RNAs: functional surprises from the RNA world. *Genes Dev.* **23,** 1494–504 (2009).
111. Ponting, C. P., Oliver, P. L. & Reik, W. Evolution and functions of long noncoding RNAs. *Cell* **136,** 629–41 (2009).
112. Wapinski, O. & Chang, H. Y. Long noncoding RNAs and human disease. *Trends Cell Biol.* **21,** 354–61 (2011).
113. Ietswaart, R., Wu, Z. & Dean, C. Flowering time control: another window to the connection between antisense RNA and chromatin. *Trends Genet.* **28,** 445–453 (2012).
114. Niederer, R. O., Hass, E. P. & Zappulla, D. C. Long Noncoding RNAs in the Yeast S. cerevisiae. *Adv Exp Med Biol.* 119–132 (Springer, Singapore, 2017).
115. Lee, J. T. Epigenetic Regulation by Long Noncoding RNAs. *Science (80-.).* **338,** 1435–1439 (2012).
116. Wang, K. C. & Chang, H. Y. Molecular mechanisms of long noncoding RNAs. *Mol. Cell* **43,** 904–14 (2011).
117. Cesana, M. *et al.* A long noncoding RNA controls muscle differentiation by functioning as a competing endogenous RNA. *Cell* **147,** 358–69 (2011).
118. Yang, Q. *et al.* Analysis of LncRNA expression in cell differentiation. *RNA Biol.* **15,** 413–422 (2018).
119. Batista, P. J. & Chang, H. Y. Long noncoding RNAs: cellular address codes in

development and disease. *Cell* **152,** 1298–307 (2013).

120. Alvarez-Dominguez, J. R. *et al.* De novo Reconstruction of Adipose Tissue Transcriptomes Reveals Novel Long Non-coding RNAs that Regulate Brown Adipocyte Development HHS Public Access. *Cell Metab* **21,** 764–776 (2015).
121. Panzitt, K. *et al.* Characterization of HULC, a novel gene with striking up-regulation in hepatocellular carcinoma, as noncoding RNA. *Gastroenterology* **132,** 330–42 (2007).
122. Ji, P. *et al.* MALAT-1, a novel noncoding RNA and thymosin β4 predict metastasis and survival in early-stage non-small cell lung cancer. *Oncogene* **22,** 8031–8041 (2003).
123. Feng, J. *et al.* The Evf-2 noncoding RNA is transcribed from the Dlx-5/6 ultraconserved region and functions as a Dlx-2 transcriptional coactivator. *Genes Dev.* **20,** 1470–84 (2006).
124. Zhao, X. Y., Li, S., Wang, G. X., Yu, Q. & Lin, J. D. A Long noncoding RNA transcriptional regulatory circuit drives thermogenic adipocyte differentiation. *Mol. Cell* (2014).
125. Martianov, I., Ramadass, A., Serra Barros, A., Chow, N. & Akoulitchev, A. Repression of the human dihydrofolate reductase gene by a non-coding interfering transcript. *Nature* **445,** 666–670 (2007).
126. Wang, X. *et al.* Induced ncRNAs allosterically modify RNA-binding proteins in cis to inhibit transcription. *Nature* **454,** 126–130 (2008).
127. Kallen, A. N. *et al.* The Imprinted H19 LncRNA Antagonizes Let-7 MicroRNAs. *Mol. Cell* **52,** 101–112 (2013).
128. Wang, Y. *et al.* Endogenous miRNA sponge lincRNA-RoR regulates Oct4, Nanog, and Sox2 in human embryonic stem cell self-renewal. *Dev. Cell* **25,** 69–80 (2013).
129. Rinn, J. L. *et al.* Functional demarcation of active and silent chromatin domains in human HOX loci by noncoding RNAs. *Cell* **129,** 1311–23 (2007).
130. Kaneko, S. *et al.* Interactions between JARID2 and noncoding RNAs regulate PRC2 recruitment to chromatin. *Mol. Cell* **53,** 290–300 (2014).
131. Cifuentes-Rojas, C., Hernandez, A. J., Sarma, K. & Lee, J. T. Regulatory interactions between RNA and polycomb repressive complex 2. *Mol. Cell* **55,** 171–85 (2014).
132. Yoon, J.-H. *et al.* LincRNA-p21 suppresses target mRNA translation. *Mol. Cell* **47,** 648–55 (2012).
133. Tripathi, V. *et al.* The nuclear-retained noncoding RNA MALAT1 regulates

alternative splicing by modulating SR splicing factor phosphorylation. *Mol. Cell* **39,** 925–38 (2010).

134. Gong, C. & Maquat, L. E. lncRNAs transactivate STAU1-mediated mRNA decay by duplexing with 3' UTRs via Alu elements. *Nature* **470,** 284–8 (2011).
135. Hu, W., Alvarez-Dominguez, J. R. & Lodish, H. F. Regulation of mammalian cell differentiation by long non-coding RNAs. *EMBO Rep.* **13,** 971–83 (2012).
136. Zhao, X.-Y. & Lin, J. D. Long Noncoding RNAs: A New Regulatory Code in Metabolic Control. *Trends Biochem. Sci.* **40,** 586–96 (2015).
137. Kahn, S. E., Hull, R. L. & Utzschneider, K. M. Mechanisms linking obesity to insulin resistance and type 2 diabetes. *Nature* **444,** 840–6 (2006).
138. Ellis, B. C., Graham, L. D. & Molloy, P. L. CRNDE, a long non-coding RNA responsive to insulin/IGF signaling, regulates genes involved in central metabolism. *Biochim. Biophys. Acta* **1843,** 372–86 (2014).
139. Kajimura, S., Seale, P. & Spiegelman, B. M. Transcriptional Control of Brown Fat Development. *Cell Metab.* **11,** 257–262 (2010).
140. Birney, E. *et al.* Identification and analysis of functional elements in 1% of the human genome by the ENCODE pilot project. *Nature* **447,** 799–816 (2007).
141. Hacisuleyman, E. *et al.* Topological organization of multichromosomal regions by the long intergenic noncoding RNA Firre. *Nat. Struct. Mol. Biol.* **21,** 198–206 (2014).
142. Jimenez, M. A., Akerblad, P., Sigvardsson, M. & Rosen, E. D. Critical role for Ebf1 and Ebf2 in the adipogenic transcriptional cascade. *Mol. Cell. Biol.* **27,** 743–57 (2007).
143. Rajakumari, S. *et al.* EBF2 determines and maintains brown adipocyte identity. *Cell Metab.* **17,** 562–74 (2013).
144. Morison, I. M., Ramsay, J. P. & Spencer, H. G. A census of mammalian imprinting. *Trends Genet.* **21,** 457–465 (2005).
145. Mcgrath, J. & Solter, D. Completion of Mouse Embryogenesis Requires Both the Maternal and Paternal Genomes. *Cell* **37,** 179–183 (1984).
146. Surani, M. A. H., Barton, S. C. & Norris, M. L. Development of reconstituted mouse eggs suggests imprinting of the genome during gametogenesis. *Nature* **308,** 548–550 (1984).
147. Cattanach, B. M. & Kirk, M. Differential activity of maternally and paternally derived chromosome regions in mice. *Nature* **315,** 496–498 (1985).

148. Peters, J. The role of genomic imprinting in biology and disease: an expanding view. *Nat. Rev. Genet.* **15,** 517–530 (2014).
149. Moore, T. & Haig, D. Genomic imprinting in mammalian development: a parental tug-of-war. *Trends Genet.* **7,** 45–49 (1991).
150. Isles, A. R., Davies, W. & Wilkinson, L. S. Genomic imprinting and the social brain. *Philos. Trans. R. Soc. Lond. B. Biol. Sci.* **361,** 2229–37 (2006).
151. Keverne, E. B. & Curley, J. P. Epigenetics, brain evolution and behaviour. *Front. Neuroendocrinol.* **29,** 398–412 (2008).
152. Reik, W. & Walter, J. Genomic imprinting: parental influence on the genome. *Nat. Rev. Genet.* **2,** 21–32 (2001).
153. Kong, A. *et al.* Parental origin of sequence variants associated with complex diseases. *Nature* **462,** 868–874 (2009).
154. Wakeling, E. L. *et al.* Diagnosis and management of Silver–Russell syndrome: first international consensus statement. *Nat. Rev. Endocrinol.* **13,** 105–124 (2016).
155. Bell, A. C. & Felsenfeld, G. Methylation of a CTCF-dependent boundary controls imprinted expression of the Igf2 gene. *Nature* **405,** 482–485 (2000).
156. Hark, A. T. *et al.* CTCF mediates methylation-sensitive enhancer-blocking activity at the H19/Igf2 locus. *Nature* **405,** 486–489 (2000).
157. Ferguson-Smith, A. C. Genomic imprinting: the emergence of an epigenetic paradigm. *Nat. Rev. Genet.* **12,** 565–575 (2011).
158. Meng, L. *et al.* Towards a therapy for Angelman syndrome by targeting a long non-coding RNA. *Nature* **518,** 409–412 (2014).
159. Hall, J. G. Genomic Imprinting: Review and Relevance to Human; Diseases. *Am. J. Hum. Genet* **46,** 857–873 (1990).
160. Curley, J. P. *et al.* Increased body fat in mice with a targeted mutation of the paternally expressed imprinted gene *Peg3*. *FASEB J.* **19,** 1302–1304 (2005).
161. Plagge, A. *et al.* The imprinted signaling protein XLαs is required for postnatal adaptation to feeding. *Nat. Genet.* **36,** 818–826 (2004).
162. Peters, J. *et al.* Imprinting control within the compact Gnas locus. *Cytogenet. Genome Res.* **113,** 194–201 (2006).
163. Xie, T. *et al.* Severe obesity and insulin resistance due to deletion of the maternal Gsalpha allele is reversed by paternal deletion of the Gsalpha imprint control region. *Endocrinology* **149,** 2443–50 (2008).
164. Yu, S. *et al.* Paternal versus maternal transmission of a stimulatory G-protein alpha

subunit knockout produces opposite effects on energy metabolism. *J. Clin. Invest.* **105,** 615–23 (2000).

165. Tseng, Y.-H. *et al.* Prediction of preadipocyte differentiation by gene expression reveals role of insulin receptor substrates and necdin. *Nat. Cell Biol.* **7,** 601–611 (2005).
166. Charalambous, M. *et al.* Imprinted Gene Dosage Is Critical for the Transition to Independent Life. *Cell Metab.* **15,** 209–221 (2012).
167. Haig, D. Huddling: brown fat, genomic imprinting and the warm inner glow. *Curr. Biol.* **18,** R172-4 (2008).
168. Pachnis, V., Belayew, A. & Tilghman, S. M. Locus unlinked to o-fetoprotein under the control of the murine raf and Rif genes (regulatory genes/tissue specificity/cDNA cloning/developmental regulation). *Genetics* **81,** 5523–5527 (1984).
169. Bartolomei, M. S., Zemel, S. & Tilghman, S. M. Parental imprinting of the mouse H19 gene. *Nature* **351,** 153–155 (1991).
170. Zhang, Y. & Tycko, B. Monoallelic expression of the human H19 gene. *Nat. Genet.* **1,** 40–44 (1992).
171. Brannan, C. I., Dees, E. C., Ingram, R. S. & Tilghman, S. M. The product of the H19 gene may function as an RNA. *Mol. Cell. Biol.* **10,** 28–36 (1990).
172. Kent, W. J. *et al.* The human genome browser at UCSC. *Genome Res.* **12,** 996–1006 (2002).
173. Dey, B. K., Pfeifer, K. & Dutta, A. The H19 long noncoding RNA gives rise to microRNAs miR-675-3p and miR-675-5p to promote skeletal muscle differentiation and regeneration. *Genes Dev.* **28,** 491–501 (2014).
174. Pope, C., Mishra, S., Russell, J., Zhou, Q. & Zhong, X.-B. Targeting H19, an Imprinted Long Non-Coding RNA, in Hepatic Functions and Liver Diseases. *Dis. (Basel, Switzerland)* **5,** (2017).
175. Leighton, P. A., Saam, J. R., Ingram, R. S., Stewart, C. L. & Tilghman, S. M. An enhancer deletion affects both H19 and Igf2 expression. *Genes Dev.* 2079-2089 (1995).
176. Drewell, R. A., Goddard, C. J., Thomas, J. O. & Surani, M. A. Methylation-dependent silencing at the H19 imprinting control region by MeCP2. *Nucleic Acids Res.* **30,** 1139–44 (2002).
177. Brunkow, M. E. & Tilghman, S. M. Ectopic expression of the H19 gene in mice

causes prenatal lethality. *Genes Dev.* **5,** 1092–101 (1991).

178. Nordin, M., Bergman, D., Halje, M., Engström, W. & Ward, A. Epigenetic regulation of the *Igf2/H19* gene cluster. *Cell Prolif.* **47,** 189–199 (2014).
179. Gabory, A., Ripoche, M.-A., Yoshimizu, T. & Dandolo, L. The H19 gene: regulation and function of a non-coding RNA. *Cytogenet. Genome Res.* **113,** 188–93 (2006).
180. Raveh, E., Matouk, I. J., Gilon, M. & Hochberg, A. The H19 Long non-coding RNA in cancer initiation, progression and metastasis – a proposed unifying theory. *Mol. Cancer* **14,** 184 (2015).
181. Matouk, I. J. *et al.* The H19 Non-Coding RNA Is Essential for Human Tumor Growth. *PLoS One* **2,** e845 (2007).
182. Hao, Y., Crenshaw, T., Moulton, T., Newcomb, E. & Tycko, B. Tumour-suppressor activity of H19 RNA. *Nature* **365,** 764–767 (1993).
183. Yoshimizu, T. *et al.* The H19 locus acts in vivo as a tumor suppressor. *Proc. Natl. Acad. Sci. U. S. A.* **105,** 12417–22 (2008).
184. Tsang, W. P. *et al.* Oncofetal H19-derived miR-675 regulates tumor suppressor RB in human colorectal cancer. *Carcinogenesis* (2010).
185. Yamamoto, Y., Nishikawa, Y., Tokairin, T., Omori, Y. & Enomoto, K. Increased expression of H19 non-coding mRNA follows hepatocyte proliferation in the rat and mouse. *J. Hepatol.* **40,** 808–814 (2004).
186. Gabory, A., Jammes, H. & Dandolo, L. The H19 locus: Role of an imprinted non-coding RNA in growth and development. *BioEssays* (2010).
187. Gabory, A. *et al.* H19 acts as a trans regulator of the imprinted gene network controlling growth in mice. *Development* **136,** 3413–21 (2009).
188. Keniry, A. *et al.* The H19 lincRNA is a developmental reservoir of miR-675 that suppresses growth and Igf1r. *Nat. Cell Biol.* **14,** 659–665 (2012).
189. DeChiara, T. M., Robertson, E. J. & Efstratiadis, A. Parental imprinting of the mouse insulin-like growth factor II gene. *Cell* **64,** 849–859 (1991).
190. Monnier, P. *et al.* H19 lncRNA controls gene expression of the Imprinted Gene Network by recruiting MBD1. *Proc. Natl. Acad. Sci. U. S. A.* **110,** 20693–8 (2013).
191. Zhang, L. *et al.* Epigenetic activation of the MiR-200 family contributes to H19-mediated metastasis suppression in hepatocellular carcinoma. *Carcinogenesis* **34,** 577–586 (2013).
192. Röder, P. V, Wu, B., Liu, Y. & Han, W. Pancreatic regulation of glucose homeostasis. *Exp. Mol. Med.* **48,** e219 (2016).

193. Han, D. K., Khaing, Z. Z., Pollock, R. A., Haudenschild, C. C. & Liau, G. H19, a marker of developmental transition, is reexpressed in human atherosclerotic plaques and is regulated by the insulin family of growth factors in cultured rabbit smooth muscle cells. *J. Clin. Invest.* **97,** 1276–85 (1996).
194. Ripoche, M. A., Kress, C., Poirier, F. & Dandolo, L. Deletion of the H19 transcription unit reveals the existence of a putative imprinting control element. *Genes Dev.* **11,** 1596–604 (1997).
195. Leighton, P. A., Ingram, R. S., Eggenschwiler, J., Efstratiadis, A. & Tilghman, S. M. Disruption of imprinting caused by deletion of the H19 gene region in mice. *Nature* **375,** 34–39 (1995).
196. Eriksson, J. G., Forsen, T. J., Osmond, C. & Barker, D. J. P. Pathways of infant and childhood growth that lead to type 2 diabetes. *Diabetes Care* **26,** 3006–10 (2003).
197. Gao, Y. *et al.* The H19/let-7 double-negative feedback loop contributes to glucose metabolism in muscle cells. *Nucleic Acids Res.* **42,** 13799–13811 (2014).
198. Ding, G. L. *et al.* Transgenerational glucose intolerance with Igf2/H19 epigenetic alterations in mouse islet induced by intrauterine hyperglycemia. *Diabetes* **61,** 1133–1142 (2012).
199. Kim, J. *et al.* Long noncoding RNAs in diseases of aging. *Biochim. Biophys. Acta* **1859,** 209–21 (2016).
200. Kornfeld, J. & Brüning, J. C. Regulation of metabolism by long , non-coding RNAs. *Front. Genet.* **5,** (2014).
201. You, L. *et al.* GM13133 is a negative regulator in mouse white adipocytes differentiation and drives the characteristics of brown adipocytes. *J. Cell. Physiol.* **233,** 313–324 (2018).
202. Mi, L., Zhao, X.-Y., Li, S., Yang, G. & Lin, J. D. Conserved function of the long noncoding RNA Blnc1 in brown adipocyte differentiation. *Mol. Metab.* **6,** 101–110 (2017).
203. Steculorum, S. M. *et al.* AgRP Neurons Control Systemic Insulin Sensitivity via Myostatin Expression in Brown Adipose Tissue. *Cell* **165,** 125–138 (2016).
204. Schmidt, E. *et al.* LincRNA H19 protects from dietary obesity by constraining expression of monoallelic genes in brown fat. *Nat. Commun.* (accepted, 2018).
205. Wagle, P., Nikolić, M. & Frommolt, P. QuickNGS elevates Next-Generation Sequencing data analysis to a new level of automation. *BMC Genomics* **16,** 487 (2015).

206. Gao, J. *et al.* CLUH regulates mitochondrial biogenesis by binding mRNAs of nuclear-encoded mitochondrial proteins. *J. Cell Biol.* **207,** 213–23 (2014).
207. Sommer, C., Straehle, C., Kothe, U. & Hamprecht, F. A. Ilastik: Interactive learning and segmentation toolkit. in *2011 IEEE International Symposium on Biomedical Imaging: From Nano to Macro* 230–233 (IEEE, 2011).
208. Kamentsky, L. *et al.* Improved structure, function and compatibility for CellProfiler: modular high-throughput image analysis software. *Bioinformatics* **27,** 1179–1180 (2011).
209. Thorvaldsen, J. L., Fedoriw, A. M., Nguyen, S. & Bartolomei, M. S. Developmental profile of H19 differentially methylated domain (DMD) deletion alleles reveals multiple roles of the DMD in regulating allelic expression and DNA methylation at the imprinted H19/Igf2 locus. *Mol. Cell. Biol.* **26,** 1245–58 (2006).
210. Ainscough, Justin F-X. Koide, Tsuyoshi Tada, M. B. S. S. M. A. Imprinting of Igf2 and H19 from a 130kb YAC transgene. *Dev.* **124,** 3621–3632 (1997).
211. Armengol, J. *et al.* Pref-1 in brown adipose tissue: specific involvement in brown adipocyte differentiation and regulatory role of C/EBPδ. *Biochem. J.* **443,** 799–810 (2012).
212. Brand, M. D. & Nicholls, D. G. Assessing mitochondrial dysfunction in cells. *Biochem. J* **435,** 297–312 (2011).
213. Derrien, T. *et al.* The GENCODE v7 catalog of human long noncoding RNAs: analysis of their gene structure, evolution, and expression. *Genome Res.* **22,** 1775–89 (2012).
214. van Heesch, S. *et al.* Extensive localization of long noncoding RNAs to the cytosol and mono- and polyribosomal complexes. *Genome Biol.* **15,** R6 (2014).
215. Gonzalez, I. *et al.* A lncRNA regulates alternative splicing via establishment of a splicing-specific chromatin signature. *Nat. Struct. Mol. Biol.* **22,** 370–376 (2015).
216. Eun, B. *et al.* The Igf2/H19 muscle enhancer is an active transcriptional complex. *Nucleic Acids Res.* **41,** 8126–8134 (2013).
217. Guerra, C. *et al.* Brown adipose tissue-specific insulin receptor knockout shows diabetic phenotype without insulin resistance. *J. Clin. Invest.* **108,** 1205–13 (2001).
218. Oliverio, M. *et al.* Dicer1–miR-328–Bace1 signalling controls brown adipose tissue differentiation and function. *Nat. Cell Biol.* (2016).
219. Schlein, C. & Heeren, J. Implications of thermogenic adipose tissues for metabolic health. (2016).

220. Zhang, N. *et al.* Elevated hepatic expression of H19 long noncoding RNA contributes to diabetic hyperglycemia. *JCI Insight* **3,** (2018).
221. Vernochet, C. *et al.* Adipose tissue mitochondrial dysfunction triggers a lipodystrophic syndrome with insulin resistance, hepatosteatosis, and cardiovascular complications. *FASEB J.* **28,** 4408–19 (2014).
222. Boutant, M. *et al.* Mfn2 is critical for brown adipose tissue thermogenic function. *EMBO J.* **36,** 1543–1558 (2017).
223. Barlow, D. P., Stöger, R., Herrmann, B. G., Saito, K. & Schweifer, N. The mouse insulin-like growth factor type-2 receptor is imprinted and closely linked to the Tme locus. *Nature* **349,** 84–87 (1991).
224. Gabory, A. *et al.* H19 acts as a trans regulator of the imprinted gene network controlling growth in mice. *Development* **136,** 3413–21 (2009).
225. Simon, M. D. *et al.* The genomic binding sites of a noncoding RNA. *Proc. Natl. Acad. Sci. U. S. A.* **108,** 20497–502 (2011).
226. Balsa-Canto, E., Henriques, D., Gábor, A. & Banga, J. R. AMIGO2, a toolbox for dynamic modeling, optimization and control in systems biology. *Bioinformatics* **32,** 3357–3359 (2016).
227. Smits, G. *et al.* Conservation of the H19 noncoding RNA and H19-IGF2 imprinting mechanism in therians. *Nat. Genet.* **40,** 971–976 (2008).
228. Ding, C. *et al.* De novo reconstruction of human adipose transcriptome reveals conserved lncRNAs as regulators of brown adipogenesis. *Nat. Commun.* **9,** 1329 (2018).
229. Atkinson, S. R. & Marguerat, S. Exploring long non-coding RNAs through sequencing. *Semin. Cell Dev. Biol.* **23,** 200–205 (2012).
230. Guo, Y. *et al.* RNAseq by Total RNA Library Identifies Additional RNAs Compared to Poly(A) RNA Library. *Biomed Res. Int.* **2015,** 1–9 (2015).
231. Watts, J. K. & Corey, D. R. Silencing disease genes in the laboratory and the clinic. *J. Pathol.* **226,** 365–79 (2012).
232. Geary, R. S., Baker, B. F. & Crooke, S. T. Clinical and preclinical pharmacokinetics and pharmacodynamics of mipomersen (kynamro(®)): a second-generation antisense oligonucleotide inhibitor of apolipoprotein B. *Clin. Pharmacokinet.* **54,** 133–46 (2015).
233. Kamola, P. J. *et al. In silico* and *in vitro* evaluation of exonic and intronic off-target effects form a critical element of therapeutic ASO gapmer optimization. *Nucleic*

Acids Res. **43,** 8638–8650 (2015).

234. Shoshani, O. *et al.* Polyploidization of murine mesenchymal cells is associated with suppression of the long noncoding RNA H19 and reduced tumorigenicity. *Cancer Res.* **72,** 6403–13 (2012).
235. Martinet, C. *et al.* H19 controls reactivation of the imprinted gene network during muscle regeneration. *Development* **143,** 962–71 (2016).
236. Bruderer, M., Richards, R., Alini, M. & Stoddart, M. Role and regulation of RUNX2 in osteogenesis. *Eur. Cells Mater.* **28,** 269–286 (2014).
237. Chen, Q. *et al.* Fate decision of mesenchymal stem cells: adipocytes or osteoblasts? *Cell Death Differ.* **23,** 1128–39 (2016).
238. Liu, L.-F., Shen, W.-J., Zhang, Z. H., Wang, L. J. & Kraemer, F. B. Adipocytes decrease Runx2 expression in osteoblastic cells: Roles of PPARγ and adiponectin. *J. Cell. Physiol.* **225,** 837–845 (2010).
239. Ge, C. *et al.* Reciprocal Control of Osteogenic and Adipogenic Differentiation by ERK/MAP Kinase Phosphorylation of Runx2 and PPARγ Transcription Factors. *J. Cell. Physiol.* **231,** 587–596 (2016).
240. Sun, C., Berry, W. L. & Olson, L. E. PDGFRα controls the balance of stromal and adipogenic cells during adipose tissue organogenesis. *Development* **144,** 83–94 (2017).
241. Venkatraman, A. *et al.* Maternal imprinting at the H19–Igf2 locus maintains adult haematopoietic stem cell quiescence. *Nature* **500,** 345–349 (2013).
242. Dey, B. K., Pfeifer, K. & Dutta, A. The H19 long noncoding RNA gives rise to microRNAs miR-675-3p and miR-675-5p to promote skeletal muscle differentiation and regeneration. *Genes Dev.* **28,** 491–501 (2014).
243. Giovarelli, M. *et al.* H19 long noncoding RNA controls the mRNA decay promoting function of KSRP. *Proc. Natl. Acad. Sci. U. S. A.* **111,** E5023-8 (2014).
244. Boucher, J. *et al.* Insulin and insulin-like growth factor 1 receptors are required for normal expression of imprinted genes. *Proc. Natl. Acad. Sci. U. S. A.* **111,** 14512–7 (2014).
245. Golozoubova, V. *et al.* Depressed Thermogenesis but Competent Brown Adipose Tissue Recruitment in Mice Devoid of All Hormone-Binding Thyroid Hormone Receptors. *Mol. Endocrinol.* **18,** 384–401 (2004).
246. Cannon, B. & Nedergaard, J. Nonshivering thermogenesis and its adequate measurement in metabolic studies. *J. Exp. Biol.* **214,** 242–53 (2011).

247. Griggio, M. A. Thermogenic mechanisms in cold-acclimated animals. *Brazilian J. Med. Biol. Res. = Rev. Bras. Pesqui. medicas e Biol.* **21,** 171–6 (1988).
248. Jeffery, E. *et al.* Characterization of Cre recombinase models for the study of adipose tissue. *Adipocyte* **3,** 206–11 (2014).
249. Krueger, K. C., Costa, M. J., Du, H. & Feldman, B. J. Characterization of Cre Recombinase Activity for In Vivo Targeting of Adipocyte Precursor Cells. *Stem Cell Reports* **3,** 1147–1158 (2014).
250. Scorrano, L. Multiple functions of mitochondria-shaping proteins. *Novartis Found. Symp.* **287,** 47-55; discussion 55–9 (2007).
251. Cogliati, S., Enriquez, J. A. & Scorrano, L. Mitochondrial Cristae: Where Beauty Meets Functionality. *Trends Biochem. Sci.* **41,** 261–273 (2016).
252. Koc, E. C. *et al.* The Large Subunit of the Mammalian Mitochondrial Ribosome. *J. Biol. Chem.* **276**, 43958-69 (2001).
253. Wang, Z., Cotney, J. & Shadel, G. S. Human mitochondrial ribosomal protein MRPL12 interacts directly with mitochondrial RNA polymerase to modulate mitochondrial gene expression. *J. Biol. Chem.* **282,** 12610–8 (2007).
254. Graziewicz, M. A., Longley, M. J. & Copeland, W. C. DNA Polymerase γ in Mitochondrial DNA Replication and Repair. *Chem Rev.* **106**, 383-405 (2006).
255. Horsefield, R. *et al.* Structural and Computational Analysis of the Quinone-binding Site of Complex II (Succinate-Ubiquinone Oxidoreductase). *J. Biol. Chem.* **281**, 7309-15. (2005).
256. Virbasius, J. V & Scarpulla, R. C. Activation of the human mitochondrial transcription factor A gene by nuclear respiratory factors: a potential regulatory link between nuclear and mitochondrial gene expression in organelle biogenesis. *Proc. Natl. Acad. Sci. U. S. A.* **91,** 1309–13 (1994).
257. Zurita Rendón, O., Silva Neiva, L., Sasarman, F. & Shoubridge, E. A. The arginine methyltransferase NDUFAF7 is essential for complex I assembly and early vertebrate embryogenesis. *Hum. Mol. Genet.* **23,** 5159–5170 (2014).
258. Schägger, H., Brandt, U., Gencic, S. & von Jagow, G. Ubiquinol-cytochrome-c reductase from human and bovine mitochondria. *Methods Enzymol.* **260,** 82–96 (1995).
259. Monnier, P. *et al.* H19 lncRNA controls gene expression of the Imprinted Gene Network by recruiting MBD1. *Proc. Natl. Acad. Sci. USA.* **1,** 20693-8 (2013).
260. Imig, J. *et al.* miR-CLIP capture of a miRNA targetome uncovers a lincRNA H19-

miR-106a interaction. *Nat. Chem. Biol.* **11,** 1–10 (2014).

261. Zhou, J. *et al.* H19 lncRNA alters DNA methylation genome wide by regulating S-adenosylhomocysteine hydrolase. *Nat. Commun.* **6,** 10221 (2015).
262. Jobe, E. M. *et al.* Methyl-CpG-Binding Protein MBD1 Regulates Neuronal Lineage Commitment through Maintaining Adult Neural Stem Cell Identity. *J. Neurosci.* **37,** 523–536 (2017).
263. Takahashi, M., Kamei, Y. & Ezaki, O. Mest/Peg1 imprinted gene enlarges adipocytes and is a marker of adipocyte size. *Am. J. Physiol. Metab.* **288,** E117–E124 (2005).
264. Fujiwara, K. *et al.* Necdin Controls Proliferation of White Adipocyte Progenitor Cells. *PLoS One* **7,** e30948 (2012).
265. Kotzbeck, P. *et al.* Brown adipose tissue whitening leads to brown adipocyte death and adipose tissue inflammation. *J. Lipid Res.* **59,** 784–794 (2018).
266. Haig, D. Genomic Imprinting and Kinship: How Good is the Evidence? *Annu. Rev. Genet.* **38,** 553–585 (2004).
267. Ishida, M. & Moore, G. E. The role of imprinted genes in humans. *Mol. Aspects Med.* **34,** 826–840 (2013).
268. Pappas, J. G. The clinical course of an overgrowth syndrome, from diagnosis in infancy through adulthood: the case of Beckwith-Wiedemann syndrome. *Curr. Probl. Pediatr. Adolesc. Health Care* **45,** 112–7 (2015).
269. DeBaun, M. R. *et al.* Epigenetic Alterations of H19 and LIT1 Distinguish Patients with Beckwith-Wiedemann Syndrome with Cancer and Birth Defects. *Am. J. Hum. Genet.* **70,** 604–611 (2002).
270. Van De Pette, M. *et al.* Cdkn1c Boosts the Development of Brown Adipose Tissue in a Murine Model of Silver Russell Syndrome. *PLoS Genet.* **12,** e1005916 (2016).
271. Eggermann, T. *et al.* CDKN1C mutations: two sides of the same coin. *Trends Mol. Med.* **20,** 614–22 (2014).
272. Chu, C., Spitale, R. C. & Chang, H. Y. Technologies to probe functions and mechanisms of long noncoding RNAs. *Nat. Struct. Mol. Biol.* **22,** 29–35 (2015).
273. Porter, C. *et al.* Human and Mouse Brown Adipose Tissue Mitochondria Have Comparable UCP1 Function. *Cell Metab.* **24,** 246–255 (2016).
274. Kiwaki, K. & Levine, J. A. Differential effects of adrenocorticotropic hormone on human and mouse adipose tissue. *J. Comp. Physiol. B Biochem. Syst. Environ. Physiol.* **173,** 675–678 (2003).

275. Markussen, L. K. *et al.* Characterization of immortalized human brown and white pre-adipocyte cell models from a single donor. *PLoS One* **12,** e0185624 (2017).
276. Hanahan, D. & Weinberg, R. A. Hallmarks of cancer: the next generation. *Cell* **144,** 646–674 (2011).
277. Sandulache, V. C. & Myers, J. N. Altered metabolism in head and neck squamous cell carcinoma: an opportunity for identification of novel biomarkers and drug targets. *Head Neck* **34,** 282–90 (2012).
278. Kamarajan, P. *et al.* Head and Neck Squamous Cell Carcinoma Metabolism Draws on Glutaminolysis, and Stemness Is Specifically Regulated by Glutaminolysis via Aldehyde Dehydrogenase. *J. Proteome Res.* **16,** 1315–1326 (2017).
279. Curry, J. M. *et al.* Tumor Microenvironment in Head and Neck Squamous Cell Carcinoma. *Semin. Oncol.* **41,** 217–234 (2014).
280. Ferreira, P. G. *et al.* The effects of death and post-mortem cold ischemia on human tissue transcriptomes. *Nat. Commun.* **9,** 490 (2018).
281. Ward, M., McEwan, C., Mills, J. D. & Janitz, M. Conservation and tissue-specific transcription patterns of long noncoding RNAs. *J. Hum. Transcr.* **1,** 2–9 (2015).
282. Madiraju, A. K. *et al.* Metformin suppresses gluconeogenesis by inhibiting mitochondrial glycerophosphate dehydrogenase. *Nature* **510,** 542–546 (2014).
283. Breining, P. *et al.* Metformin targets brown adipose tissue in vivo and reduces oxygen consumption in vitro. *Diabetes, Obes. Metab.* (2018).
284. Zhong, T. *et al.* Metformin alters DNA methylation genome-wide via the H19/SAHH axis. *Oncogene* **36,** 2345–2354 (2017).
285. Lindsay, R. S. & Loeken, M. R. Metformin use in pregnancy: promises and uncertainties. *Diabetologia* **60,** 1612–1619 (2017).
286. Deng, J. *et al.* H19 lncRNA alters methylation and expression of Hnf4α in the liver of metformin-exposed fetuses. *Cell Death Dis.* **8,** e3175 (2017).

Acknowledgements

Prof. Dr. Jan-Wilhelm Kornfeld Thank you for giving me the opportunity to do my PhD research in your lab and for trusting me with this fascinating project. I am very thankful for your support, your scientific guidance, and the sustained interest in the progress of the project during all these years. Thank you for giving me the freedom to develop myself, to let me become aware of my strengths and to improve on my weaknesses.

PhD thesis committee I would like to thank Prof. Thorsten Hoppe, Prof. Matthias Hammerschmidt and Dr. Ursula Lichtenberg for their time reading my PhD thesis and their acceptance of the invitation to become part of my PhD thesis committee.

Evangelisches Studienwerk Villigst e.V. I gratefully acknowledge the funding that I received for my PhD research. I´ve had some great times in Haus Villigst and enjoyed being part of such a great organization.

To all the collaborators Thank you all for contributing to this research project. A special thank goes to Martin Bilban for his support, fruitful scientific discussions, and contribution to the paper. Thank you, Evgenia Ntini and Ulf Ørom for welcoming me in your lab and teaching me the ChART technique.

Kornfeld, Brüning, Wunderlich, Steculorum lab members I want to show my appreciation towards all members of BWKS labs for their support, the encouragements, and fun times. Hardly have I laughed so much (although I didn´t always know the reason for it and I´m sure that it was often enough out of desperation about the topics ;-)). My special thanks go to Anke, Cathy, Sandra, Sajjad, Jule, Paul, Philipp, Marta P.-J., Sinika, Jonas, Nils, Jens A. I´ll miss you guys the moment I leave the institute.

Rachel Special thanks go to you for proofreading my thesis.

Matteo and Isa My favourite Italian couple. Thank you both for everything (including the uncountable coffee capsules and Scamorze). I´m so happy that I could experience my PhD-time with both of you. You two make up the perfect balance between driven and relax ;-)

Ines Ich freue mich, dass du dich entschieden hast für deine Masterarbeit in unser Labor zu kommen. Es hat super viel Spaß gemacht mit dir zusammenzuarbeiten, zu lachen und Frozen Margaritas trinken zu gehen.

Nasim First of all, thank you for proofreading parts of the thesis. I´m so happy that we´ve spent so much time together lately. Thank you for being there and for your support, especially in the last and most energy-consuming steps of the PhD.

Katharina Möller Ich bin sehr dankbar, dass wir uns über Villigst kennengelernt haben und so viel schöne gemeinsame Dinge zusammen erlebt haben. Danke für die gemeinsamen Lunch-Pausen, Abendessen oder Treffen zwischendurch.

Mama and Robert Vom Abi, zum BSc, zum MSc und nun zum PhD und niemals habt ihr aufgehört an mich zu glauben. Danke für eure bedingungs- und endlose Unterstützung. Seit ich denken kann, Mama, ermöglichst du mir alles was ich erreichen möchte und bist immer für mich da. Du bist nicht nur „Mama“, sondern auch meine beste Freundin. DANKE an euch beide!

Henri Auch wenn du das noch nicht lesen kannst, möchte ich dir danken, dass du mir bei leider viel zu seltenen Heimatbesuchen immer die Wichtigkeit von Freizeit vermittelt hast, wenn du mit deinen großen bestechlichen Augen danach verlangt hast mit dir zu spielen, während ich über meine Arbeit gegrübelt habe.

Family and Friends Papa, Kathy, Micha, Kim, Daniel, Katha, Hanna, Franzi... Danke für die entspannten und schönen Momente zwischendurch und euer Verständnis, dass ich nicht bei jedem Event der letzten Jahre dabei sein konnte.

My Dutch Family Dank jullie voor jullie ondersteuning en interesse in mijn promotieonderzoek. Ik heb er altijd met veel plezier over uitgelegd en gepraat.

Henk Finally, I would like to say - and I think that three words can´t express what it means to me how much you have supported me the last years - “Dank je wel” to the most caring person in the world I know. Getting to know you at our first Promotreffen in Villigst and starting a life together with you was for sure one of the best things that happened to me. Thank you for your patience and your endless support, not only with motivational and sometimes critical words but also deeds. Living together in one room with both of us writing our PhD theses and still getting along so well… I´m convinced we can manage everything in life together ♥

Erklärung

Ich versichere, dass ich die von mir vorgelegte Dissertation selbstständig angefertigt, die benutzten Quellen und Hilfsmittel vollständig angegeben und die Stellen der Arbeit – einschließlich Tabellen, Karten und Abbildungen –, die anderen Werken im Wortlaut oder dem Sinn nach entnommen sind, in jedem Einzelfall als Entlehnung kenntlich gemacht habe; dass diese Dissertation noch keiner anderen Fakultät oder Universität zur Prüfung vorgelegen hat; dass sie – abgesehen von unten angegeben Teilpublikationen – noch nicht veröffentlicht worden ist sowie, dass ich eine solche Veröffentlichung vor Abschluss des Promotionsverfahrens nicht vornehmen werde. Die Bestimmungen dieser Promotionsordnung sind mir bekannt. Die von mir vorgelegte Dissertation ist von Prof. Dr. Jan-Wilhelm Kornfeld betreut worden.

Köln, 8. November 2018

Elena Schmidt

Teilpublikation

Schmidt E, Dhaouadi I, Gaziano I, Oliverio M, Klemm P, Awazawa M, Mitterer G, Fernandez-Rebollo E, Pradas-Juni M, Wagner W, Hammerschmidt P, Loureiro R, Kiefer C, Hansmeier NR, Khani S, Bergami M, Heine M, Ntini E, Frommolt P, Zentis P, Ørom UA, Heeren J, Blüher M, Bilban M, Kornfeld JW.
LincRNA *H19* protects from dietary obesity by constraining expression of monoallelic genes in brown fat. *Nat Commun*. (accepted)